

General Disclaimer

One or more of the Following Statements may affect this Document

- This document has been reproduced from the best copy furnished by the organizational source. It is being released in the interest of making available as much information as possible.
- This document may contain data, which exceeds the sheet parameters. It was furnished in this condition by the organizational source and is the best copy available.
- This document may contain tone-on-tone or color graphs, charts and/or pictures, which have been reproduced in black and white.
- This document is paginated as submitted by the original source.
- Portions of this document are not fully legible due to the historical nature of some of the material. However, it is the best reproduction available from the original submission.

Interim Report
for
COLLOID THRUSTER TECHNOLOGY
(20 June 1969 - 20 June 1970)

Contract No. NAS5-21025

Prepared by

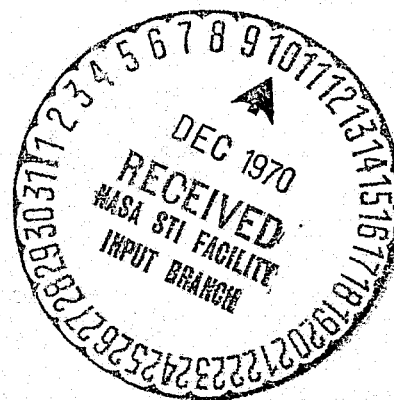
Electro-Optical Systems
300 North Halstead Street
Pasadena, California 91107

for

Goddard Space Flight Center
Greenbelt, Maryland

FACILITY FORM 602

N71-12076	(THRU)
134	43
(PAGES)	(COPIES)
CR-111417	28
(NASA CR OR TMX OR AD NUMBER)	(CATEGORY)



Interim Report

for

COLLOID THRUSTER TECHNOLOGY
(20 June 1969 - 20 June 1970)

Contract No. NAS5-21025

Goddard Space Flight Center

Contracting Officer: A. L. Essex
Technical Monitor: A. Sherman

Prepared by

Electro-Optical Systems
300 North Halstead Street
Pasadena, California 91107

Project Manager: Dr. Julius Perel

for

Goddard Space Flight Center
Greenbelt, Maryland

ABSTRACT

A study program was initiated to show the feasibility of the annular geometry design (as opposed to capillary needle geometry) for the future development of a colloid thruster system composed of a simplified array of emitters. In addition to demonstrating this feasibility, the annulus has shown reproducible operation over a wide range of performance levels at high efficiencies with no glow discharge and very low extractor currents. This was attained by means of a coupled experimental/analytical investigation and carefully designed experiments on temperature, mass flow, beam configuration and glow discharge effects. The analytical study resulted in a set of equations that describe the interrelation of the operational parameters, thrust, specific impulse, specific charge and current and their variations with control variables, voltage and mass flowrate. A region of operation where the current and thrust were linear with mass flowrate was uncovered. Operation of a thruster system in this region with the developed mass flow meter and controller permits a simple feedback control system and determinations of thrust and specific impulse without the time-of-flight analysis previously required. Instrumentation developed and the test results investigated are reported. Advanced thruster design is discussed for operation at 1 mlb with 19 emitters.

FOREWORD

The work described in this interim report is the result of the first year of a program at Electro-Optical Systems (EOS) under Contract No. NAS5-21025 with NASA, Goddard Space Flight Center (GSFC). The technical monitor is Dr. Allan Sherman who made important contributions in the program direction and in specific technical areas with assistance from William Burton, also from GSFC. At EOS, Dr. Julius Perel (Project Manager), and Messrs. John F. Mahoney and Arthur Y. Yahiku performed the technical work and prepared this interim report with assistance and consultation from Mr. Howard L. Daley. Important new equipment was supplied by EOS and work on a mass flow system was aided by Gerald E. Trump and Gale Gant. Preparation of laboratory apparatus and fabrication of annular emitters were accomplished by Arthur Kasa and J. Robert Otto.

CONTENTS

<u>Section</u>	<u>Title</u>	<u>Page</u>
1.	INTRODUCTION	1
2.	PROGRAM APPROACH AND TECHNIQUES	4
2.1	Technical Approach	4
2.1.1	Background Considerations	4
2.1.2	Thruster Equations	5
2.2	Experimental Techniques	7
2.2.1	Experimental Arrangement	7
2.2.2	Apparatus and Instrumentation	9
2.2.3	Data Reduction	24
2.3	Thruster Design	28
2.3.1	Emitter Configurations	28
2.3.2	Emitter Material and Fabrication	32
2.3.3	Thruster Configuration	39
3.	PROPELLANT AND FLOW CONTROL TESTS	45
3.1	Propellant Properties	45
3.2	Flowrate Control Test With an Annulus	47
4.	ANALYTICAL STUDIES	51
4.1	Background Data	52
4.2	Thruster Equations	53
4.3	Comparison With Experiment	62
4.4	Performance Indices	66
4.5	Theoretical Thruster Design	69
5.	ANNULAR THRUSTER TESTS	72
5.1	Test Runs	72
5.2	Thruster Performance	72
5.2.1	Parametrics	77
5.2.2	Beam Focusing Effects	86
5.2.3	Mass Flow Parametrics	91
5.2.4	Temperature Effects	98
5.2.5	Summary of Thruster Performance	104

CONTENTS (contd)

<u>Section</u>	<u>Title</u>	<u>Page</u>
5.3	Glow Discharge Effects	107
5.3.1	Radiation Characteristics of Glow Discharge	108
5.3.2	Glow Discharge and Inner Extractor Currents	108
5.3.3	Trapping Electrode Tests	113
5.4	Advanced State-of-the-Art Thruster	116
6.	SUMMARY	121
6.1	Achievements	121
6.2	Problems	123
	GLOSSARY	124
	REFERENCES	126

ILLUSTRATIONS

<u>Figure</u>	<u>Title</u>	<u>Page</u>
1	Specific Impulse versus Thrust	8
2	Schematic Diagram of Experimental Setup	10
3	2 foot by 3 foot Vacuum Chamber Showing Colloid Instrumentation	11
4	Segmented Cylindrical Collector	13
5	Segmented TOF Collector	14
6	Block Diagram of Digitize Mode	15
7	Block Diagram of Thyatron Switch and Data Acquisition Synchronization	17
8	Block Diagram of Punch Mode	18
9	Block Diagram of Display Mode	19
10	Thyatron Switch Circuitry	21
11	Propellant Flow Meter and Control Device	23
12	Photomicrographic Equipment	25
13	Examples of TOF Traces	26
14	Inner Annulus Sleeving Showing Details of Flow Grooves	30
15	Inner and Outer Annulus Sleeving (Annulus A08)	31
16	Photomicrograph of Annulus A06 (X50 Magnification) After Testing (Run 7001-01, -02)	33
17	GSFC Annular Emitter	34
18	Photomicrograph Showing Details of Thoriated (2%) Tungsten Annulus (A07) Emitter Edge at 50X Magnification	36
19	Technique of Fabricating Emitter with Pt/Ir Edge	37
20	Photomicrograph Showing Details of Platinum (90%)/Iridium (10%) and 20Cb3 S.S. Annulus (A08) Emitter Edges at X50 Magnification	38
21	Photomicrograph (X50 Magnification) of Pt/Ir and 20CB3 Stainless Steel Emitter (A08) After 50 Hours of Continuous Operation (Run 7003-01)	40
22	Annulus Colloid Thruster	41
23	Inner and Outer Extractor Geometries	43
24	Viscosity of Glycerol	46

ILLUSTRATIONS (contd)

<u>Figure</u>	<u>Title</u>	<u>Page</u>
25	Conductivity versus Temperature for 20 gm NaI/100 ml Glycerol Mixture	48
26	Annulus Emitter Current versus Mass Flowmeter Reading	50
27	I versus \dot{m} for Annulus A01 (Run 6909-02)	54
28	Variation of Thrust, Current, and Specific Impulse for Annulus A01 (Run 6909-01 at 15 kV)	55
29	Thrust versus Current (Run 6909-02)	56
30	Parametric Variation with \dot{m} at V = Constant	61
31	I versus \dot{m} for A02, Run 6910-01	63
32	T versus \dot{m} for A02, Run 6910-01	64
33	I_{sp} versus \dot{m} for A02, Run 6910-01	65
34	Current, Specific Impulse, and Thrust versus \dot{m} for A06, Run 7005-02	67
35	Current versus Mass Flowrate for Various Parameters	68
36	Operational Parameters for a Theoretical Thruster Operated at 15 kV ($k_o = 0.95$, $P = 47.5 \times 10^{-13}$)	71
37	Mass Flowrate versus Thrust at a Constant Temperature for Annulus A06, Run 7004-04	78
38	Mass Flowrate versus Thrust at Various Temperatures for Annulus A06, Run 7005-02	79
39	Operational Parameters versus Mass Flowrate for Annulus A09, Run 7006-01	81
40	Effect of Smaller Rim on Thruster Performance for Run 7004-04 (A06) and 7006-01 (A09)	83
41	Variation of Specific Impulse with Thrust for Annulus Parametric Study (Annulus A01)	84
42	I versus \dot{m} for GSFC Thruster, Propellant F02, Run 6910-03	87
43	Specific Impulse versus Mass Flow (Run No. 6910-03-GSFC)	88
44	Thrust versus Mass Flow (Run No. 6190-03-GSFC)	89
45	Collection Efficiency versus \dot{m} , Run 6910-03	90
46	Efficiency Collection versus Mass Flow Emitter A02 - Run 6912-01	92
47	Collection Efficiency versus Mass Flowrate as a Function of Temperature at 15 kV for Annulus A06 (Run 7006-02)	93
48	Effects of Feed Pressure on Mass Flowrate for Annulus A06, Run 7002-02	95

ILLUSTRATIONS (contd)

<u>Figure</u>	<u>Title</u>	<u>Page</u>
49	Effects of Temperature on Mass Flowrate for Annulus A06, Run 7006-02	96
50	Mass Flowrate as a Function of Voltage for Annulus A06, Run 7002-02	97
51	Mass Flowrate as a Function of Specific Charge for Various Temperatures for Annulus A06, Run 7006-02	100
52	Variation of Specific Charge with Temperature for Constant Mass Flowrates for Annulus A06, Run 7006-02	101
53	Source Current as a Function of Mass Flowrate for Annulus A06, Run 7006-02	102
54	Specific Impulse as a Function of Mass Flowrate for Annulus A06, Run 7006-02	103
55	Wide Band Spectra of Annulus Glow (Annulus A03, Run 7002-03)	109
56	Variation of Inner and Outer Extractor Currents with Outer Extractor Voltage at Inner Extractor Voltages of -0.5, -2.5, and -4.5 kV. (Annulus A06, Run 7004-03)	111
57	Cross Sectional View of Annulus (A06) Assembly Showing Electron Shield Electrode	114
58	Operational Parameters versus \dot{m} for an Advanced Thruster Design for $k_0 = 0.815$, $P = 87.2 \times 10^{-13}$, $\eta_i = 80\%$ Operated at 15 kV	120

SECTION 1

INTRODUCTION

Colloid thrusters show the potential of operating very efficiently at thrust levels of a mlb or less and at specific impulse levels between 500 and 1500 seconds. The high efficiency occurs because the charged particle generating and accelerating processes are actuated by the same electric field with very little power required for particle generation. Hence, for near earth applications within this specific impulse range, colloid propulsion would indeed be competitive.

Initial investigations were made using capillary needle geometries to obtain the high electric fields required to produce charged particle beams. Thruster levels of a few μ lb can be produced by single needle emitters at the high end of the specific impulse range of interest. This emitter geometry has several limitations such as the low thrust per emitter and the poor temperature control. When total thrust at the mlb level is required for a thruster system, the low thrust per emitter limitation presents fabrication and reliability problems particularly for operation at high specific impulse. Temperature problems arise because of a low thermal conductivity for the needle geometry. These problems affect mass flow control because of the high thermal variation of the propellant (glycerol) viscosity. The charge particle generation process is also dependent upon the temperature at the emitter tip.

To minimize these problems, linear slit geometry emitters were investigated with some success (Refs. 1, 2 and 3). Annular geometry emitters, which avoid the fabrication and operational problem associated with linear slits, were developed and successfully tested at NASA Goddard (Ref. 4). This was followed by the EOS development of a large

annulus with a different structural design (Ref. 5). A design similar to the Goddard design was developed at TRW and referred to as an "annular needle" (Ref. 3). All of the initial tests showed the design to be feasible and more than competitive with the capillary needle geometry. The investigations described in this report show that annulus performance, range of operation, simplicity of fabrication, and other features exceed those of capillary needles except that higher voltage is required. In addition, the wider range of operation and stability resulted in performance features of the annulus which aided the development of a fruitful analytical investigation.

The primary goal of this program was to demonstrate the applicability of annulus geometry as a colloid thruster system. Emphasis was placed upon ease of fabrication and operation in comparison with a capillary needle array for the same performance conditions. In addition, glow discharge phenomenon and high extractor current investigations were considered important because of their effects upon operation and because they introduce an uncertainty in performance data. Emitter edge erosion was monitored by periodic microphotography for correlation with degradation of performance (if any).

Several highlights were achieved on the program to date which advanced the state of the art in both experimental techniques and emitter performance. The techniques developed include a new data reduction system for time-of-flight analysis and a mass flow control and metering system. Emitters were operated over a range of voltages and mass flowrates which resulted in a wide range of thruster operating levels. Specific impulses of > 1000 seconds were achieved, glow discharges were eliminated as a result of electrode and temperature studies, and temperature effects were investigated which indicate a direction of investigation which may increase specific impulse. A single annulus was operated at 13 kV producing a thrust of 174 μ lb at 550 seconds which showed stable reproducible operation. Under less stable conditions a single annulus

was operated at 15 kV and produced 200 μ lb at 900 seconds. Finally, from a series of coordinated experimental and analytical investigations, a set of analytical functions were derived which interrelates various thruster performance parameters and can be used to predict variations of parameters and provide a consistent basis for extrapolation of results. These studies have led to a greater understanding of the operation of both annular and needle geometry emitters so that tradeoffs between various operating modes can be predicted.

The work on the remainder of this program will be aimed toward increasing the specific impulse while maintaining high thrust per emitter levels. An annular array will be developed and tested for controllability, reliability and durability.

This interim report describes the techniques used, the results obtained and the understanding gained during the first year of the program. The following section discusses the technical approach along with the experimental techniques and hardware that was used. Section 3 discusses the propellant investigations and flow control tests. The analytical studies supported by experimental data, are discussed in Section 4. The emitter runs are tabulated and the results, organized parametrically using the analytical equations, are described in Section 5. Only those data providing insight, understanding, and particular features of interest are shown of the vast amount of data that led up to this level. Section 5 also presents a state-of-the-art thruster design and is followed by a report summary given in Section 6.

SECTION 2

PROGRAM APPROACH AND TECHNIQUES

2.1 TECHNICAL APPROACH

The approach and techniques used in the development of colloid annular thrusters do not differ appreciably from those previously employed in capillary needle investigations. Nevertheless, some aspects of the present program are significantly different and include the successful use of analytical techniques to complement the experimental effort and thereby enhance the overall results. This enhancement was accomplished using advanced data taking and data display techniques to uncover the emitter parametric variations with performance level. Experimental and data taking techniques are described in this section with the analytical studies described in Section 4.

2.1.1 BACKGROUND CONSIDERATIONS

Interest in the colloid thruster has occurred because of its relatively simple operation and high efficiency in the specific impulse range of 500 to 1500 seconds. Generation and acceleration of the charged particles is accomplished by applying an intense electric field (typically $> 10^6$ V/cm) to the surface of a conducting propellant fluid. The intense field is obtained using high curvature geometry with nominally high voltages (5 to 15 kV). The acceleration of these particles provides the thrust for colloid thrusters.

Laboratory operation consists of providing a controlled mass flowrate (\dot{m}) to an emitter tip that is maintained at high voltage (V) to produce a current (I) of charged particles. The most essential measurements include the voltage, the beam current, and time-of-flight (TOF) data

to examine the distribution of the beam particles. From an analysis of TOF data, the mean charge-to-mass ratio (or mean specific charge, $\langle q/m \rangle$) can be obtained along with the beam efficiency (η). The term η is a measure of the efficiency of the beam to produce thrust as compared with that produced by a beam composed of a single specific charge at the same mass flowrate and voltage (Refs. 5 and 6). The most widely used propellant, glycerol doped with NaI to make it sufficiently conductive, is contained in a pressurized reservoir with the feedrate generally controlled by varying the pressure. Until recently, emitters were generally made of capillary needles with I.D. of 0.002 inch to 0.008 inch. The complexity of fabricating a large array of needles when thrusts $> 100 \mu\text{lb}$ are desired led to the development of linear slits and then to annular slits. The experimental investigations on this program concentrated on annular slit emitters.

2.1.2 THRUSTER EQUATIONS

The two vital parameters required to determine the performance level of a thruster system on a mission are the thrust (T) and specific impulse (I_{sp}). These plus the beam current, mean specific charge, and power efficiency constitute thruster "operational parameters". The performance level can be changed by means of the "control variables" which are the accelerating voltage and mass flowrate. The control variables also include emitter temperature, emitter geometry, and propellant properties which are controllable, but cannot readily be varied during emitter test. These parameters are summarized as follows:

- | | | |
|----|------------------------|---|
| a. | Control Variables | V , \dot{m} , Emitter, Temperature, Geometry, Propellant Properties |
| b. | Operational Parameters | I , $\langle q/m \rangle$, I_{sp} , T , η |

Thrust is given by

$$T = \dot{m} \langle v \rangle \quad (1)$$

where $\langle v \rangle$ is the mean particle velocity in the beam assuming the beam to be parallel (nondivergent). If the mass utilization efficiency is 100 percent the specific impulse is

$$I_{sp} = \frac{\langle v \rangle}{g}, \quad (2)$$

where g is the acceleration due to gravity on earth. From the kinetic energy relationship, the mean specific charge ($\langle q/m \rangle \equiv \langle c \rangle$) is

$$\langle q/m \rangle = \frac{\langle v^2 \rangle}{2V}, \quad (3)$$

where $\langle v^2 \rangle$ is the mean square velocity. The current is given by

$$I = \langle q/m \rangle \dot{m}. \quad (4)$$

The specific charge efficiency which is a measure of thrust degradation due to the specific charge distribution is given by

$$\eta = \frac{\langle c^{1/2} \rangle^2}{\langle c \rangle} = \frac{\langle v \rangle^2}{\langle v^2 \rangle} \quad (5)$$

where $\langle c^{1/2} \rangle^2$ is the square mean root specific charge. The relationship between these parameters can be summarized by the following expressions which shows their interrelation:

$$T = \dot{m} g I_{sp}, \quad (6)$$

and

$$\eta_{IV} = T^2 / 2\dot{m}, \quad (7)$$

where η_{IV} is the beam power. A nomograph of thrust versus specific impulse is shown in Figure 1 for constant values of \dot{m} and η_{IV} . In the above equations it is assumed that energy losses other than those due to the specific charge distribution are negligible. In general, T versus I_{sp} curves for a thruster will not follow constant \dot{m} or η_{IV} lines because of the complexity of the relationship with other factors such as temperature, geometry, and propellant properties. This complexity dictated that parametric analysis of the data would be the most profitable way to investigate colloid thrusters. The main emphasis was placed on the variation of T , I , and I_{sp} as a function of \dot{m} , V , and temperature for a given thruster and propellant combinations.

2.2 EXPERIMENTAL TECHNIQUES

The experimental investigations were aimed at understanding the way control variables V , \dot{m} , temperature, geometry, and propellant properties affect the operational parameters I , $\langle q/m \rangle I_{sp}$, T , and η . Time-of-flight (TOF) analysis of the charged particles as a function of the control variables was the primary method used to obtain these relationships. TOF analysis is a means of determining the velocity distribution of the particles from which the operational parameters may be calculated. This subsection details the experimental arrangement, instrumentation, and data reduction techniques used in this program.

2.2.1 EXPERIMENTAL ARRANGEMENT

The experimental apparatus for examining emitter operation includes a 2-foot diameter by 3-foot long vacuum system, high voltage power supplies, high voltage switch, current and voltage meters, current

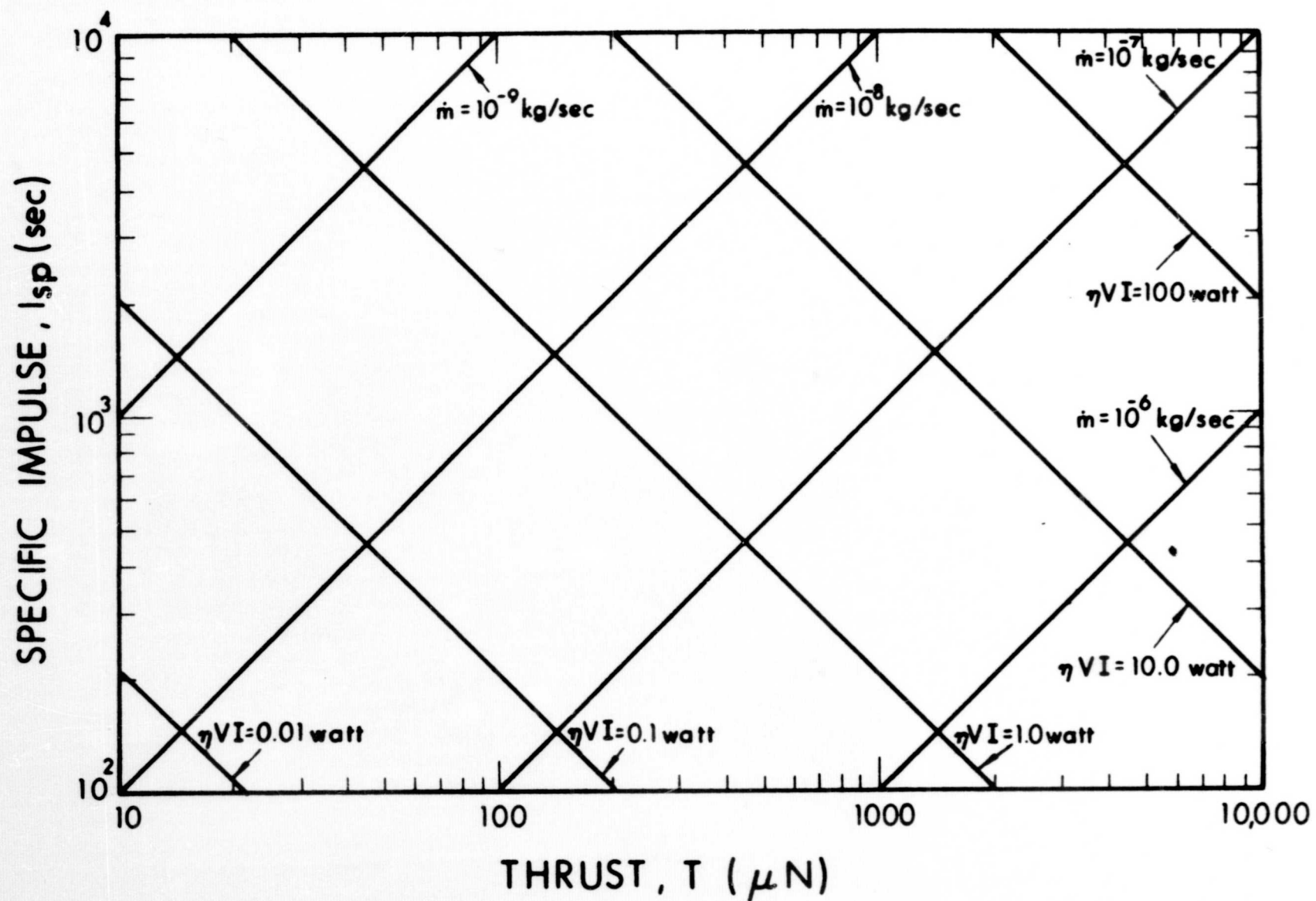


Figure 1. Specific Impulse versus Thrust

collectors, the analog to digital data acquisition system (DAS), and an oscilloscope. A schematic diagram of a typical arrangement is shown in Figure 2. The propellant is fed to the emitter from a pressurized reservoir that is located outside the vacuum chamber. Charged particles are generated and accelerated by applying a high positive voltage (10 kV to 18 kV) to the emitter with the extractor electrodes at negative potentials. The emitter potential is measured directly with an electrostatic voltmeter. The current to two TOF collectors that are 50 cm from the emitter is monitored in parallel by an oscilloscope and the DAS. TOF data is obtained by shorting the high voltage to ground using a switching circuit which provides a sync signal for both the oscilloscope and the DAS. The sync signal initiates the TOF trace on the oscilloscope which can be recorded using a scope camera. At the same time the DAS converts the analog current signal to digital points that are subsequently stored on paper tape. The data from the tape is fed into a Sigma 7 computer which is used to calculate both the operational parameters and mass flowrate. The computer can also provide plots of the operational parameters as a function of \dot{m} for different values of V .

2.2.2 APPARATUS AND INSTRUMENTATION

2.2.2.1 Vacuum System

The vacuum system used for most of these tests is a 2-foot diameter by 3-foot long vacuum chamber containing a liquid nitrogen cooled liner and both a 10-inch and 6-inch diffusion pump with liquid nitrogen cooled baffles (see Figure 3). This system has a sufficiently high pumping speed to provide pressures in the 10^{-6} to 10^{-5} torr range during thruster operation. A smaller 1-foot diameter by 3-foot long chamber is used for some auxiliary tests.

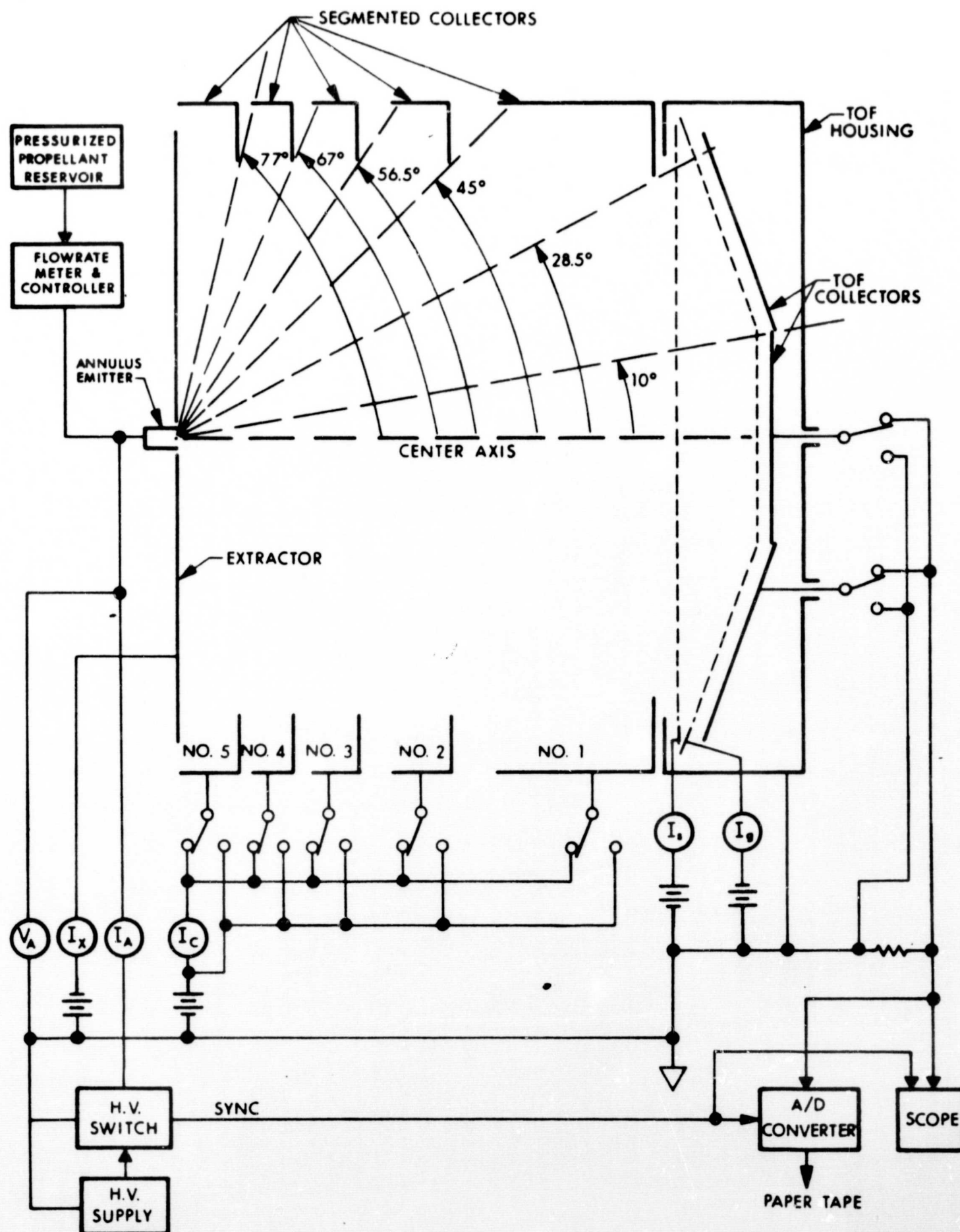


Figure 2. Schematic Diagram of Experimental Setup

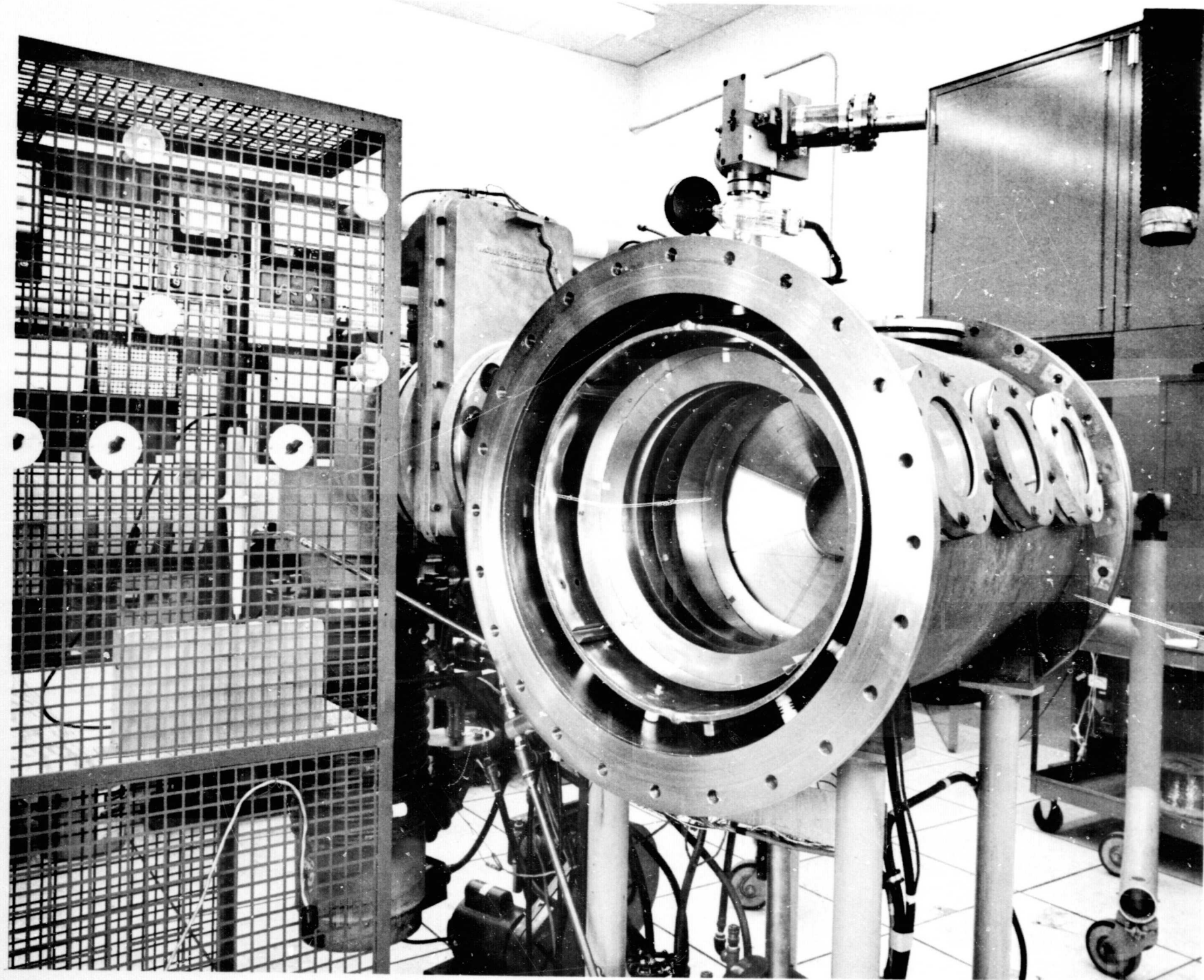


Figure 3. 2 foot by 3 foot Vacuum Chamber Showing Colloid Instrumentation

2.2.2.2 Current Collectors

The beam collector system consists of a set of segmented cylindrical collectors (Figure 4) and a set of two concentric TOF collectors (Figure 5). A schematic arrangement of the collectors was shown in Figure 2. The TOF collectors have one grid to suppress secondary electrons and a second grid to act as an electrostatic shield. The center section subtends a half angle of 10° and the outer section subtends from 10° to 30° . This corresponds to solid angles of 0.095 and 0.675 steradian, respectively. Separate, coaxially shielded leads for the two sections are brought out of the vacuum chamber so that TOF data to the collectors can be measured separately or simultaneously.

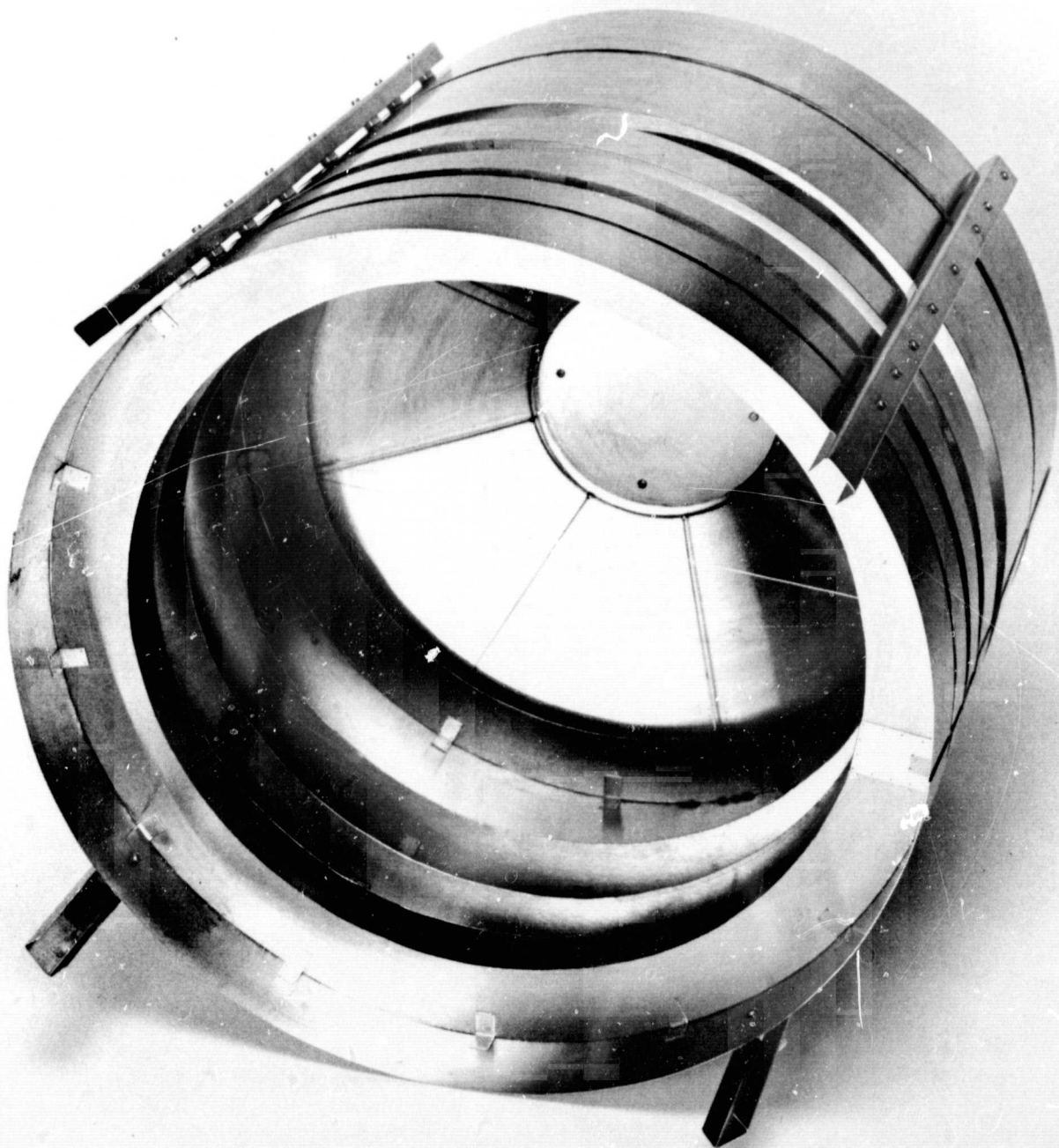
2.2.2.3 TOF Data Acquisition System

An analog to digital data acquisition system (DAS) was designed using IC digital logic modules (Xerox Data Systems' T Series) to obtain TOF data automatically. These data are stored on an 8-level paper tape in binary form and analyzed using a Sigma 7 computer. The DAS consists of an 8-bit analog to digital converter, buffer memory, pulse generator, timing and control logic, address accumulator, digital to analog converter, and paper tape punch. The DAS has three modes of operation; digitize, punch, and display.

a. Digitize Mode

In the digitize mode, shown in Figure 6, the TOF data are digitized at a rate determined by the pulse generator setting. The data are then stored in a 32-word (8 bits per word) buffer memory. The pulse generator is in an externally gated mode so that digitize command pulses are produced only when both the external gate and memory-ready signals are true.

The memory-ready signal is made true by resetting the memory address. It will remain true until the memory is full. The memory is arranged so that after the last memory location, it is advanced to the first location. As new data are read in, the previous data are destroyed. Therefore, the memory-ready signal prevents the memory from making more than one cycle and thereby destroying the initial data points.



96927

Figure 4. Segmented Cylindrical Collector

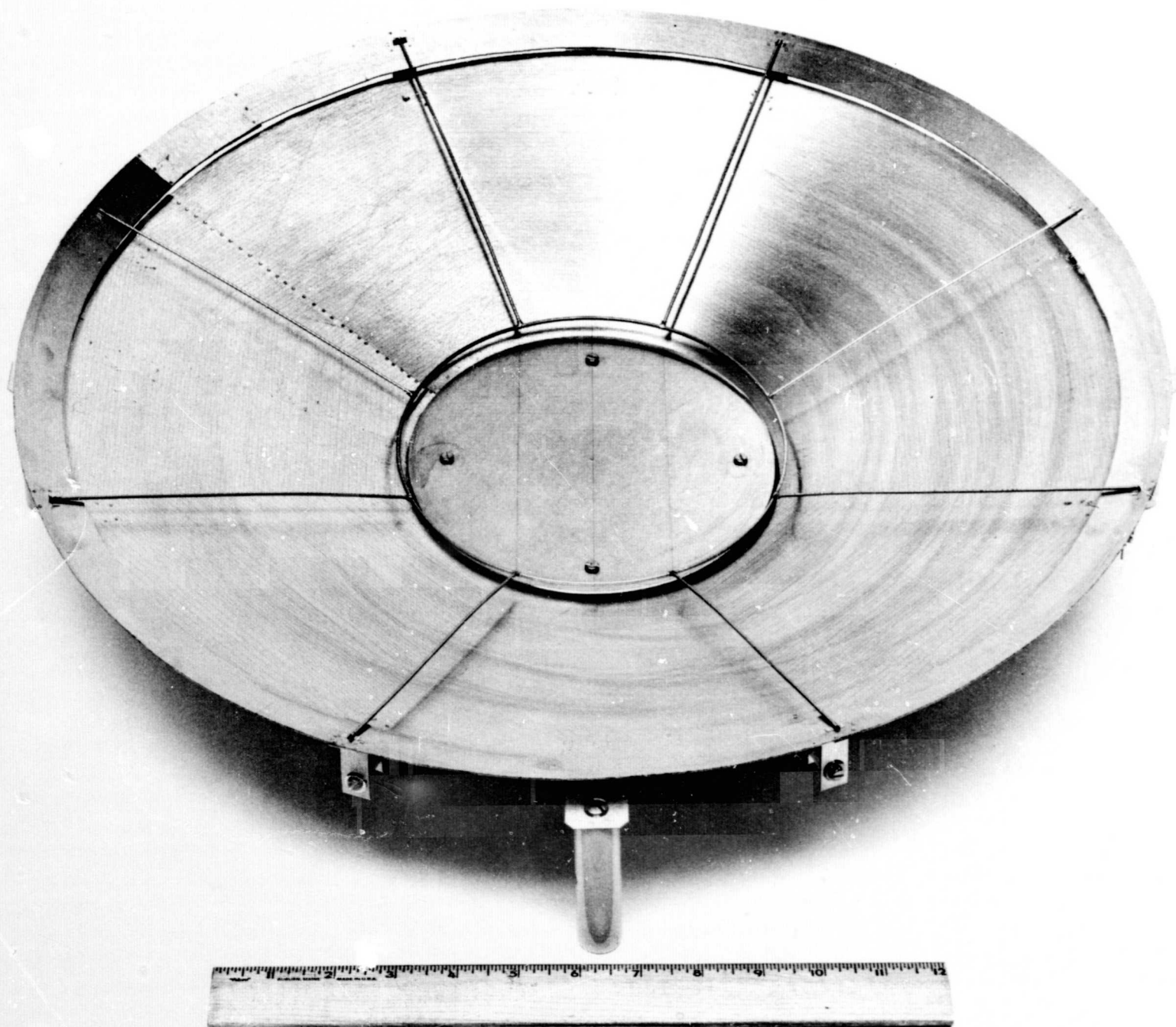


Figure 5. Segmented TOF Collector

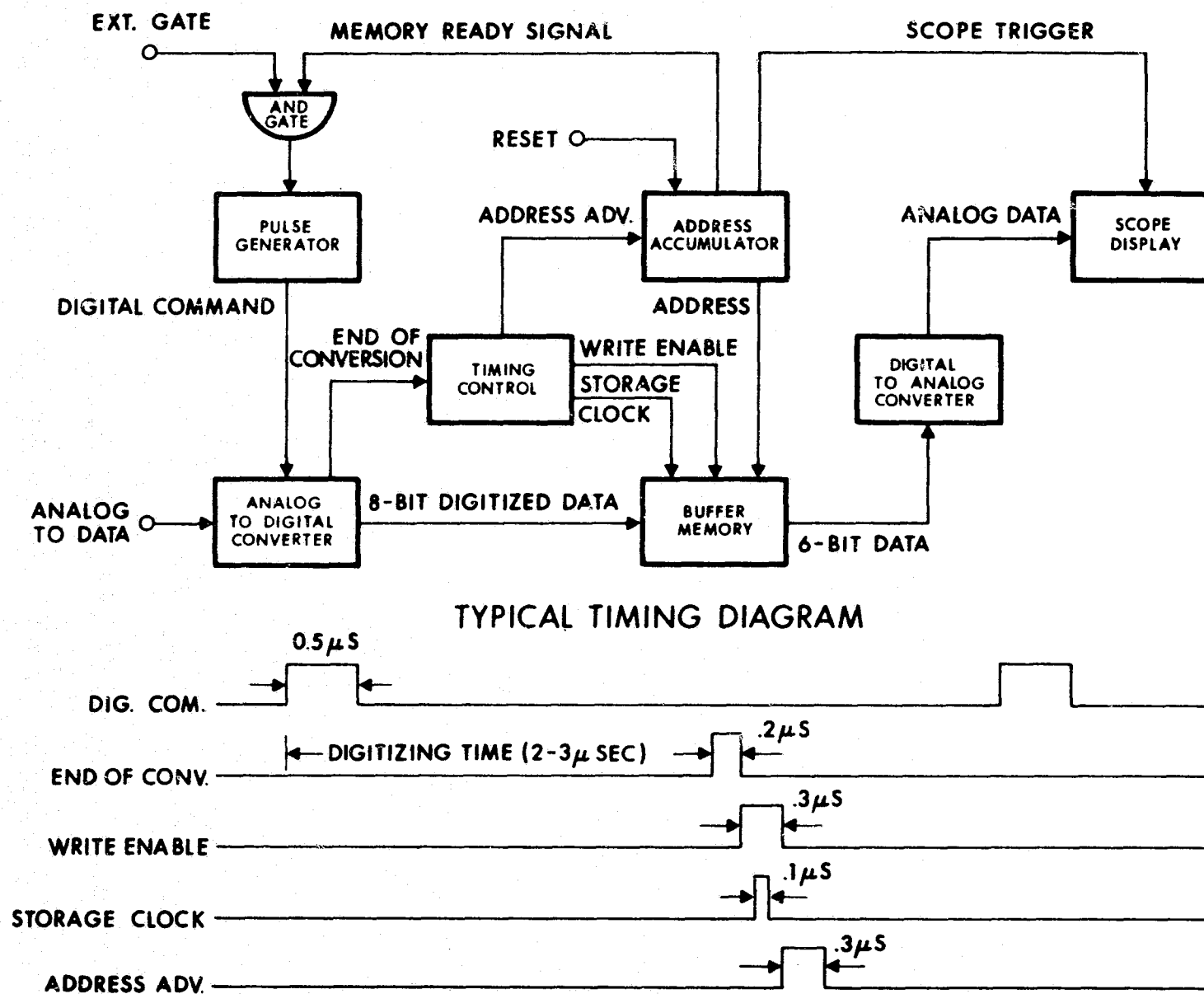


Figure 6. Block Diagram of Digitize Mode

The external gate signal is generated by the oscilloscope time base gate which is true whenever the time base is making a sweep. Figure 7 shows how the thyatron switch, which initiates the TOF data, and the data acquisition system are synchronized. A sync pulse triggers the oscilloscope, causing the time base gate to be true for the duration of the oscilloscope sweep and initiating the digitizing process. After a given delay, which is adjustable, a delayed pulse triggers the thyatron which shorts the high voltage-to-ground to start the TOF data. The result is that during the delay time, the initial current level is digitized after which the TOF data are digitized. After each data point is digitized, it is stored in the buffer memory in coincidence with the write-enable and storage-clock signals. The memory is then advanced to the next location until all the memory locations are filled.

b. Punch Mode

In the punch mode, shown in Figure 8, the contents of the memory are punched onto paper tape in sequential order, starting with the first location. The pulse generator is in an external trigger and gated mode. A 5 Hz pulse generator provides the triggering signal and the address accumulator provides the gate signal. The gate signal is made true by resetting the address. The memory clock is slaved to the 5 Hz triggering signal and advances the address to the next location. After a 10-millisecond delay, a delayed pulse is produced which activates the teletype and causes it to punch the contents of that memory location onto paper tape. This continues until the entire memory is read out onto paper tape.

c. Display Mode

In the display mode, shown in Figure 9, the memory is continuously cycled at a rate determined by the pulse generator. An oscilloscope trigger is produced whenever the first memory address is generated. This synchronizes the oscilloscope sweep with the memory cycle. The six most significant bits of the memory content are converted to an analog signal and fed to the input of the oscilloscope to display the TOF trace.

2.2.2.4 Thyatron Switch Circuit

In conjunction with the DAS, an electronic method of triggering the emitter high voltage-to-ground potential was developed. The initial circuit had a hydrogen-filled thyatron connected between the high voltage and ground. A pulse forming network which used a silicon controlled rectifier (SCR) as a trigger was connected to the grid of the

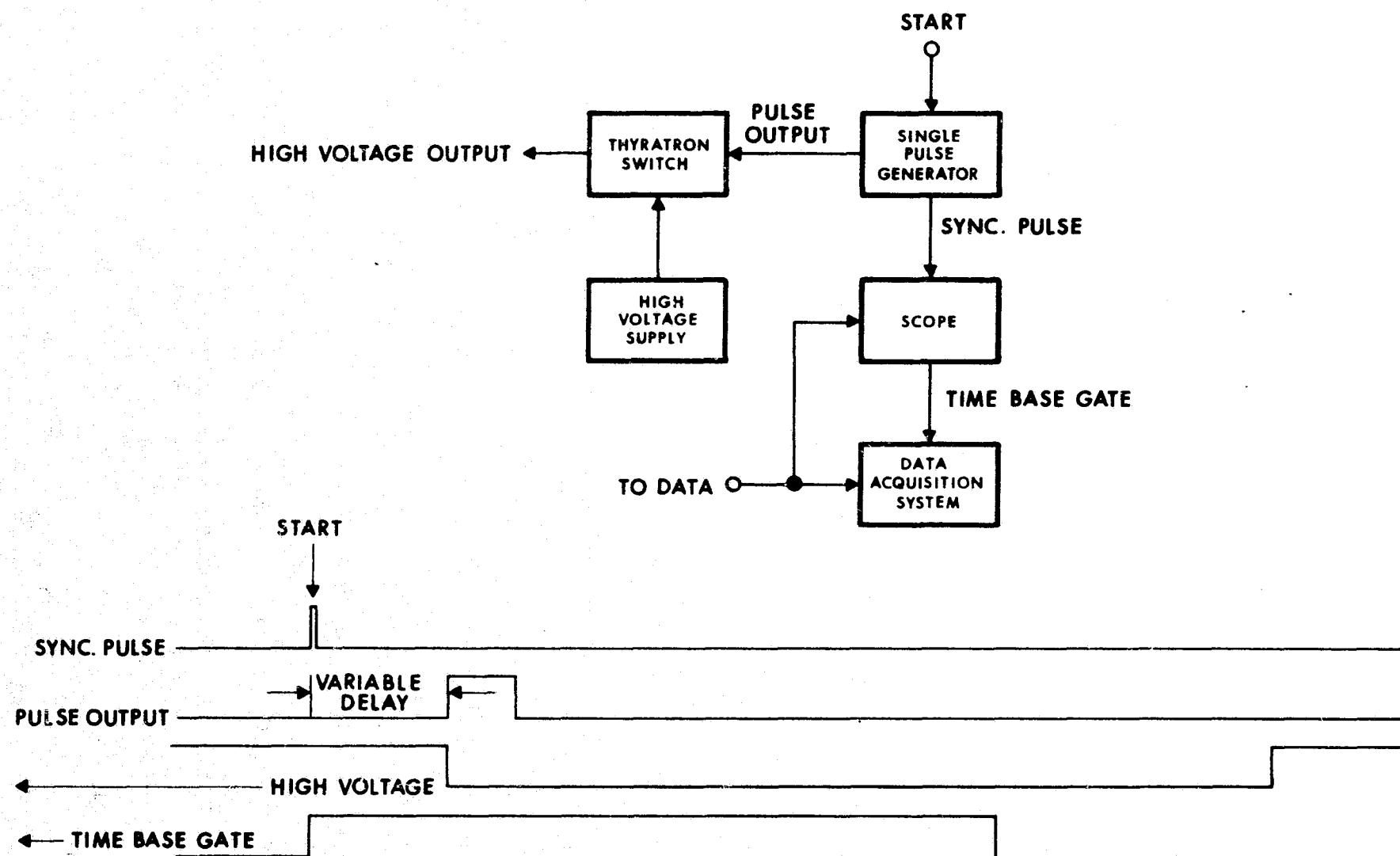


Figure 7. Block Diagram of Thyatron Switch and Data Acquisition Synchronization

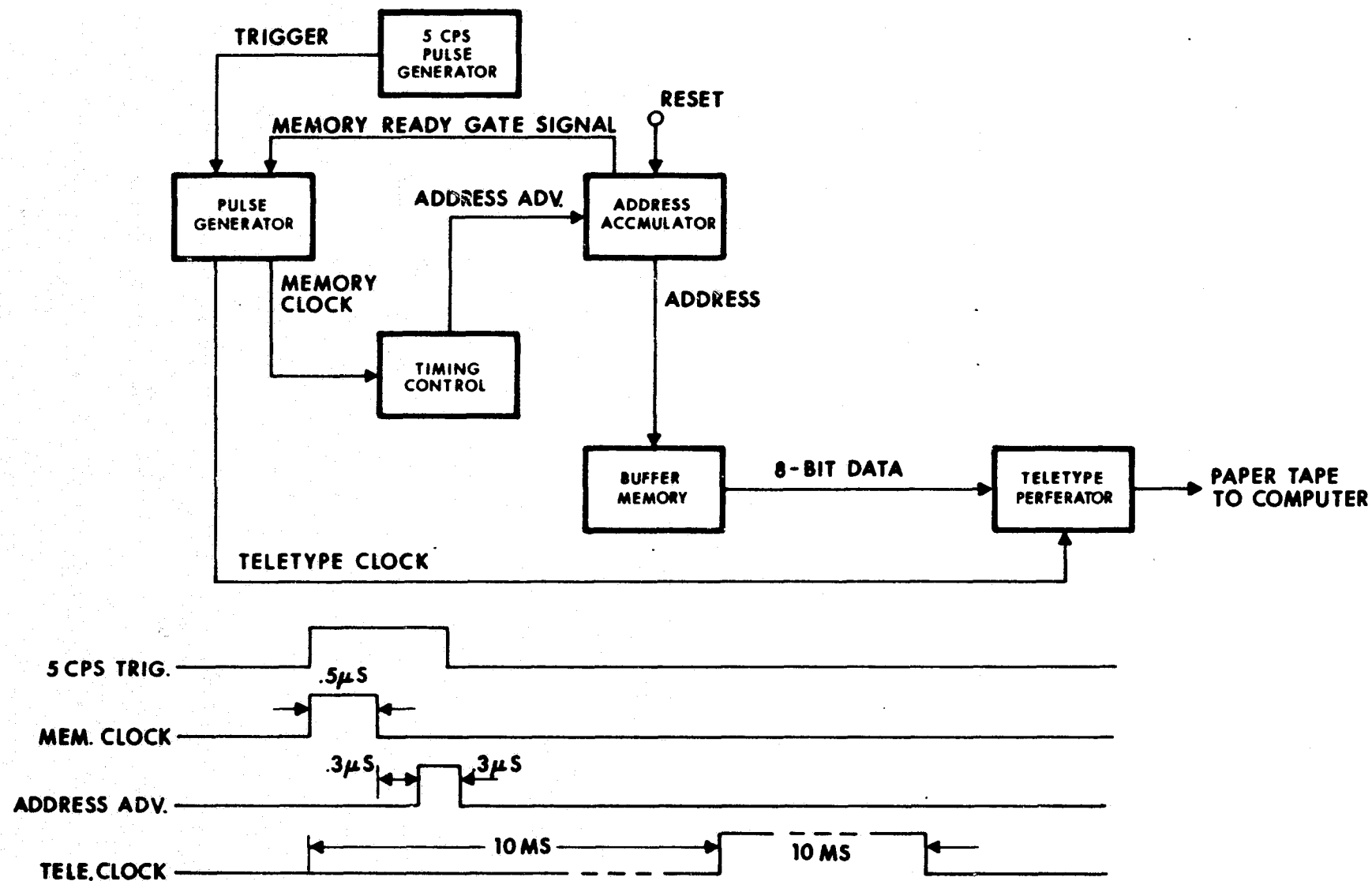


Figure 8. Block Diagram of Punch Mode

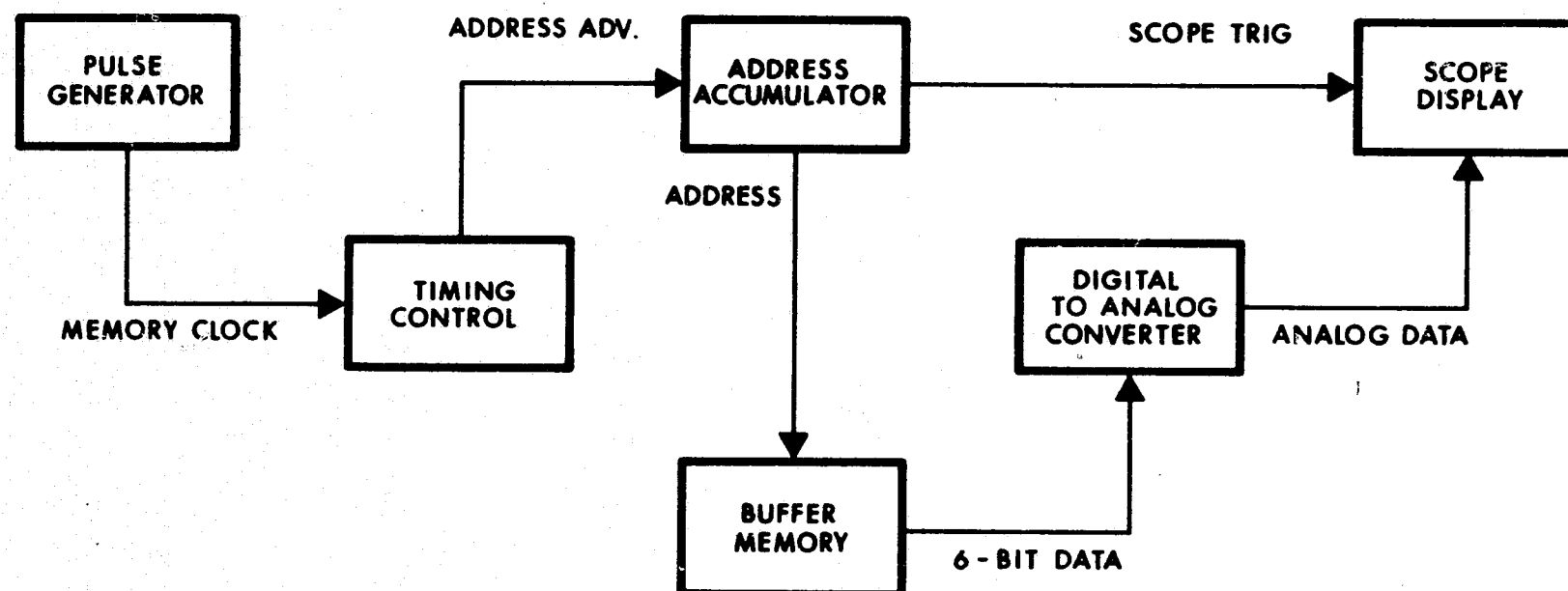


Figure 9. Block Diagram of Display Mode

thyatron. A control pulse applied to the gate of the SCR allowed a positive voltage pulse to appear on the grid; this rendered the tube conductive and effectively reduced the anode (emitter) potential to ground. The current from the power supply was determined by the voltage and the value of the resistance R, since the impedance of the tube is small when conductive. The amount of current flowing through the tube had to be above a critical value to maintain the anode near ground potential. For too low a current, the anode potential repeatedly rose to above +500V and then dropped to ground again, with a mean time interval between voltage swings of about 10 μ sec. This train of voltage pulses produced a corresponding train of pulses on TOF traces. Above the critical current the TOF traces appeared clean.

The general features described above are shown in Figure 10. This figure also reflects a modification made to the high voltage power supply which turns the high voltage supply off when the thyatron fires. This is accomplished by using the built-in overcurrent protection relay in the supply to automatically turn the high voltage off for about 1/4 second, to render the thyatron nonconductive, then turn the high voltage back on again.

2.2.2.5 Propellant Flowmeter and Controller

This subsection describes the effort on an EOS-funded program to develop a breadboard propellant flowmeter, flow controller, and high-voltage electronics package for colloid sources. The effort to date has been directed toward developing a device which would meter and control the propellant (glycerol) flowrate over a range from 10 to 100 μ g/sec. The device consists of a flowmeter, flow controller, and electronic package. The electronic package contains the high-voltage power supply as well as the electronics for the meter and controller.

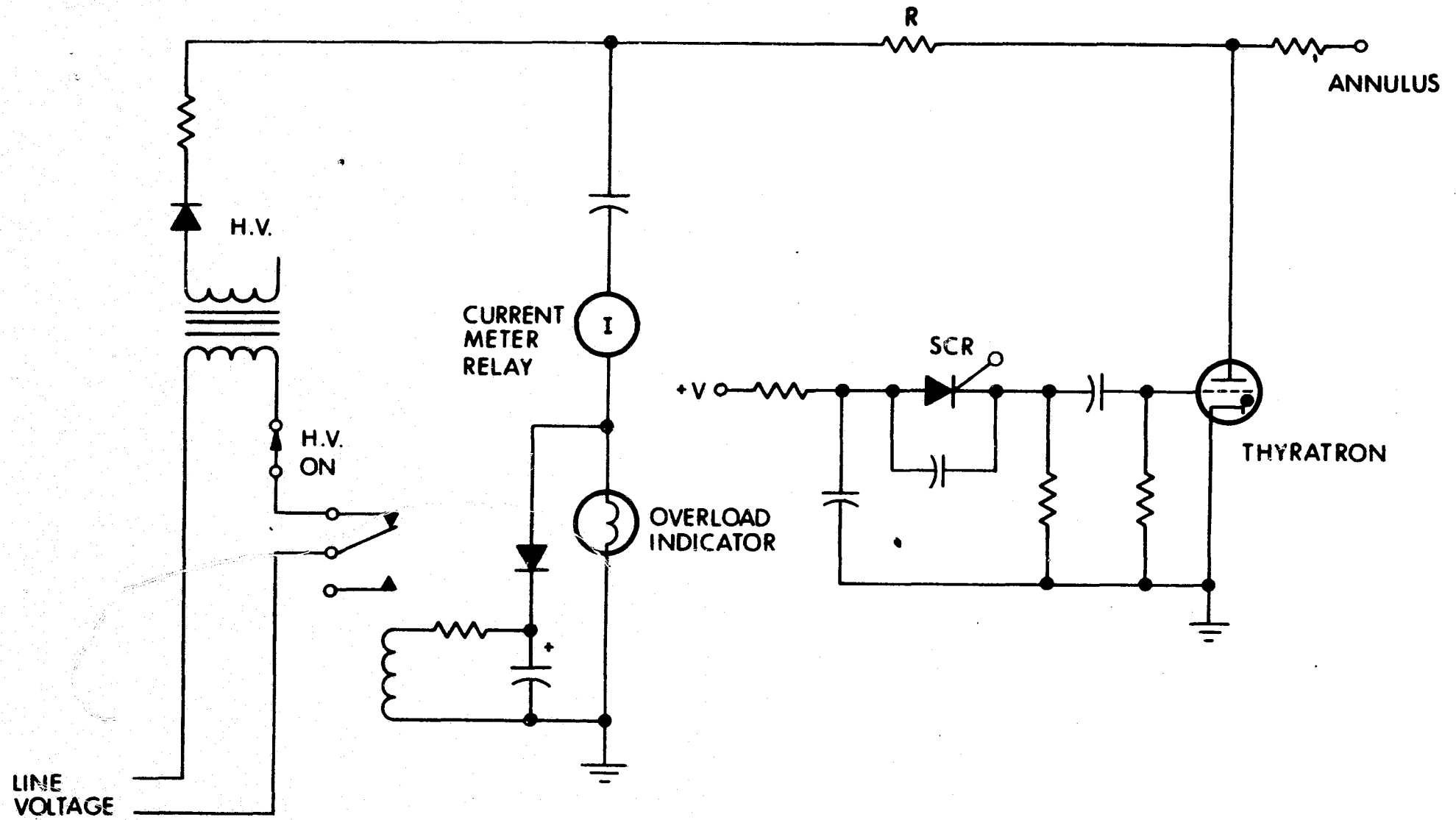


Figure 10. Thyatron Switch Circuitry

A schematic diagram of the flowmeter and controller is shown in Figure 11. The flowmeter consists of a small-bore stainless steel capillary tube which is heated in the center. The temperature difference ($T_2 - T_1$) between points symmetrically located on either side of the heated area is an indicator of propellant flowrate and is calibrated as such. Sensistors are used as the temperature-sensing devices in the flowmeter to detect propellant flow. They are available as very small cubes, and have a reproducible and stable temperature coefficient of about 0.7 percent/ $^{\circ}\text{C}$.

The two sensistors are connected in a bridge configuration with a potentiometer used to balance the sensistor voltages before any flow occurs. The output of the bridge is connected to an operational amplifier in a differential configuration. This amplifier has a controlled gain of 100, and an output that is a measure of propellant flow. This output is compared to a manually selected reference voltage in a second operational amplifier. The output of this amplifier is a measure of the difference between the measured flowrate and a reference signal, and is used as the error signal in a closed-loop flow control system.

The flow controller consists of a second small-bore capillary tube that is electrically heated to warm the propellant and lower its viscosity. This increases the flowrate because the controller is designed to be the limiting flow impedance in the propellant feed line. The temperature dependence of the viscosity of the propellant base (glycerol) is such that a 30°C temperature change produces an order of magnitude change in flowrate. Temperature effects on propellant viscosity is discussed in detail in Subsection 3.2.1.

Using a glass capillary tube for absolute flowrate determination, the flow controller was shown to control glycerol flow over the design range of 10 to 100 $\mu\text{g}/\text{second}$. Closed-loop tests were conducted, and it was shown that the feedback loop was stable and controlled flowrate to a constant level.

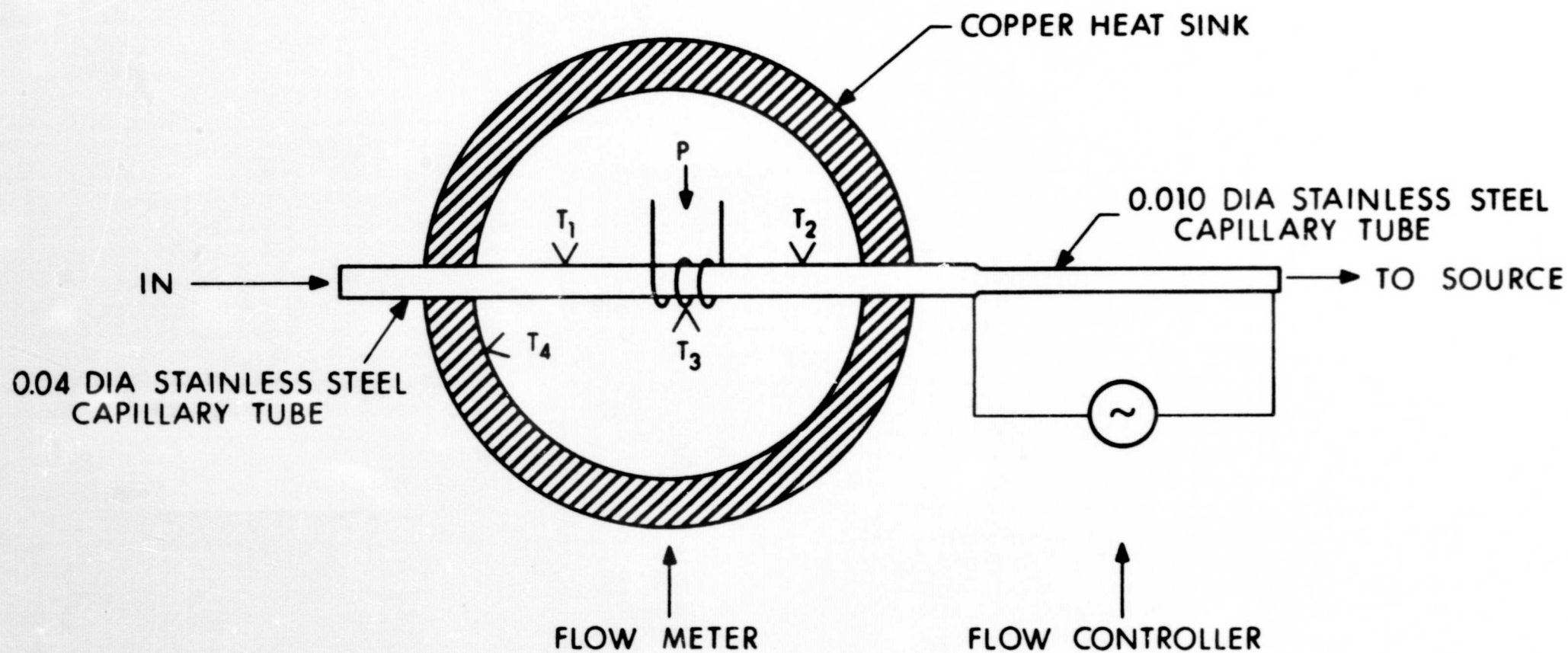


Figure 11. Propellant Flow Meter and Control Device

2.2.2.6 Photomicrographic Equipment

A complete Reichart photomicrographic system (Figure 12) and darkroom facilities were used to take photographs of the emitter edges. Magnifications from 50 to 3500X are available with this equipment. This equipment was used to examine emitter edges before and after operation as part of a standard testing procedure.

2.2.3 DATA REDUCTION

Data reduction involves the computation of \dot{m} and the operational parameters from the TOF data. TOF data is a function of i versus t where i is the current to the TOF collectors and t is time (initiated when the emitter voltage is shorted to ground). The current starts at some initial value i_0 and goes to zero in a manner determined by the velocity distribution of the charged particles. Examples of TOF traces are shown in Figure 13 a through e. The shape of the TOF traces determines the thrust efficiency. Figure 13a is an example showing a very high efficiency and Figure 13b is an example showing low efficiency. Figure 13c shows the TOF traces obtained by monitoring the inner and outer TOF collectors separately and in parallel. This type of data can be used to obtain a rough spatial distribution. Thrust is directly proportional to the area under the TOF trace. Figure 13d is an example showing a relatively large thrust. Specific impulse is inversely proportional to the time centroid. Figure 13e is an example of a relatively high specific impulse.

The following relationships were used to compute \dot{m} and the operational parameters (where L is the distance between the emitter and TOF collector, V is the emitter voltage, I is the emitter current, A is the area under the TOF trace, t_c is the time centroid of the TOF trace, g is the acceleration due to gravity, and ϵ is the collection efficiency, i_0/I):

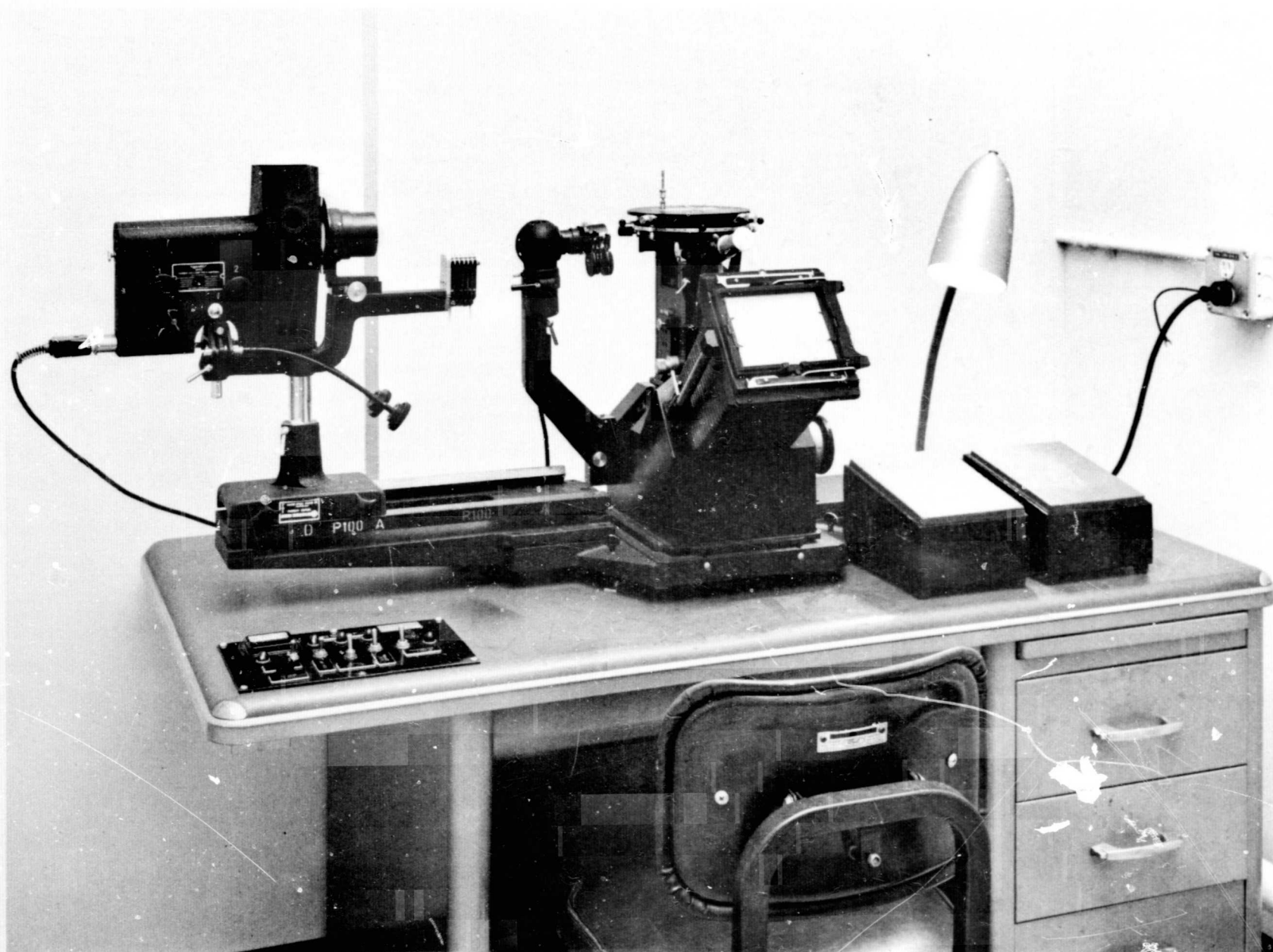
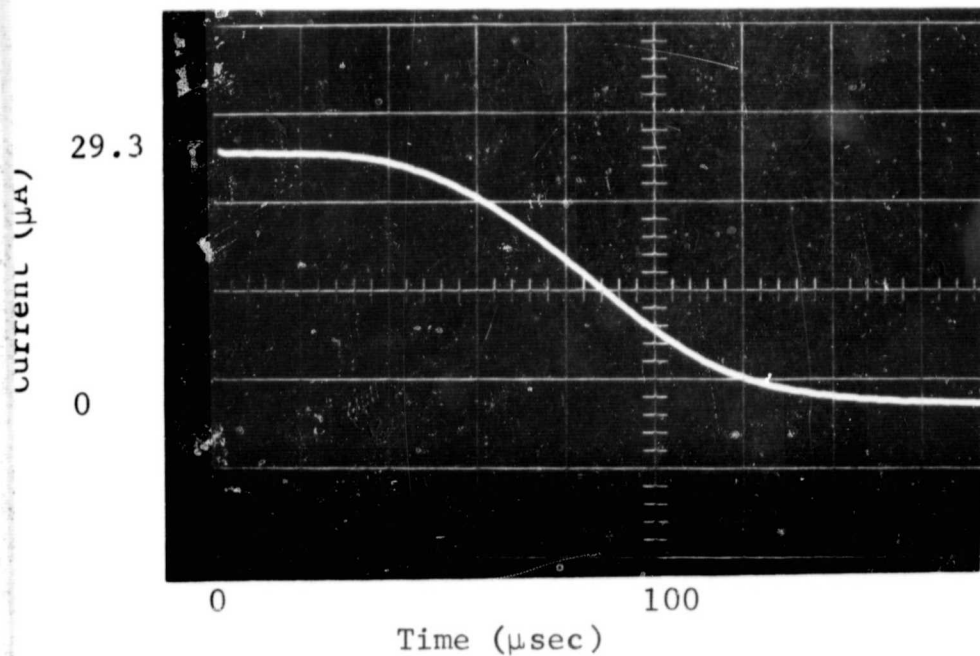
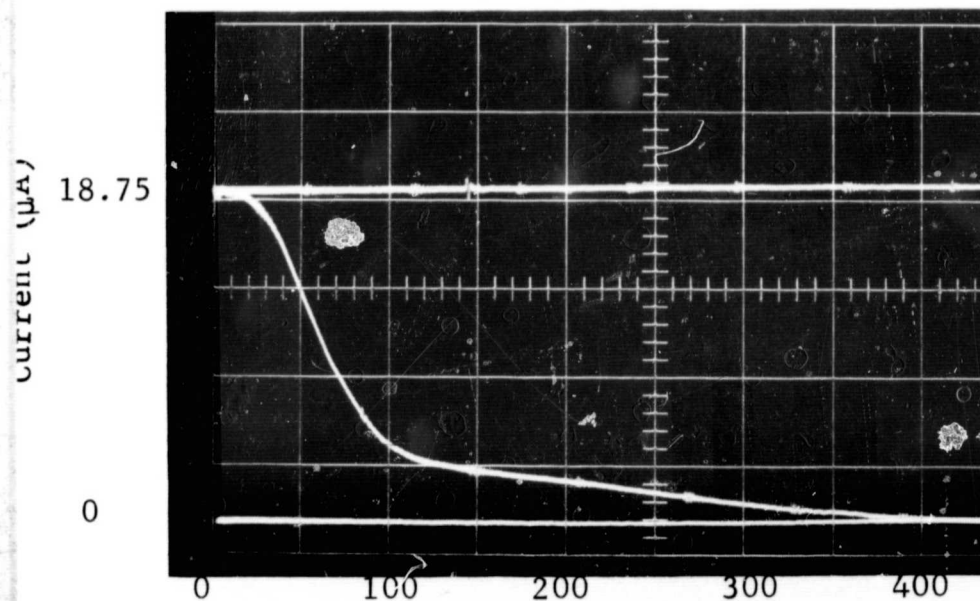


Figure 12. Photomicrographic Equipment



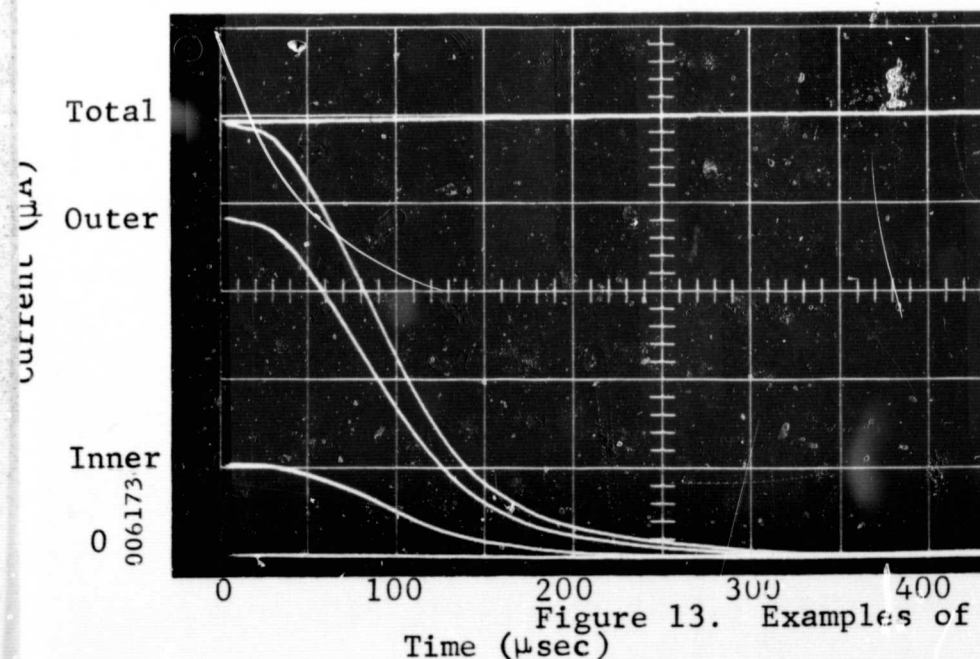
(a)

$V = 14.0 \text{ kV}$
 $I = 56.0 \text{ } \mu\text{A}$
 $i_o = 29.3 \text{ } \mu\text{A}$
 $\eta = 92.1\%$
 $I_{sp} = 665 \text{ sec}$
 $T = 50 \text{ } \mu\text{lb}$



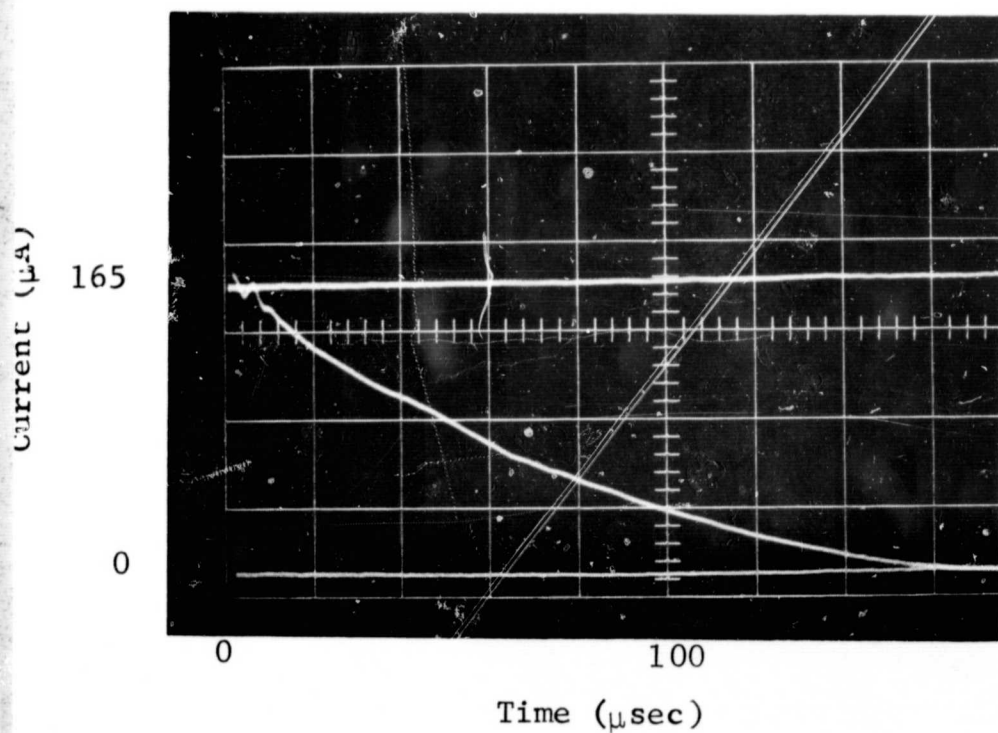
(b)

$V = 14.0 \text{ kV}$
 $I = 21.0 \text{ } \mu\text{A}$
 $i_o = 18.75 \text{ } \mu\text{A}$
 $\eta = 55.7\%$
 $I_{sp} = 305 \text{ sec}$
 $T = 24.5 \text{ } \mu\text{lb}$

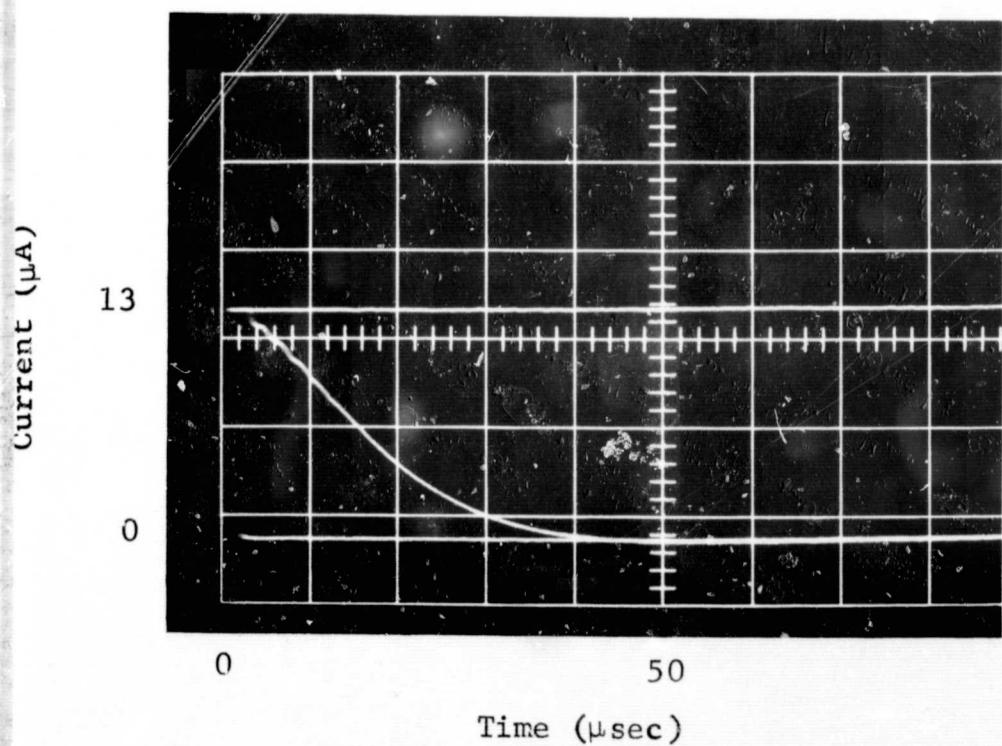


$V = 9.0 \text{ kV}$
 $I = 80.0 \text{ } \mu\text{A}$
 $i_o \text{ (total)} = 49.0 \text{ } \mu\text{A}$
 $\text{ (outer)} = 38.2 \text{ } \mu\text{A}$
 $\text{ (inner)} = 10.3 \text{ } \mu\text{A}$
 $\eta \text{ (total)} = 76.7\%$
 $\text{ (outer)} = 77.4\%$
 $\text{ (inner)} = 84.2\%$
 $I_{sp} \text{ (total)} = 367 \text{ sec}$
 $\text{ (outer)} = 385 \text{ sec}$
 $\text{ (inner)} = 335 \text{ sec}$
 $T \text{ (total)} = 69 \text{ } \mu\text{lb}$

Figure 13. Examples of TOF Traces (sheet 1 of 2)



$V = 13.0 \text{ kV}$
 $I = 242.2 \text{ } \mu\text{A}$
 $i_o = 165.0 \text{ } \mu\text{A}$
 $\eta = 66.6\%$
 $I_{sp} = 554 \text{ sec}$
 $T = 174 \text{ } \mu\text{lb}$



$V = 14.9 \text{ kV}$
 $I = 87.0 \text{ } \mu\text{A}$
 $i_o = 13.0 \text{ } \mu\text{A}$
 $\eta = 74.3\%$
 $I_{sp} = 1196 \text{ sec}$
 $T = 16 \text{ } \mu\text{lb}$

006174

Figure 13. Examples of TOF Traces (sheet 2 of 2)

$$A = \int i \, dt \quad (8)$$

$$t_c = A^{-1} \int t \, i \, dt \quad (9)$$

$$T = \frac{2 \, V \, A}{\epsilon \, L} \quad (10)$$

$$I_{sp} = \frac{L}{2 \, t_c \, g} \quad (11)$$

$$\dot{m} = \frac{4 \, V \, A \, t_c}{\epsilon \, L^2} \quad (12)$$

$$\langle q/m \rangle = \frac{i_o \, L^2}{4 \, V \, A \, t_c} \quad (13)$$

$$\eta = \frac{A}{2 \, i_o \, t_c} \quad (14)$$

A computer program was used to perform these computations. The subroutine which calculates the TOF trace area and time centroid uses Simpson's rule or Newton's rule (Ref. 7) or both together. The reduced data is printed out in tabular form and operational parameters are plotted as a function of \dot{m} for each value of V .

2.3 THRUSTER DESIGN

2.3.1 EMITTER CONFIGURATIONS

The annulus geometry has evolved through various stages of development. The critical aspects of geometry which strongly determine the mechanics of particle generation and acceleration are the emitter edge dimensions and gap spacings. The effects of surface condition on particle generation are not well understood at present. Of lesser importance

dimensionally are the propellant feed channels built into the annulus body. However, it is desirable to provide an annular plenum (of large dimensions compared to gap spacings) within the annulus so that surface tension forces are more favorable to ensure an even supply of propellant over the entire tip circumference.

The importance of restricting propellant massflow to achieve higher specific impulse became evident in early annulus investigations. Mass flow instability at the annulus resulted from heating of the emitter and made control of mass flowrate difficult. As a consequence of this instability, efforts were initiated to provide restrictive elements located away from the emitter edge. The efforts included in-line filters and capillary tubing restrictive elements placed between the feed system and annulus.

Further attempts to control annulus flow impedance resulted in an annulus design incorporating a restrictive shelf containing flow grooves which were built into the main body of the annulus. This further increase in impedance led to the discovery of the emission limited region of operation at low mass flowrates. The basic annulus structure before assembly (note the shelf containing the flow grooves) is shown in Figures 14 and 15.

Early annulus emitters had gap spacings between 0.001 and 0.002 inch. Recent testing has demonstrated that restricted flow obtained by metal-to-metal fits at the edge (or gap spacings less than 0.0005 inch) have resulted in good performance and control. Improved performance under restricted flow conditions (annulus A06) has led to the design and testing of other emitters having the restriction located at the edge.

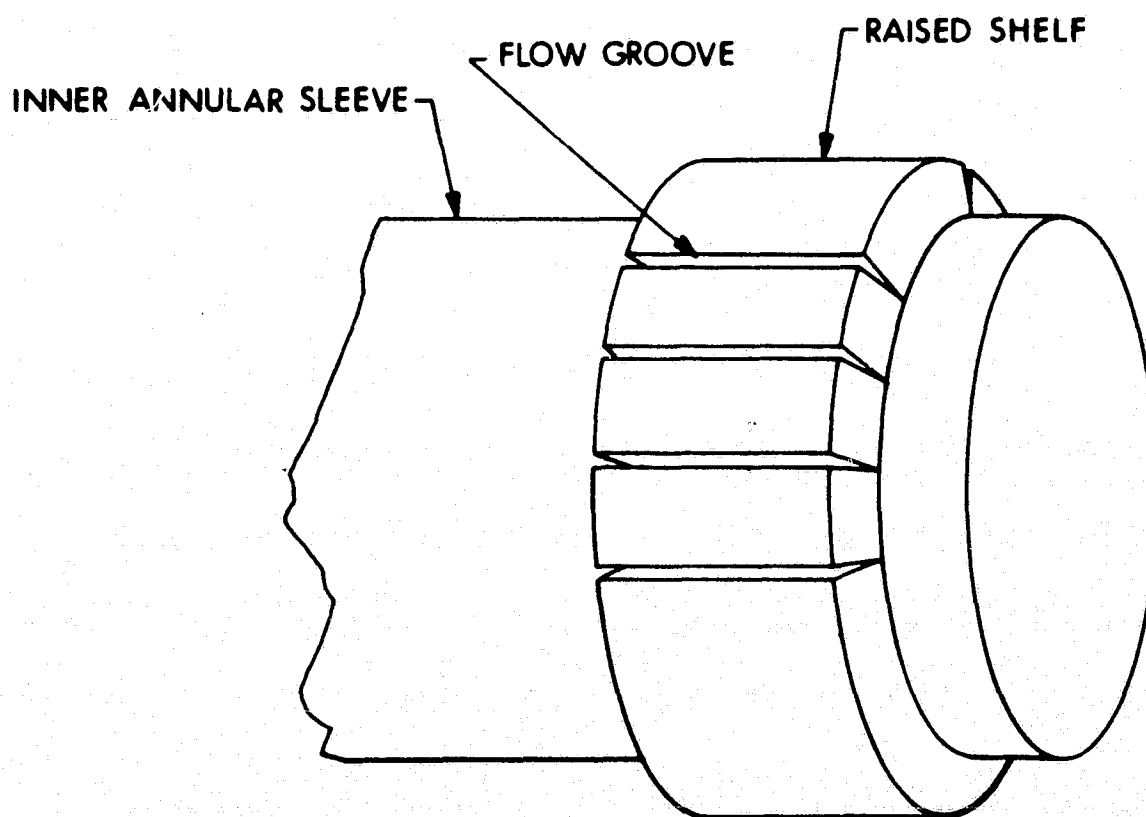
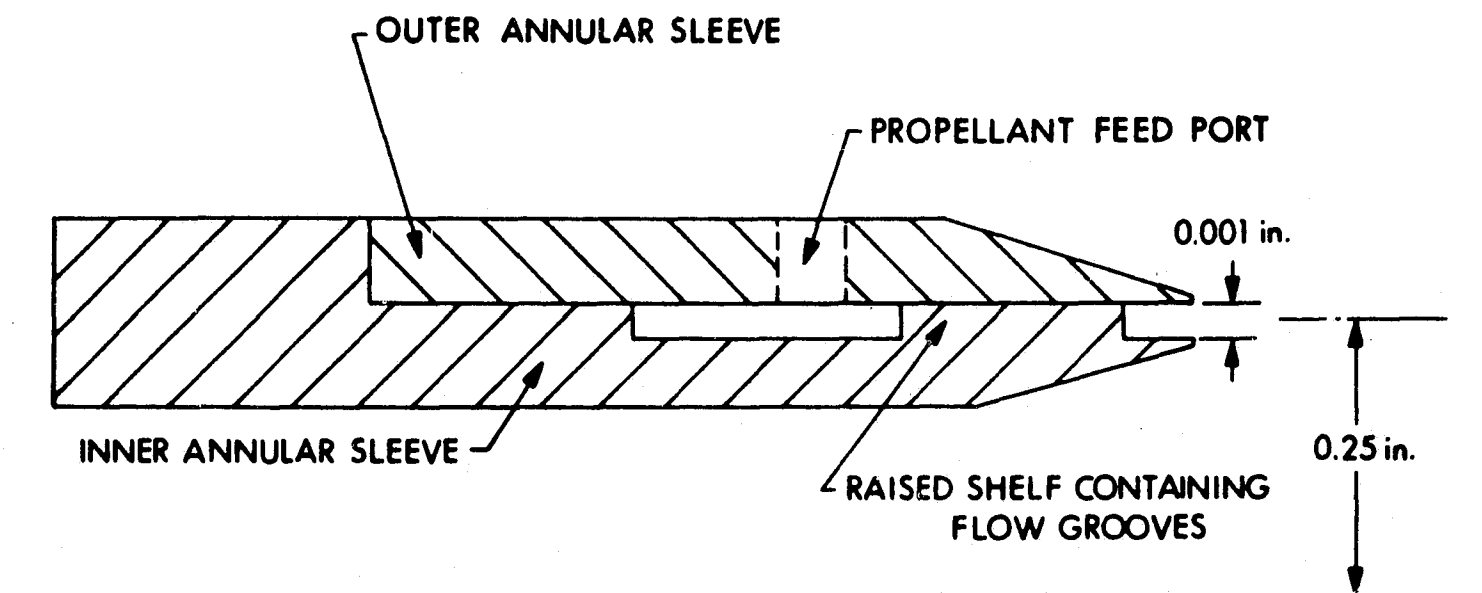


Figure 14. Inner Annulus Sleeve Showing Details of Flow Grooves

27076

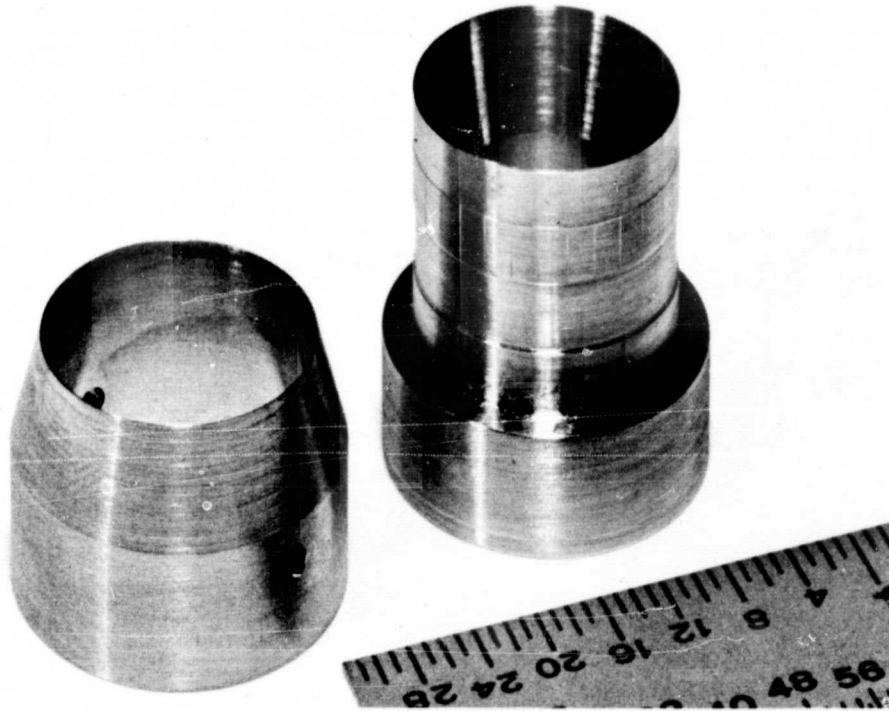


Figure 15. Inner and Outer Annulus Sleeving (Annulus A08)

The present approach to annulus design incorporates some of the features discussed above with slight variations. The gap spacing for annulus A06 was kept below 0.0005 inch and the gap length extended back approximately 0.050 inch. A photomicrograph of annulus A06 is shown in Figure 16. More recent annuli (A09 for example) have similar gap spacings extending back 0.100 inch. For annulus A06, the emitter edges were 0.002 inch to provide a flatter surface in contrast to the knife edges used previously. It was anticipated that this change would provide a more uniform and directional field across the emitter surface thereby enhancing the collection efficiency and specific charge efficiency. Subsequent testing of A06 supported the reasoning behind this design change. The disadvantage of broader emitter edges is the reduction of the electric field strength at the edges for a given voltage. Higher specific impulses can be obtained at comparable voltages by keeping the edge dimensions small as possible.

Figure 17 shows both a side and front view of the GSFC annular emitter. The emitter material is Carpenter No. 20 Cb3 stainless steel, with vapor deposited platinum inner and outer edges. The annular gap is 0.002 inch, and the inner and outer edges are nominally 0.0002 inch radii. The thruster assembly (which has no inner extractor) employs an outer extractor (not shown in Figure 17) with a gap of 0.23 inch between the annulus outer tip and inner surface of the extractor. While testing at GSFC, this extractor was positioned in the same plane as the thruster outer edge and was operated at -2 kV.

2.3.2 EMITTER MATERIAL AND FABRICATION

Annulus emitters constructed from stainless steel materials have presented no fabrication problems. They are formed entirely using standard machining techniques on a lathe with a microscope attachment to measure dimensions accurately. Techniques for fabricating emitters from thoriated tungsten and platinum/iridium materials have required more development.

006175

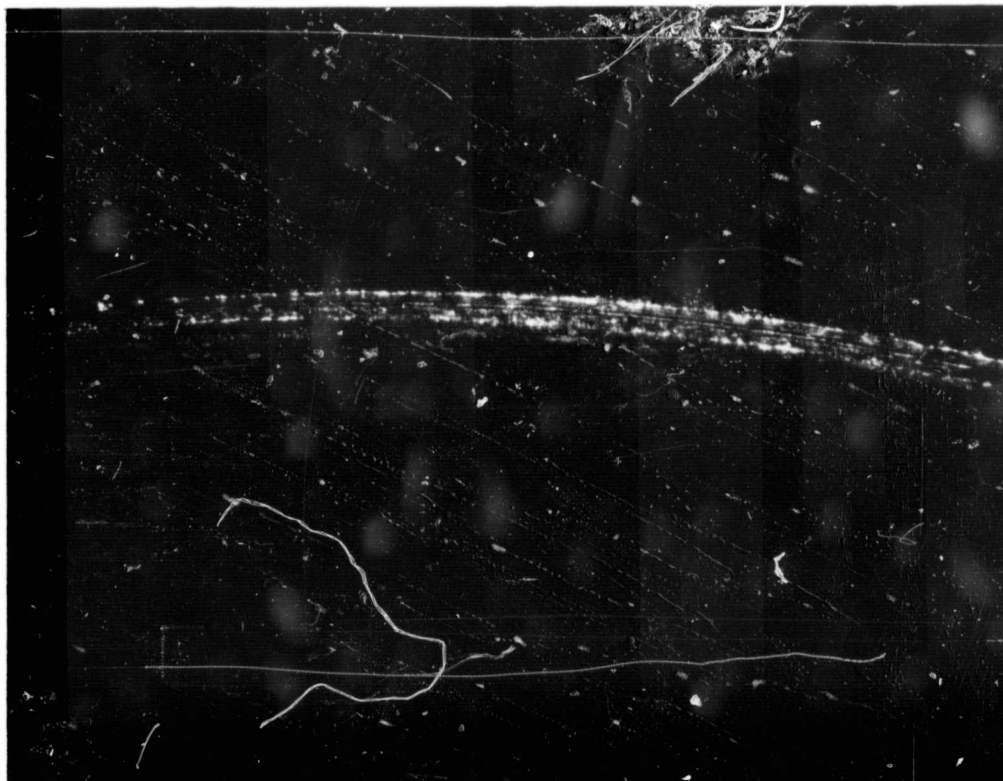
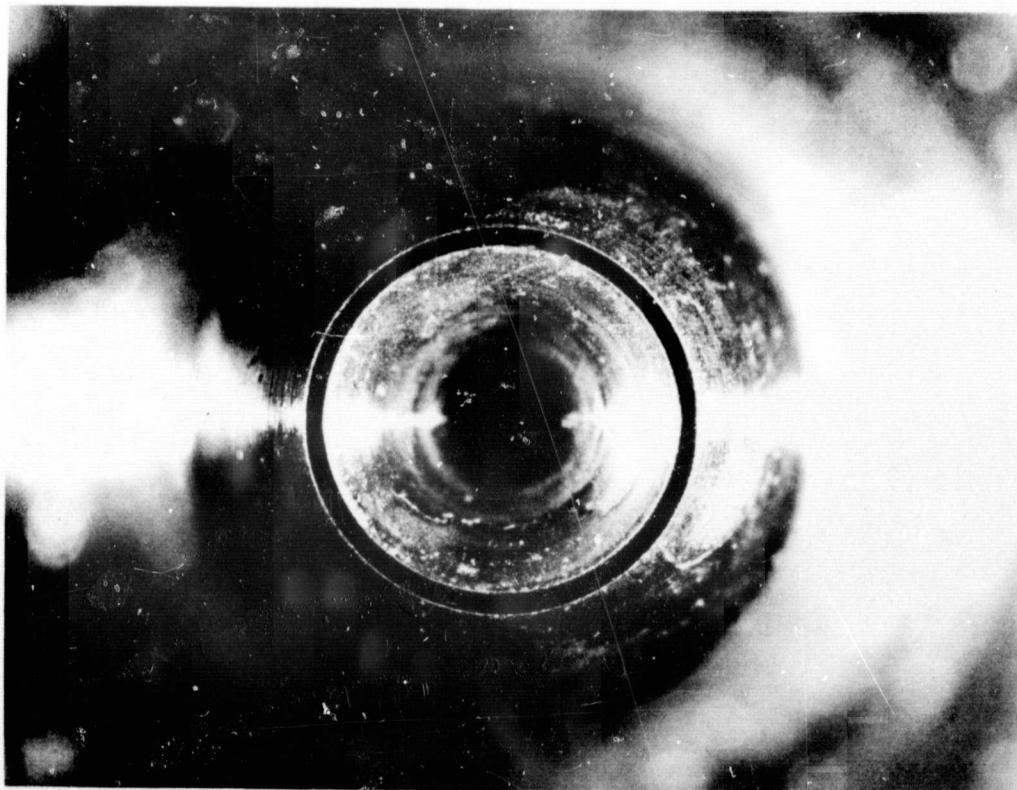
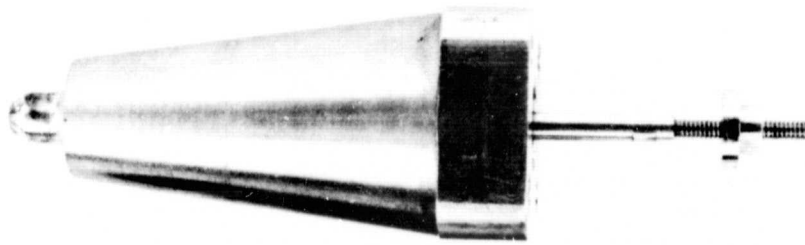


Figure 16. Photomicrograph of Annulus A06 (X 50 Magnification)
After Testing (Run 7002-01, -02)



006181

Figure 17. GSFC Annular Emitter

With thoriated tungsten, the main difficulty encountered was flaking and cracking of the material as attempts were made to produce edges less than 0.005 inch. Lapping operations, using a special lapping compound consisting of small diamond particles suspended in glycerin base, were successful in reducing the knife edge from 0.005 inch down to 0.003 inch. Although no attempts were made to reduce the edge to smaller dimensions, this technique appears promising for further reduction. A photomicrograph of the edge of a completed annulus constructed in this manner is shown in Figure 18.

Past work with needle emitters demonstrated the resistance to corrosion of Pt/Ir materials. Methods for fabricating annuli from platinum based materials were investigated and plating annulus emitter edges with platinum was considered. However, this approach was not pursued in view of the difficulties in maintaining the thin coating under the conditions of high voltage spraying. A successful technique was developed by constructing annuli with platinum/iridium edges of substantial thickness. This approach involved the brazing of a platinum (90 percent)/iridium (10 percent) washer 0.020 inch thick to a stainless steel cylinder using a NIORO (Ni-Au) braze material. The washer was brazed under pressure supplied by a threaded plug insert. The brazed unit was then made into an outer annulus sleeving, using machining techniques identical to those used for conventional stainless steel annuli. The edge of the outer sleeving was machined to a 0.002-inch edge while maintaining the integrity of the braze joint. Figure 19a shows the position of the brazed Pt/Ir washer on the stainless steel cylinder. The dotted line indicates the cut to produce the finished outer sleeving. Figure 19b shows the dimensions of the Pt/Ir at the emitter edge. A photomicrograph shows the details of the emitter edge (Figure 20). Note the differences in the conditions of the surfaces between the platinum/iridium (outer) and 20Cb3 stainless steel (inner) materials. If a smooth surface is preferred for spraying, the superiority of the Pt/Ir material over stainless steel or tungsten is apparent from the photomicrographs.

006092

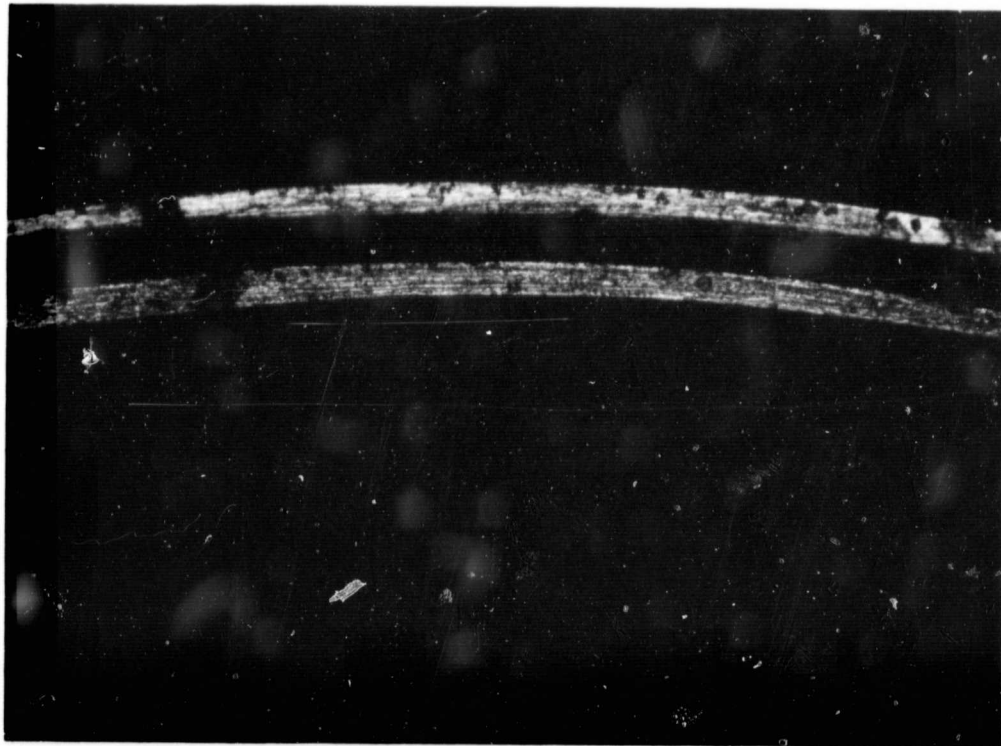


Figure 18. Photomicrograph Showing Details of Thoriated (2%) Tungsten Annulus (A07) Emitter Edge at 50X Magnification

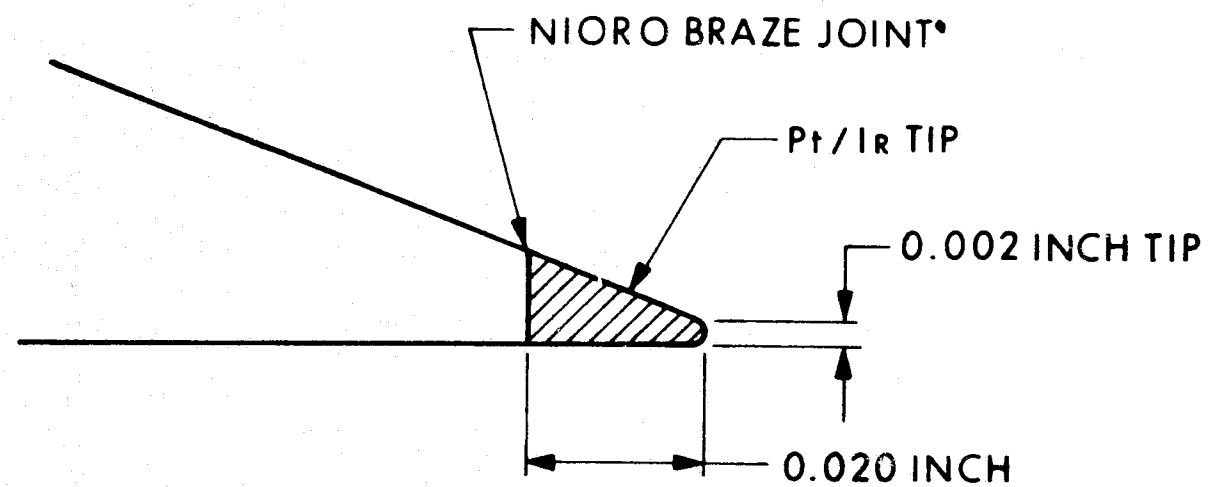
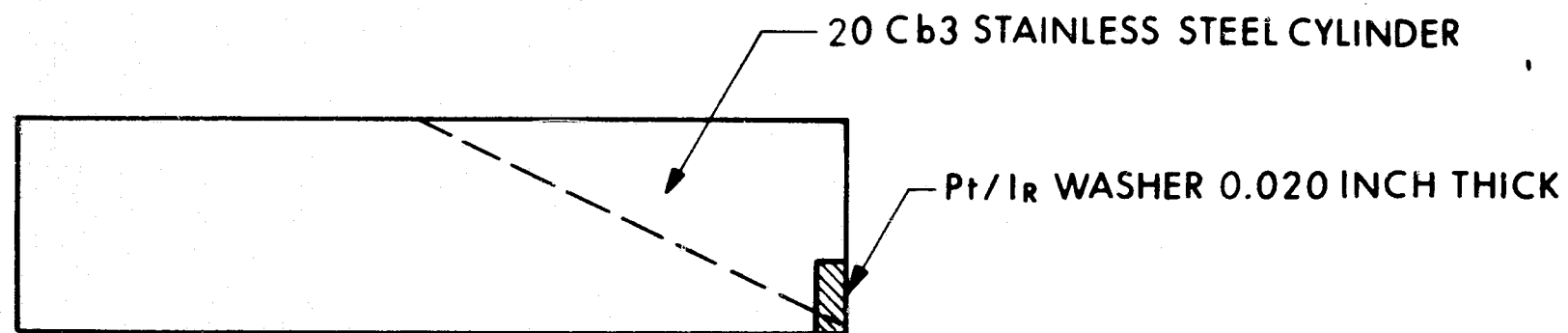


Figure 19. Technique of Fabricating Emitter with Pt/Ir Edge

006093

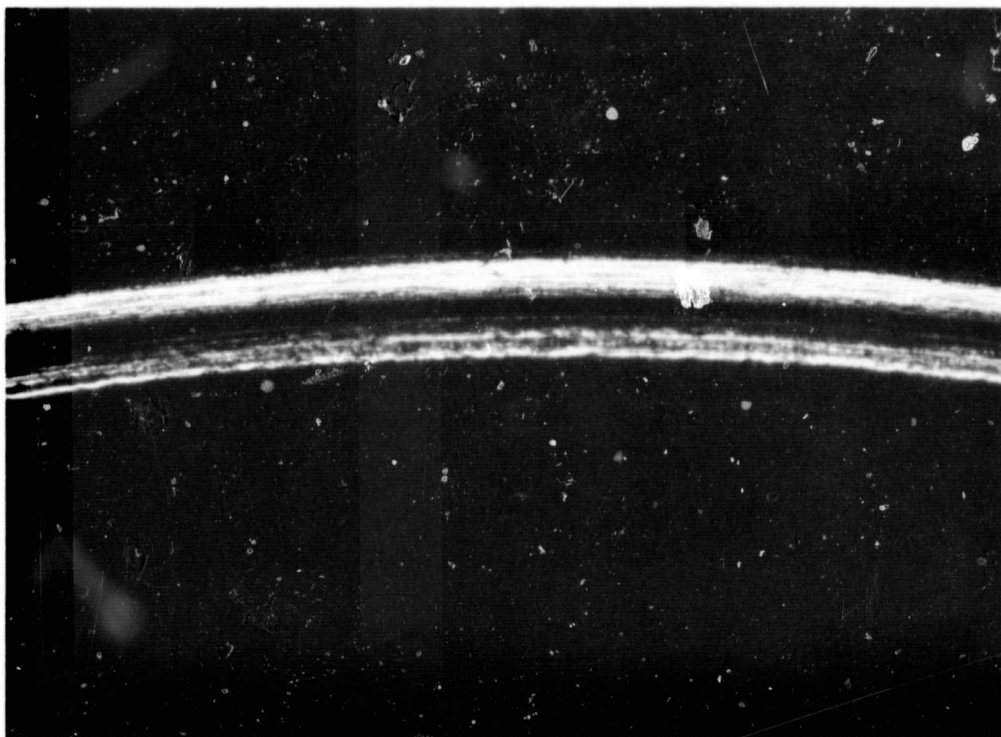


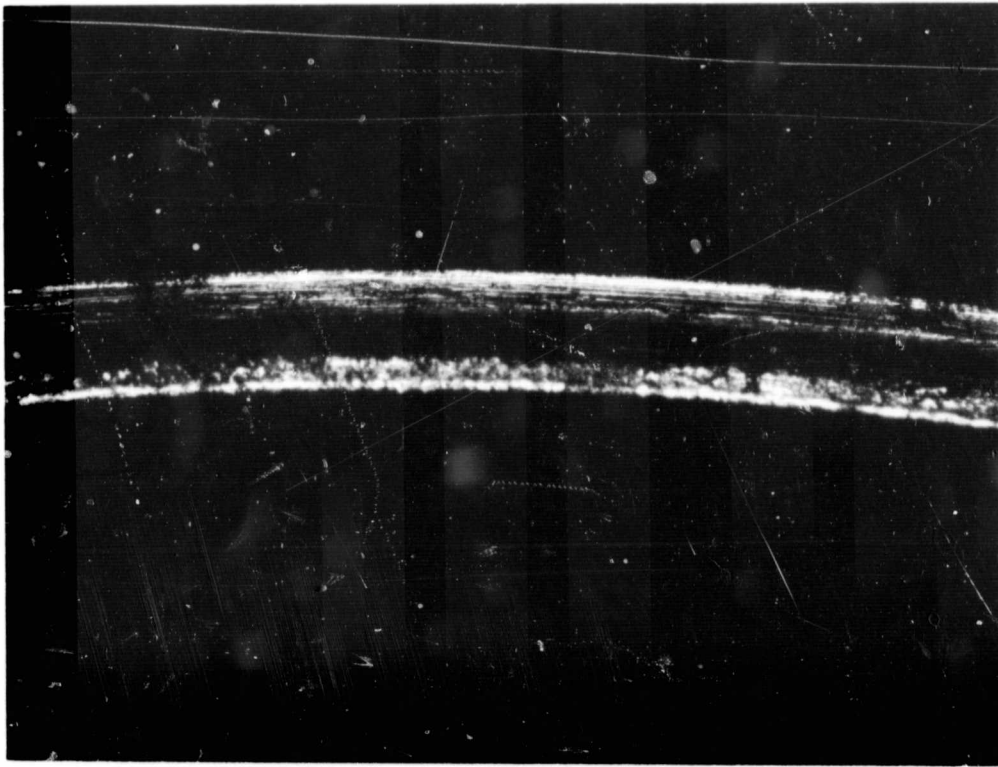
Figure 20. Photomicrograph Showing Details of Platinum (90%) Iridium (10%) and 20 CB3 S.S. Annulus (A08) Emitter Edges at X50 Magnification

A test was conducted with an annulus made with the Pt/Ir tipped outer sleeving and a 20Cb3 stainless steel inner sleeving for erosion comparison. Photomicrographs of the emitter surfaces at X50 magnification were taken after 50 hours of continuous operation and one is shown in Figure 21. Although it would have been desirable to operate the annulus longer, the photomicrographs clearly indicate that erosion has begun at the 20Cb3 stainless steel surface. The Pt/Ir surface appears affected by the spraying process, but to a lesser extent than the stainless steel. A longer duration run would be required to firmly establish the superior resistance of the Pt/Ir against erosion. However, the preliminary evidence strongly favors Pt/Ir as a future choice for annulus edges.

2.3.3 THRUSTER CONFIGURATION

Figure 22 shows an assembled thruster assembly used in recent tests. The outer plate seen in the figure is the guard shield typically operated between -500 to -1000 volts to prevent backstreaming electrons from reaching the annulus. Previously, the outer extractor fulfilled this function, however, it is not as effective since it must be operated at high negative potential to be an effective barrier against electron penetration. With the guard electrode added, the outer extractor bias can be made variable for use as a focusing or deflecting (segmented) electrode. Note the small spherical inner extractor in the center of the annulus in the figure. This particular inner extractor has a 0.200 inch diameter. In more recent tests 0.250 and 0.300 inch diameter inner extractors have been used.

Early tests performed on this program involving inner extractor geometries were aimed at eliminating inner extractor currents. More recent tests have added much to the understanding of inner extractor current origin (see Section 5). As a result, it has been determined that inner extractor currents do not depend critically on the geometrical configuration of extractors. The various kinds of inner extractor



006096

Figure 21. Photomicrograph (X50 Magnification) of Pt/Ir and 20CB3 Stainless Steel Emitter (A08) after 50 Hours of Continuous Operation (Run 7003-01)

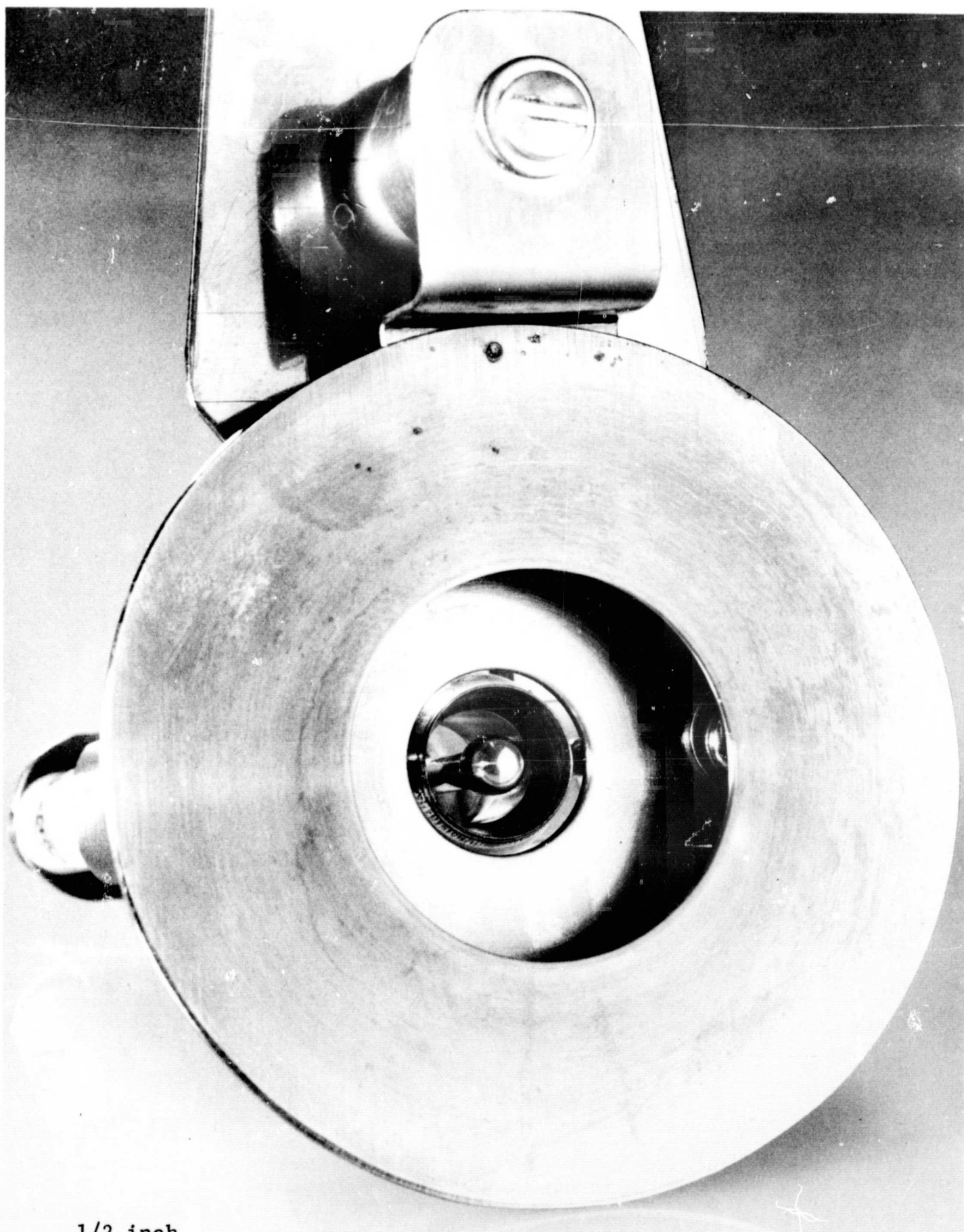


Figure 22. Annulus Colloid Thruster

geometries tested include flat discs, circular rings with conical bases, and spherical structures. Examples of the first two can be seen in Figure 23. The inclusion of an inner extractor in a thruster assembly has a pronounced effect on performance and beam focusing as evident from tests without an inner extractor. The geometry of the inner extractor in this instance may be important in determining the degree of focusing achievable as a function of inner extractor voltage.

2.3.3.1 Annulus Emitter Dimensions

Table 1, listing the geometrical and flow properties of the annuli tested, is included for reference purposes. The notations used are defined as follows: h is the annulus gap, ℓ the length of the gap, ℓ_s the length of the restrictive shelf, and N is the number of grooves in the shelf followed by groove width and depth dimensions. All dimensions are given in inches. The relative permeability is defined by

$$\text{Relative permeability} = P_A / P_N$$

where P_A is inversely proportional to the time for a given volume of gas to flow through a standard needle (0.004 inch i.d. and 1 cm long). P_N is the permeability of an annulus for an equal flow (volume) of gas.

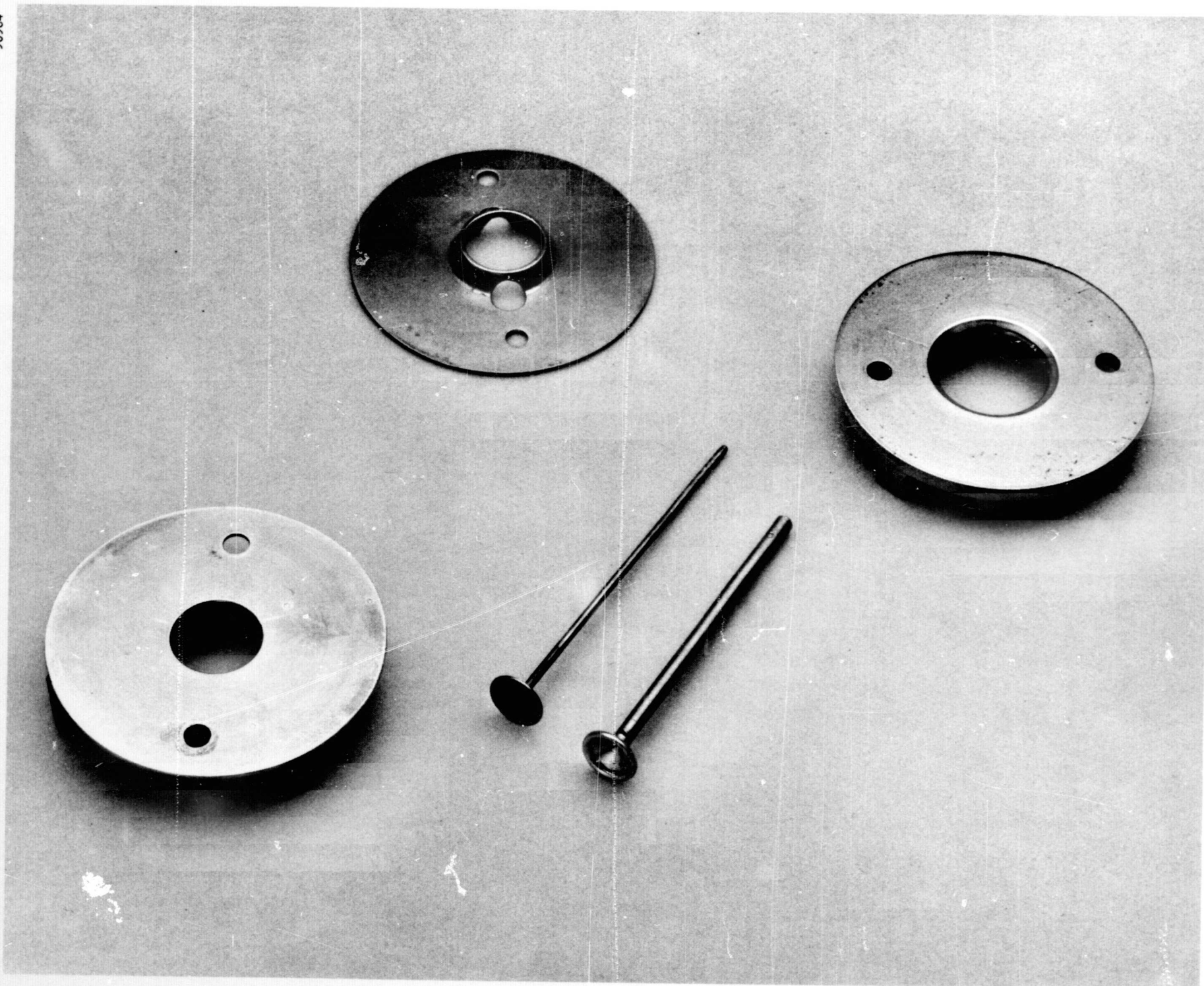


Figure 23. Inner and Outer Extractor Geometries

TABLE 1

GEOMETRICAL AND FLOW PROPERTIES OF THE ANNULI TESTED

Emitter Identification	Emitter Material	Critical Dimensions	Relative Permeability
A01	304 S.S.	h = 0.001 $\ell_s = 0.120$ N = 50 0.001 x 0.001	1.75
A02	20Cb3 S.S.	h = 0.001 $\ell = 0.030$ $\ell_s = 0.120$ N ^s = 8 0.006 x 0.00	4.2
A03	20Cb3 S.S.	h = 0.001 $\ell = 0.050$ no shelf	26
A04	20Cb3 S.S.	h = 0.001 $\ell = 0.100$ no shelf	289
A05	20Cb3 S.S.	h = 0.001 $\ell = 0.120$ $\ell_s = 0.120$ N ^s = 50 0.001 x 0.001	10.8
A06	20Cb3 S.S.	h = metal-to-metal fit $\ell = 0.020$	10
A07	2 percent thoriated tungsten	h = 0.003 $\rho = 0.100$ (with stuffing foil)	6
A08	Pt/Ir 20Cb3 S.S.	h = 0.001 $\ell = 0.120$ $\ell_s = 0.120$ N ^s = 30 0.001 x 0.001	0.3
A09	20Cb3 S.S.	h = metal-to-metal fit (~ 0.0005 inch) $\ell = 0.050$ no shelf	13
GSFC	Platinum plating on 20Cb3 S.S.	h = 0.002 $\ell_s =$ not applicable N = not applicable	

SECTION 3

PROPELLANT AND FLOW CONTROL TESTS

This section includes data on propellant properties and a discussion of the mass flow meter and controller test with an operating emitter.

3.1 PROPELLANT PROPERTIES

The usual propellant was a solution of NaI dissolved in glycerol. The significant properties of a colloid propellant are the viscosity and conductivity. Figure 24 shows the viscosity as a function of temperature for pure glycerol obtained from a handbook (Ref. 8) and of a 20g NaI/100 ml glycerol solution. The data for the 20g NaI/100 ml glycerol solution were obtained experimentally using a temperature controlled viscometer.

Several batches of NaI/glycerol were mixed for use as propellant for emitter operational tests and are listed in Table 2. Four were mixed using the same proportions and resulted in a slightly different conductivities. The last batch was made using a larger amount of NaI and had the highest conductivity. The latter solution was used in an attempt to increase the generated mean specific charge by increasing the solution charge concentration. The results indicate better operation, but because of insufficient data this conclusion is only qualitative.

A chamber was designed and constructed for use in measurements of the conductivity of propellant fluids as a function of temperature. The chamber has connections for the insertion of thermocouples and vacuum/gas ports. A conductivity cell is mounted through the top of the chamber and is externally connected to a Beckman Instrument RA-5 conductivity meter. The instrument is calibrated to read the conductivity directly

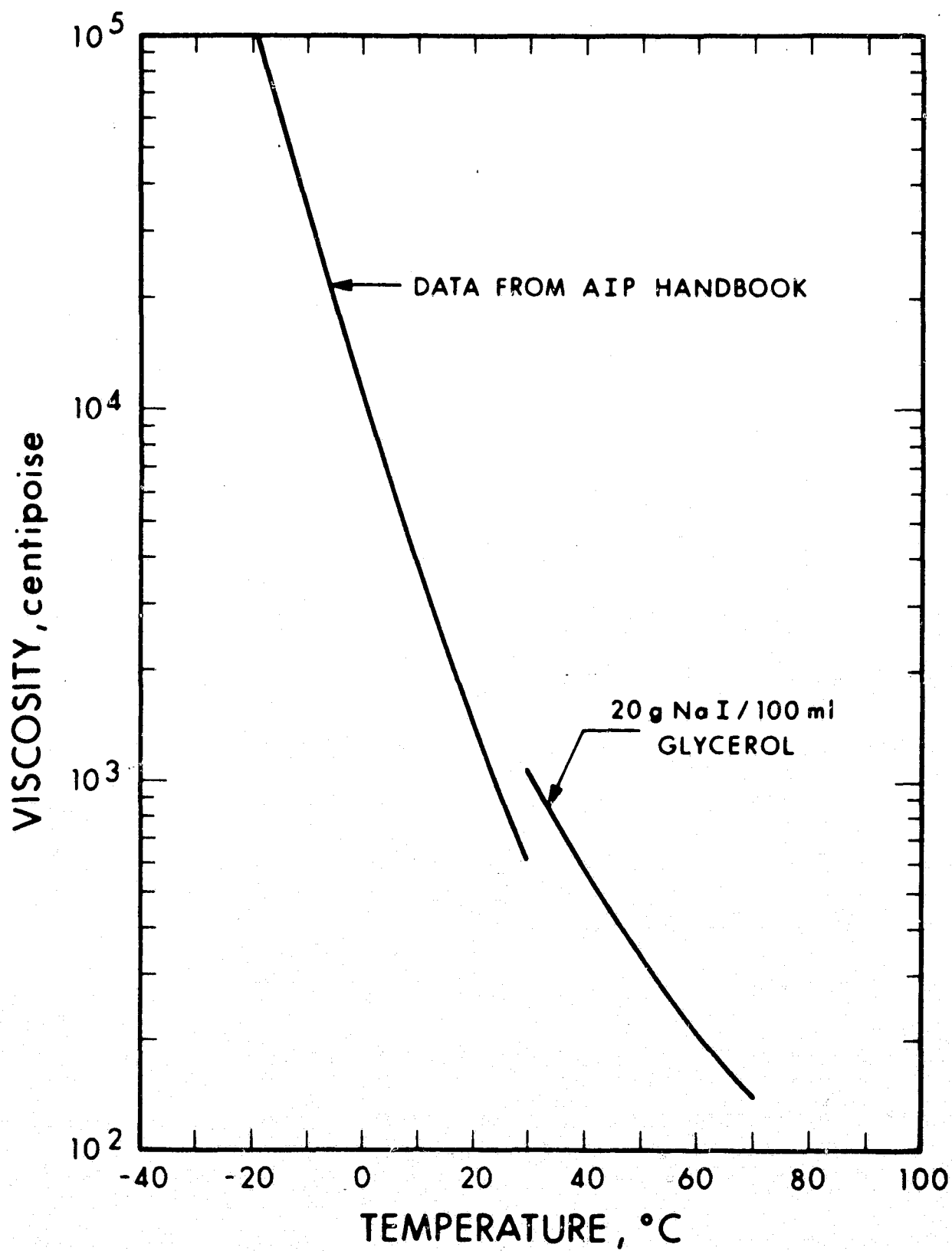


Figure 24. Viscosity of Glycerol

TABLE 2

PROPELLANT FLUID IDENTIFICATION

Batch No.	Dopant/Fluid	Conductivity $10^{-4} \Omega^{-1} \text{cm}^{-1}$
F01	20 gms NaI/100 ml glycerol	2.13
F02	20 gms NaI/100 ml glycerol	2.7
F03	20 gms NaI/100 ml glycerol	---
F04	20 gms NaI/100 ml glycerol	2
F05	30 gms NaI/100 ml glycerol	3

in micro-mhos/cm. The entire chamber may be kept at a constant temperature (or varied) by heater wire brazed to the chamber body.

A solution of 20 gm NaI/100 ml glycerol was mixed, filtered and out-gassed. The conductivity versus temperature of the fluid was measured using the chamber described above. The maximum temperature was limited to 32°C because full scale conductivity was obtained at this temperature using the available conductivity cell. The results of these measurements are presented in Figure 25. Note the abrupt change in slope which occurs near the quoted melting point of glycerol (17.9°C).

3.2 FLOWRATE CONTROL TEST WITH AN ANNULUS

An annulus thruster was successfully operated with a mass flowmeter and a controlled flow restrictor (emitter A03, Run 7001-01). The flowmeter and controller were developed on an EOS funded program, and were described in Subsection 2.2.2.5.

The flowmeter and controller were operated in a closed-loop condition. To determine if the feedback loop was operating properly, the following check was performed: (a) a signal was dialed into the restrictor circuitry to maintain a constant flowrate at some temperature; (b) the

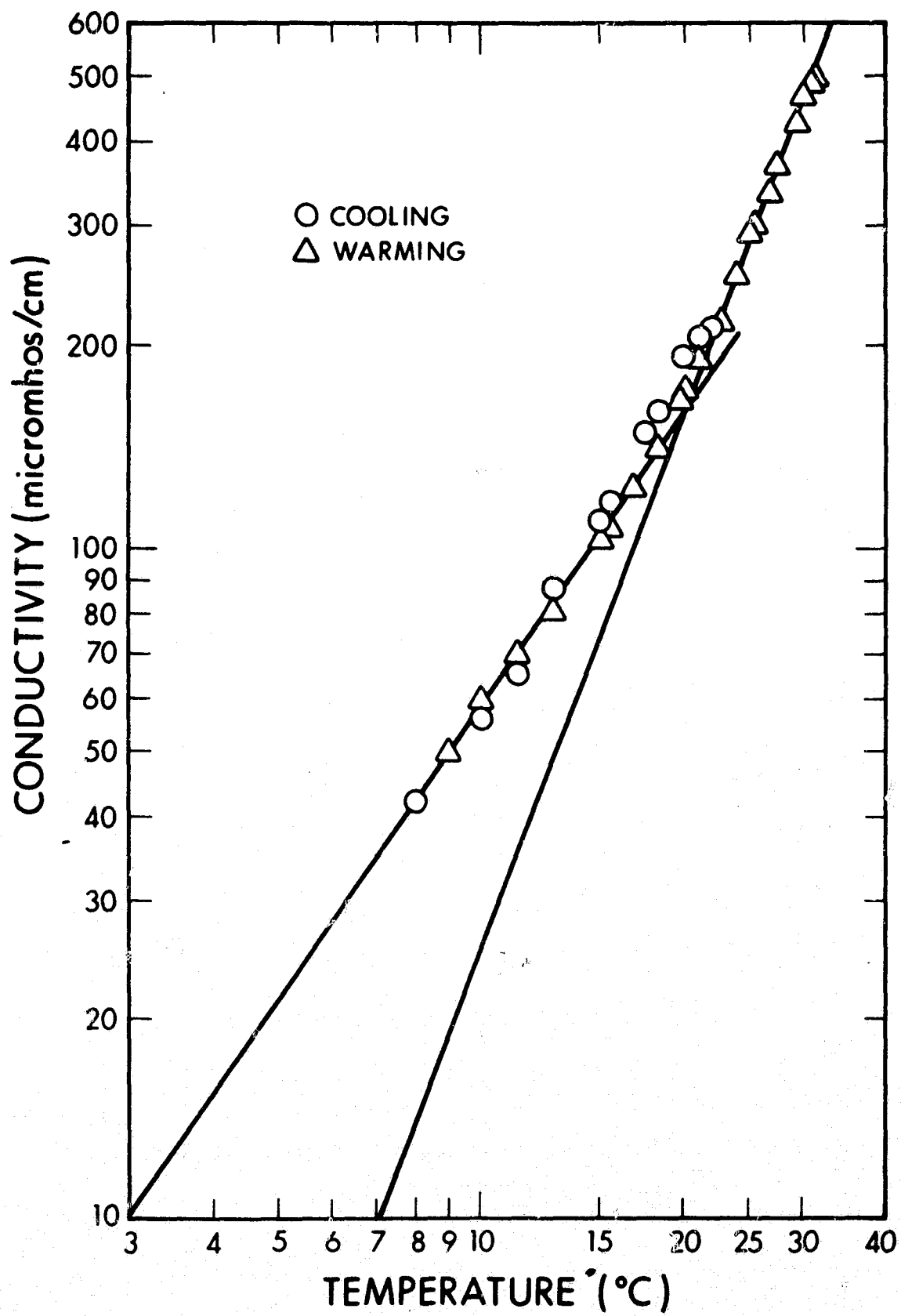


Figure 25. Conductivity versus Temperature for 20 gm NaI/100 ml Glycerol Mixture

flowrate was abruptly changed by increasing the feed system pressure; and (c) the controller responded by decreasing the restrictor heater power and the flowrate to its preset level.

Most tests consisted of dialing in a sequence of mass rates, noting the response of the annulus current, and determining the mass flowrate versus current characteristics at several voltages. The annulus current responded instantaneously to variations in restrictor power input, and stabilization was achieved in a matter of minutes.

The results of these tests are plotted in Figure 26 where the annulus current is shown as a function of the calibrated mass flowmeter readings at two different emitter voltages. For this test the mass flowmeter was calibrated so that 1 μ A reading of the mass flowmeter is equivalent to 1 μ g/sec. The crosses denote experimental data points and the solid lines were fitted to the data using the analytical techniques described in Section 4. The analytical extrapolation shows the flowmeter zero had shifted. The flowmeter was adjusted to read zero before filling the metering lines, but it was not adjusted with propellant fluid in the metering lines. This was probably the reason for the zero shift indicated in Figure 26.

The experimental arrangement precluded the taking of TOF data for direct mass flowrate comparison. An effect was observed during this test which requires further investigation. Emitter response to variations in the flow controller temperatures shows some pressure dependence. At low feed system pressures, response is extremely slow. The pressure ranges where response is slow or instantaneous have not been sufficiently identified to make predictions. This pressure dependence on response may be inherently connected to the total impedance of the thruster system.

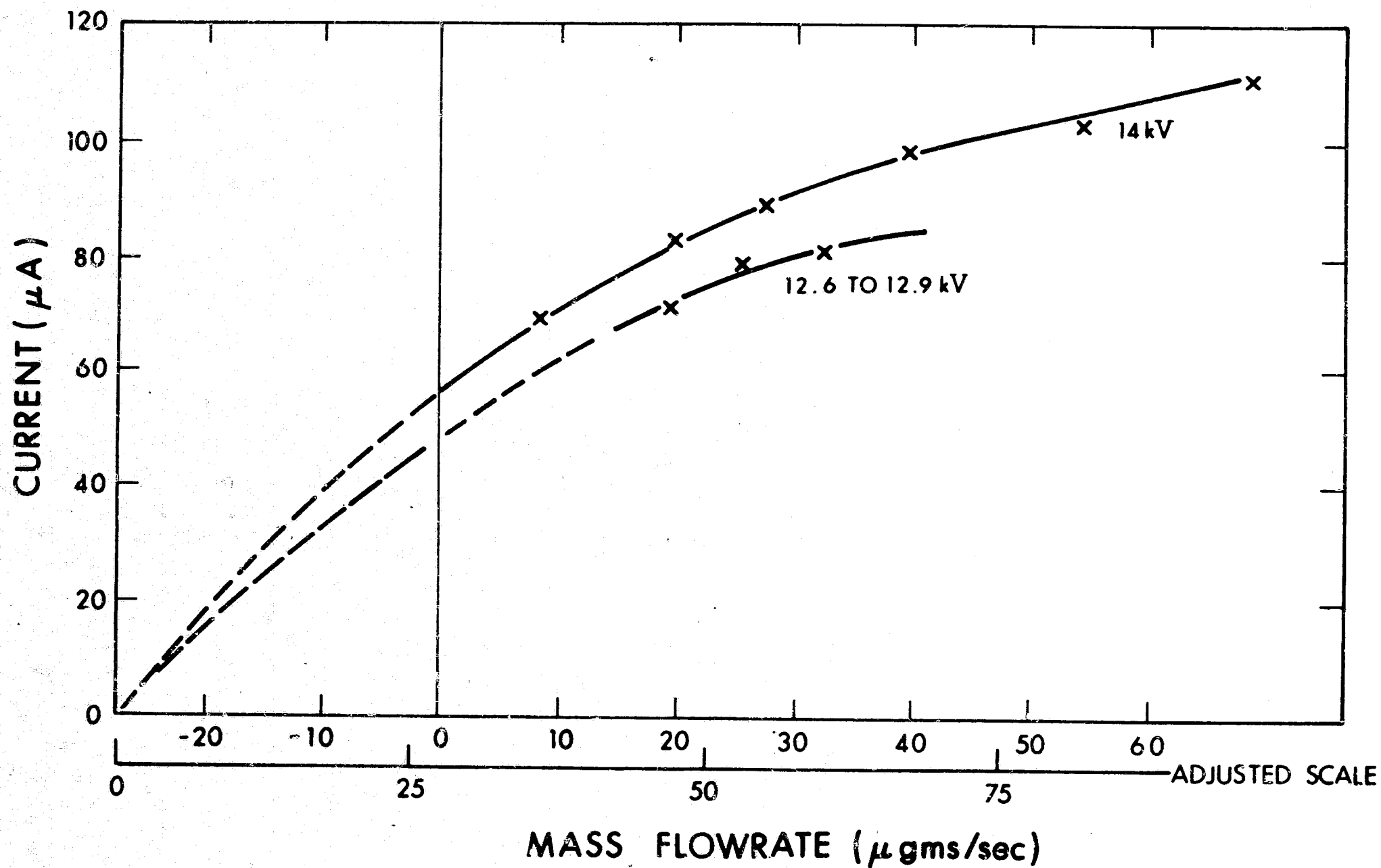


Figure 26. Annulus Emitter Current versus Mass Flowmeter Reading

SECTION 4

ANALYTICAL STUDIES

Analytical models which mathematically describe the operation of a colloid emitter have been the goal of many past studies. Some of these studies started from the properties of propellant liquids and traced the dynamics of the liquid interface when an intense electric field is applied (Refs. 9, 10, and 11). The equations resulting from the studies were then compared with experimental results to verify applicability with some success achieved. Parametric plots have been used to display performance data (Ref. 12) as an aid to understanding operation. No extensive change in understanding has resulted from either of these approaches. Difficulties stem from a lack of the precise data required to determine the dominant charge particle generating process when competing processes are involved, and from the lack of data over a wide range of control variables.

Emitter tests made at the beginning of the present program revealed an unexplored region of emitter operation at low mass flowrates in which the beam current and the thrust are linear with the mass flowrate. Exploration of this region was considered the key to understanding colloid operation and provides the basis for an analytical model. Operation in this emission limited current region was attained by restricting the mass flowrate to levels below that ordinarily obtained by capillary force flow. The results obtained from a systematic exploration of this and other mass flowrate regions were compared with a parallel analytical study.

The understanding derived from the analytical results provides the basis for the systematic study of colloid emission which is required for the design and fabrication of a thruster system having predictable

operational parameters. In addition the wide operating range previously envisioned for colloid thrusters (Ref. 13) may now be attainable using the analytical and experimental techniques developed on this program.

In this section, the derivation of the analytical equations are described with the emission limited low mass flowrate data as one limit and space charge limited formulas as the other limit. A mathematical function is formulated to bridge the gap between these two extreme conditions. The equations are then compared with the data and some further implications are discussed. Parametric plots are shown to illustrate the newly derived performance indices and to show the functional dependence upon the control variables. Finally an emitter having specified performance indices is described which would be capable of satisfying the performance goals of the follow-on program. Performance plots characterizing this thruster are shown which illustrate the wide operational range that could be achieved together with the tradeoffs required to span this range.

4.1 BACKGROUND DATA

Experimental data at low mass flowrates indicate that the performance of a colloid emitter is significantly different from that at high mass flowrates where most past data were obtained. This performance is characterized by a linear dependence of the emitter current with the mass flowrate at constant voltage. In this low mass flowrate region, other performance characteristics of significance included low beam divergence and little or no glow observed in the emitter region. Operation in the linear region resulted in good performance characteristics and is the region in which a thruster can be operated using a simple feedback control system.

Operation in the linear region is illustrated in the data shown in Figures 27 and 28 which were obtained from Runs 6909-01 and 6909-02. The current (I) versus mass flowrate (\dot{m}) curves imply that

$$I = b(V)\dot{m}, \quad (15)$$

where b is a function of the voltage (V). Figure 28 also shows the linearity of the thrust (T) with \dot{m} and a nearly constant specific impulse (I_{sp}) over the measured range. A constant, independent of V, is determined from a plot of the thrust versus I for data from run 6909-02. This plot shown in Figure 29 for a wide range of voltages illustrates the linearity. Thus we can characterize the current per unit thrust by

$$\frac{I}{T} = k, \quad (16)$$

where k is a constant in the linear region, but can change above this region. A mathematical form for k is obtained from the equations governing a colloid thruster which emits particles with a distribution of specific charge (q/m). The analysis is aimed at determining a set of analytical equations which show the dependence of thruster performance upon independent variables. The independent variables are \dot{m} , V, and emitter temperature and are termed control variables. Thruster performance is measured in terms of operational parameters which are emitter current, thrust, specific impulse, specific charge, and specific charge efficiency.

4.2 THRUSTER EQUATIONS

From the analysis of a colloid thruster the mean specific charge $\langle q/m \rangle$ is defined as

$$\left\langle \frac{q}{m} \right\rangle \equiv \langle C \rangle = \frac{I}{\dot{m}}. \quad (17)$$

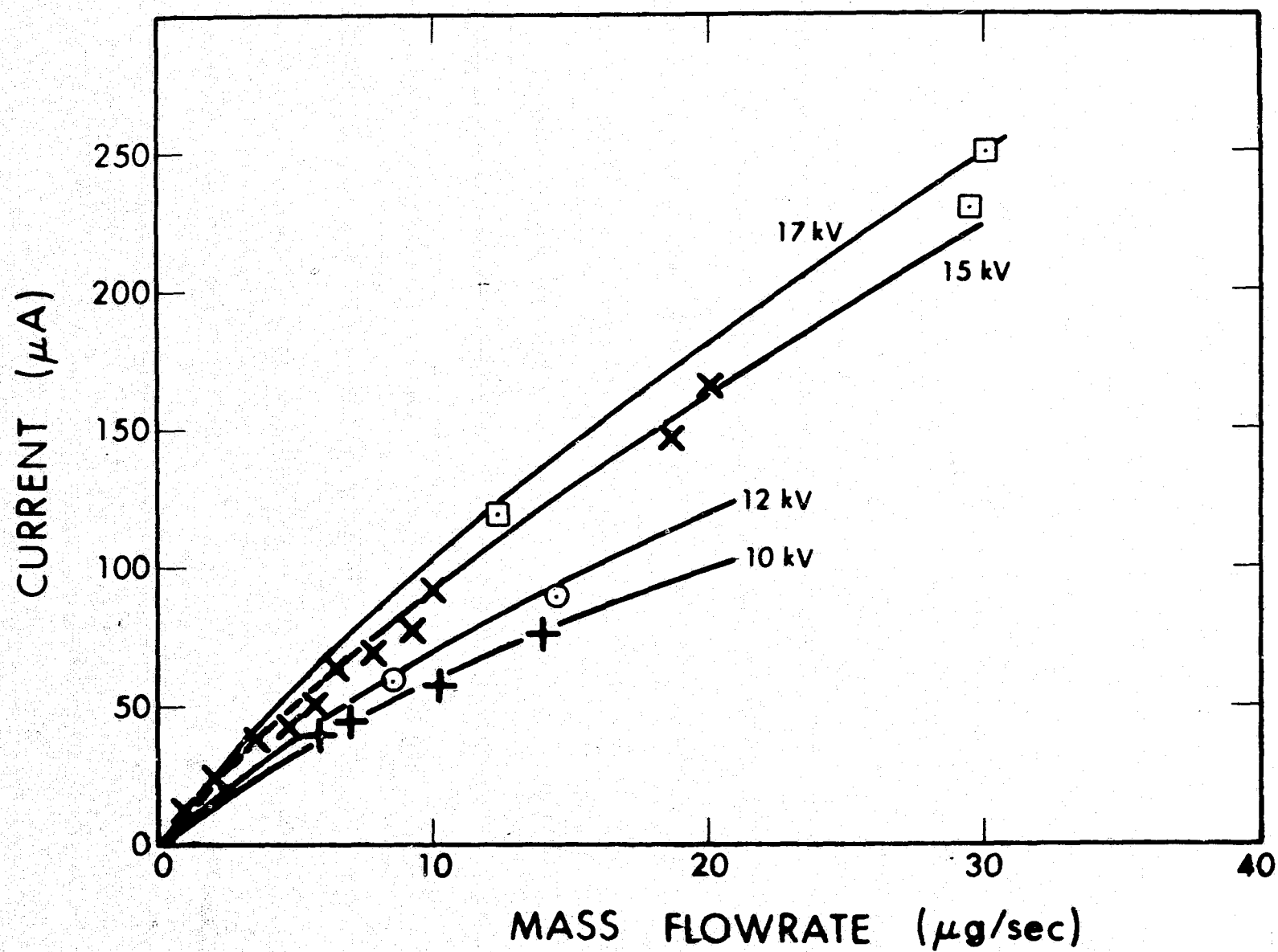


Figure 27. I versus \dot{m} for Annulus A01 (Run 6909-02)

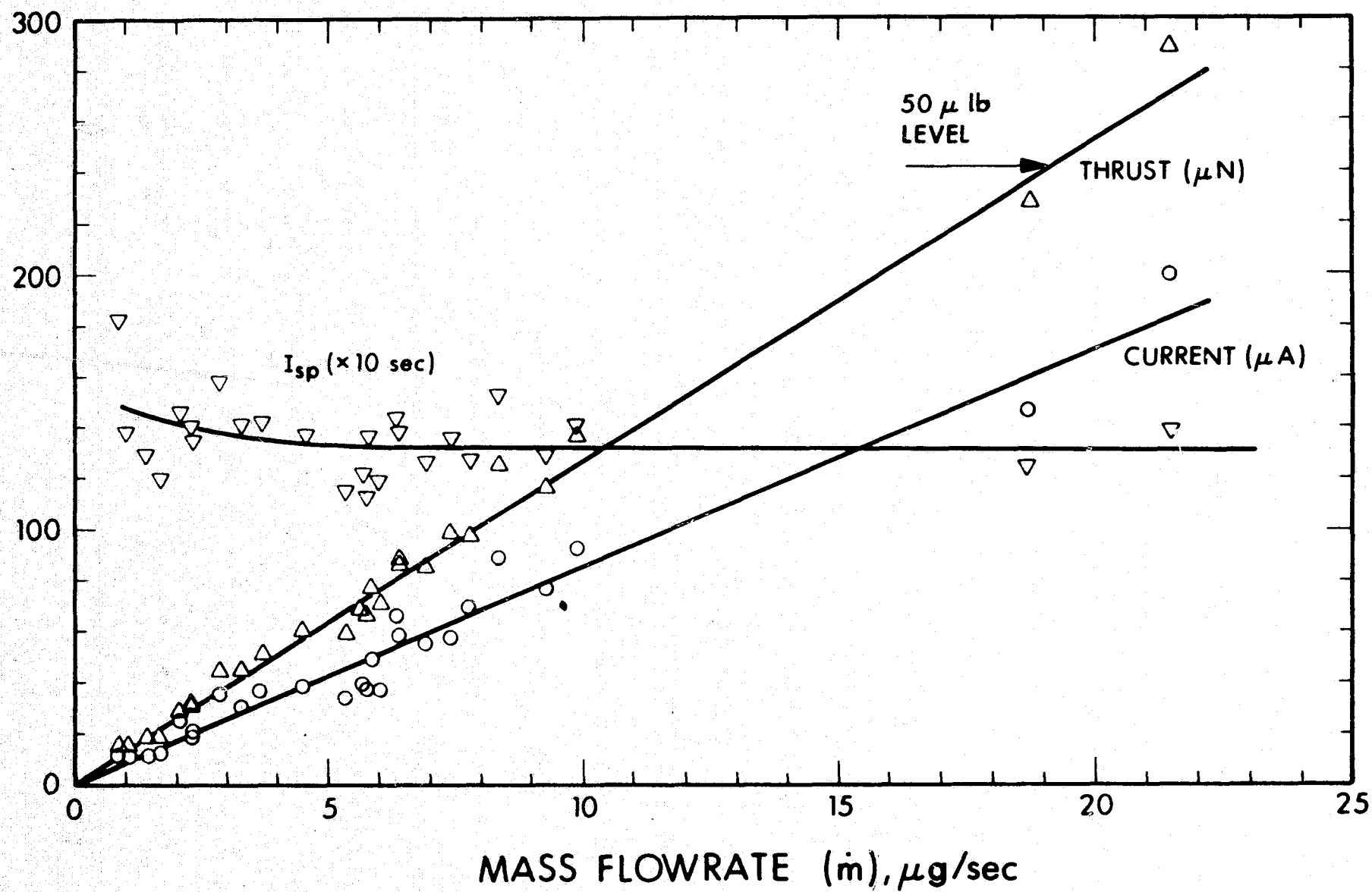


Figure 28. Variation of Thrust, Current, and Specific Impulse for Annulus A01 (Run 6909-01 at 15 kV)

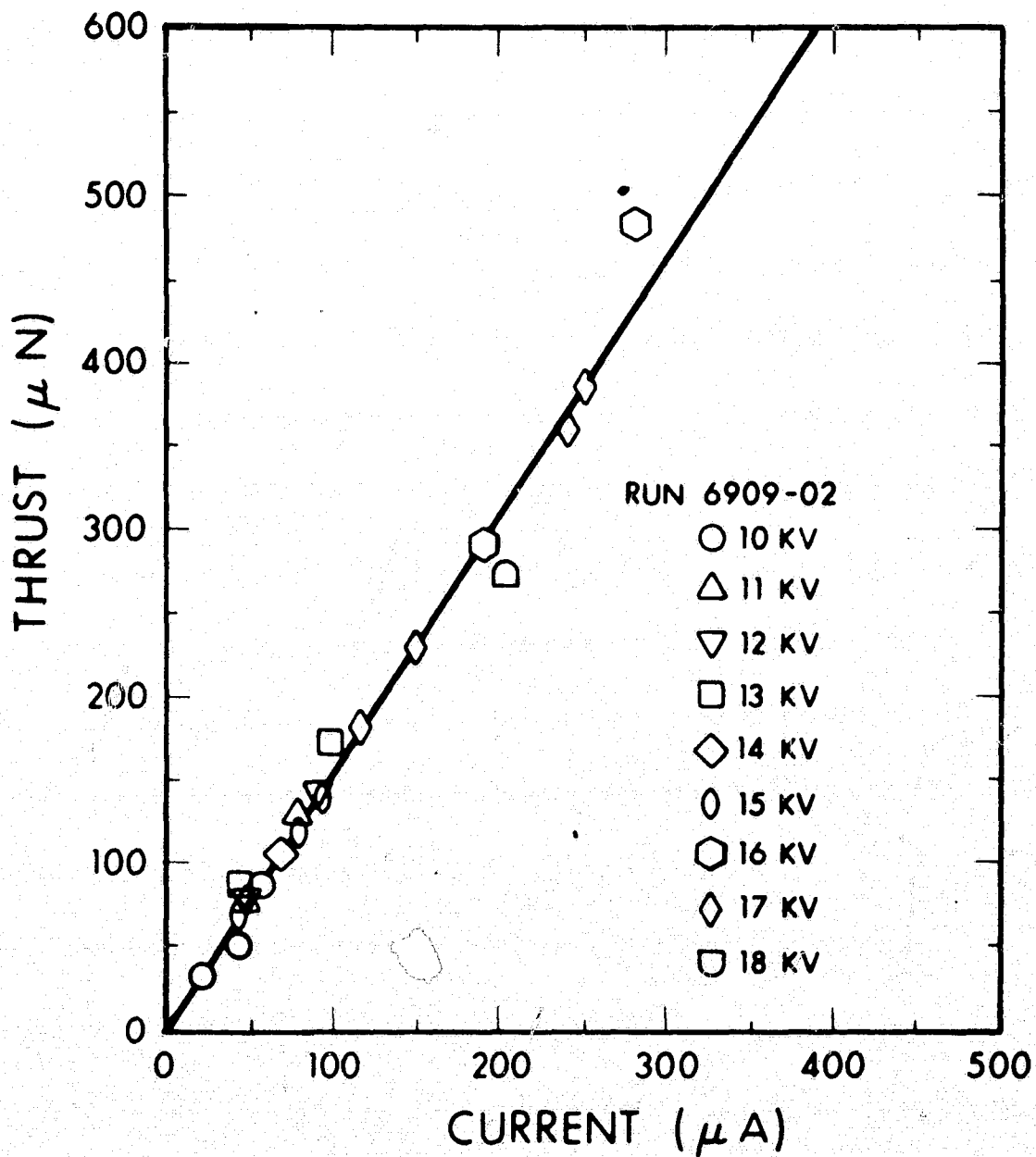


Figure 29. Thrust versus Current (Run 6909-02)

Note that $\langle \frac{q}{m} \rangle$ and $\langle C \rangle$ has the same form as $b(V)$ in Eq. 17. The thrust is given by

$$T = \dot{m} \langle v \rangle, \quad (18)$$

where $\langle v \rangle$ is the mean velocity in the emitted particle beam. From energy considerations ($qV = \frac{1}{2} mv^2$) this velocity is

$$v = \langle C^{1/2} \rangle (2V)^{1/2}, \quad (19)$$

where $\langle C^{1/2} \rangle$ is the mean root specific charge. The specific charge distribution efficiency (η) is given by

$$\eta = \frac{\langle C^{1/2} \rangle^2}{\langle C \rangle} \quad (20)$$

where $\langle C^{1/2} \rangle^2$ is the square mean root specific charge which characterizes the particle beam. Using Eqs. 17 through 20, Eq. 16 can be expressed as

$$\frac{I}{T} = \frac{\langle C \rangle^{1/2}}{(2\eta)^{1/2} V^{1/2}} = k, \quad (21)$$

where the term k can be defined as

$$k \equiv \frac{k_o}{(2\eta)^{1/2}} f(X), \quad (22)$$

where k_o is a constant with dimensions of $(A \text{ sec/kgV})^{1/2}$ that characterizes both the propellant properties and the emitter geometry and $f(X)$ is a function of $\langle C \rangle$ and V . In the linear region $\langle C \rangle$ is proportional to V so that $f(X)$ is unity. Thus from Eqs. 21 and 22 we can write

$$\langle C \rangle = k_o^2 f^2(X)V, \quad (23)$$

and from Eq. 17;

$$I = k_o^2 f^2(X)V\dot{m}. \quad (24)$$

To determine the functional dependence of $f(X)$ we consider the region at very large \dot{m} or large I where the current is space charge limited. This region is characterized by the Child-Langmuir equation for the current density (j) given by

$$j = pV^{3/2} \quad (25)$$

where p is the space charge perveance. Since the emission area (a) is not well defined and the specific charge varies we define a new term (P) called the specific perveance by

$$P = \frac{pa}{\langle C \rangle^{1/2}} \quad (26)$$

where P has the dimensions of $(A \text{ kg/sec } V^3)^{1/2}$. Thus Eq. 25 can be written as

$$I_s = \langle C \rangle^{1/2} PV^{3/2} \quad (27)$$

where I_s is the space charge limited current given by ja . The current shown in more general form in Eq. 24 should reduce to

$$I_l = k_o^2 V \dot{m} \quad (28)$$

in the linear region and to Eq. 27 in the space charge limited region.

The following function was found to smoothly bridge the gap between the two limiting cases and reduces to Eqs. 27 and 28 at the limits:

$$f(X) = X^{-1} (1 - e^{-X}) , \quad (29)$$

if

$$X = \frac{k_o \dot{m}}{P V} , \quad (30)$$

where k_o and P were defined previously (Eq. 22 and 26) and are of importance as thruster performance indices. The current and other operational parameters such as $\langle C \rangle$, thrust and specific impulse can be determined analytically using these two indices and the control variables \dot{m} and V in the expressions for $f(X)$ and X . The regions described as linear and space charge limited are not sharply defined by $f(X)$ and X but are so delineated as to convert Eq. 24 to the limiting cases given by Eqs. 27 and 28.

Past studies at our laboratory and elsewhere (Ref. 12) show that the specific charge decreases with increasing \dot{m} , particularly in the high \dot{m} regions previously explored for capillary needles. From this consideration, the current in the space charge limited region as given in Eq. 27, should slowly decrease with increasing \dot{m} . Since most past data show very little change of I with \dot{m} the data probably fell into the transition region between the two limiting cases discussed above. Thus, the current is known to be linearly increasing at low \dot{m} , level off to a maximum at intermediate \dot{m} and fall slowly at high \dot{m} . The function $f(X)$ shows this characteristic shape.

The operational parameter equations will be respecified in a form incorporating Eqs. 29 and 30 so that \dot{m} is implicit in the functions X and $f(X)$. Equation 24 can be rewritten as

$$I = k_o X f^2(X) PV^2, \quad (24A)$$

where only the term $X f^2(X) \equiv g(X)$ is a function of \dot{m} . At constant V , I versus \dot{m} can be parametrically displayed as $g(X)$ versus X . The rest of the operational parameters are given in a form where only the dimensionless terms contain \dot{m} :

$$T = (2\eta)^{1/2} X f(X) PV^2 \quad (31)$$

$$I_{sp} = (2\eta)^{1/2} \frac{k_o f(X) V}{g}, \quad (32)$$

where g is the acceleration due to gravity on the earth. Equations 23, 24A, 31 and 32 are written in parametric form with k_o , P , and η constant so that $X \propto \dot{m}$:

$$\langle C \rangle \propto f^2(x), \quad (33)$$

$$I \propto g(x) \equiv x f^2(X), \quad (34)$$

$$T \propto X f(x), \quad (35)$$

$$I_{sp} \propto f(x). \quad (36)$$

These relationships are displayed in Figure 30. Note that $\langle C \rangle$ decreases with \dot{m} (or X) and that I_{sp} decreases less rapidly. The current increases, reaches a maximum, then decreases, while the thrust continuously increases. In the linear region the I_{sp} changes by only 10 percent and I and T are nearly linear with \dot{m} .

To characterize the operation of a thruster only one of these operational parameters is required since the rest are related as shown in Figure 30. The current curve was chosen to describe the different regions which are defined with respect to the current curve as:

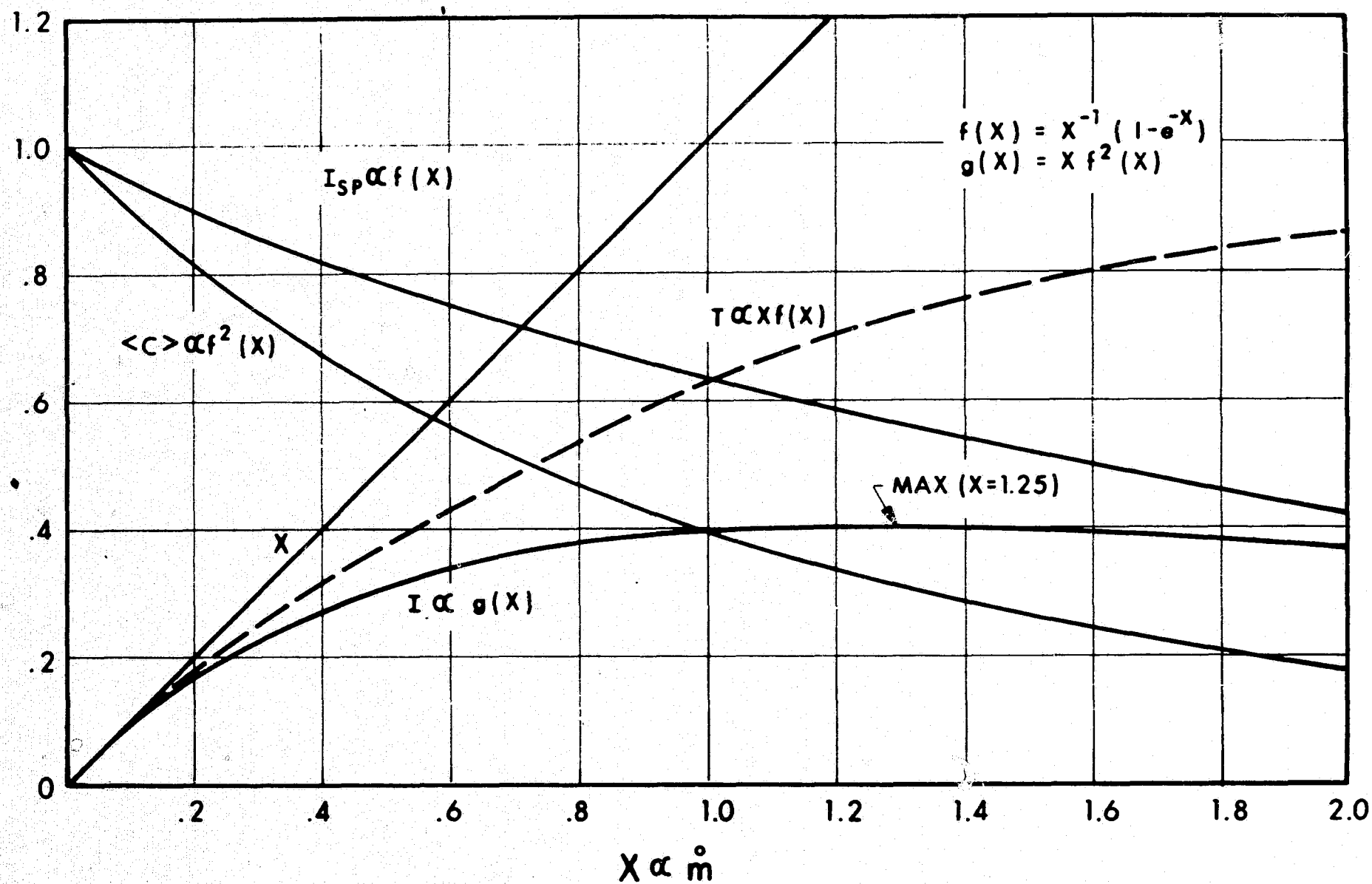


Figure 30. Parametric Variation with \dot{m} at $V = \text{Constant}$

$$\text{Linear (within 20 percent)} \quad X \leq 0.2 \quad f(X) \approx 1 \quad (37)$$

$$\text{Transition} \quad 0.2 < X < 2.3 \quad (38)$$

$$\text{Space charge limited (within 10 percent)} \quad X \geq 2.3 \quad f(X) \approx \frac{1}{X} = \frac{PV}{k_o \dot{m}} \quad (39)$$

$$\text{Position of Maximum} \quad X = 1.25 \quad (40)$$

4.3 COMPARISON WITH EXPERIMENT

Data were taken which verify the features displayed in Figure 30. The general curve shapes are also confirmed by the data of other investigators (Ref. 12). Data were expressly taken to examine the transition region where the current does not vary greatly with mass flow. Figure 31 displays this region for three voltages. The curves drawn through the experimental data points were obtained from the analytical equations (Eq. 24A) with the value of k_o obtained from reduced TOF data using Eqs. 21 and 22. P was determined from the current maximum at one voltage using $X = 1.25$ from Eqs. 16 and 26 to obtain

$$P = \frac{k_o \dot{m}}{1.25V} \quad (\text{at the maximum}) \quad (41)$$

The efficiency (η) was found to change very little for each of the data points so that $(2\eta)^{1/2}$ was considered constant over a run and an average value was used. Figures 32 and 33 show other operational parameter data points and analytical curves for the same run. The agreement between the data points from several runs and the analytical curves was sufficiently good to have confidence in the ability to predict thruster operation.

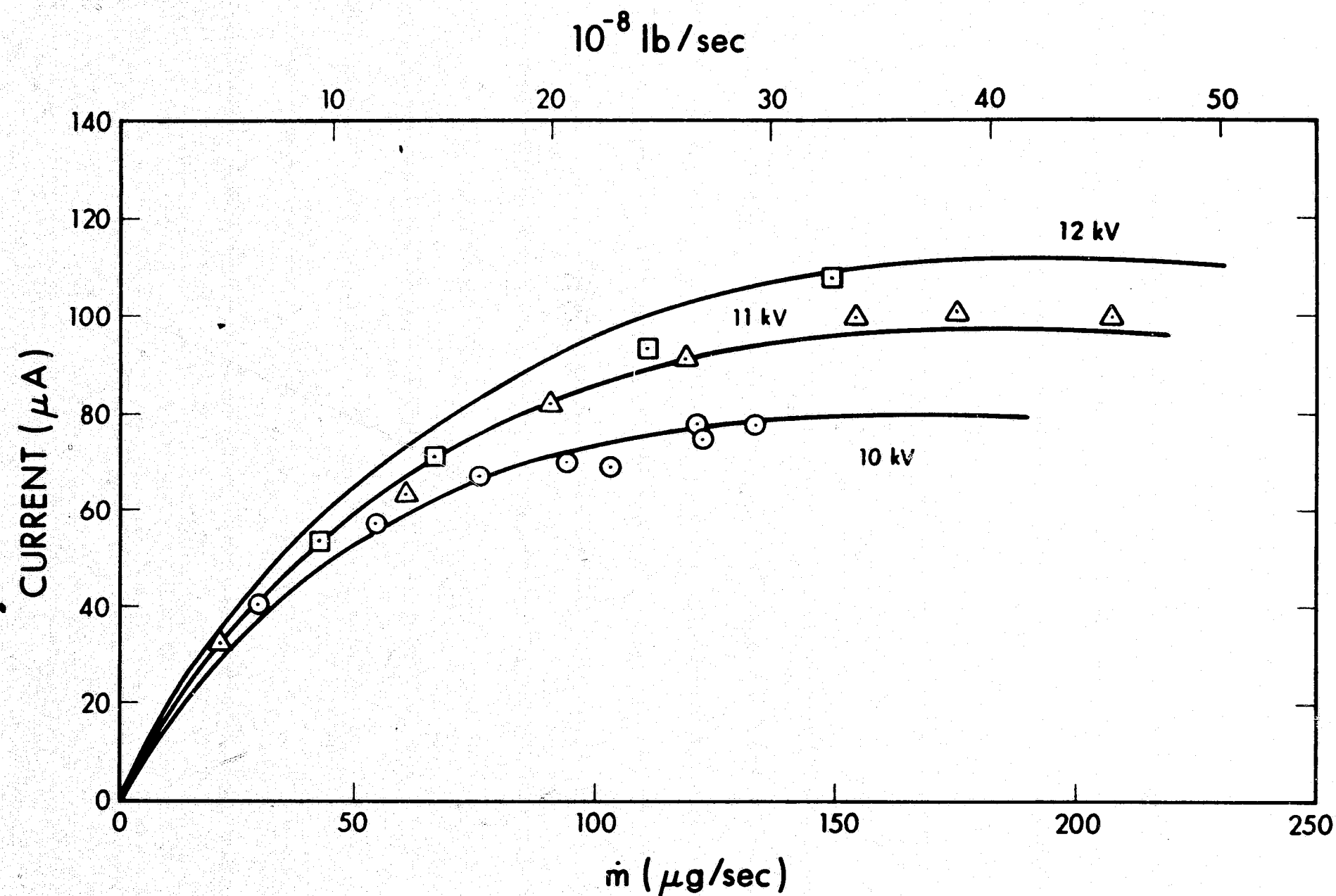


Figure 31. I versus \dot{m} for A02, Run 6910-01

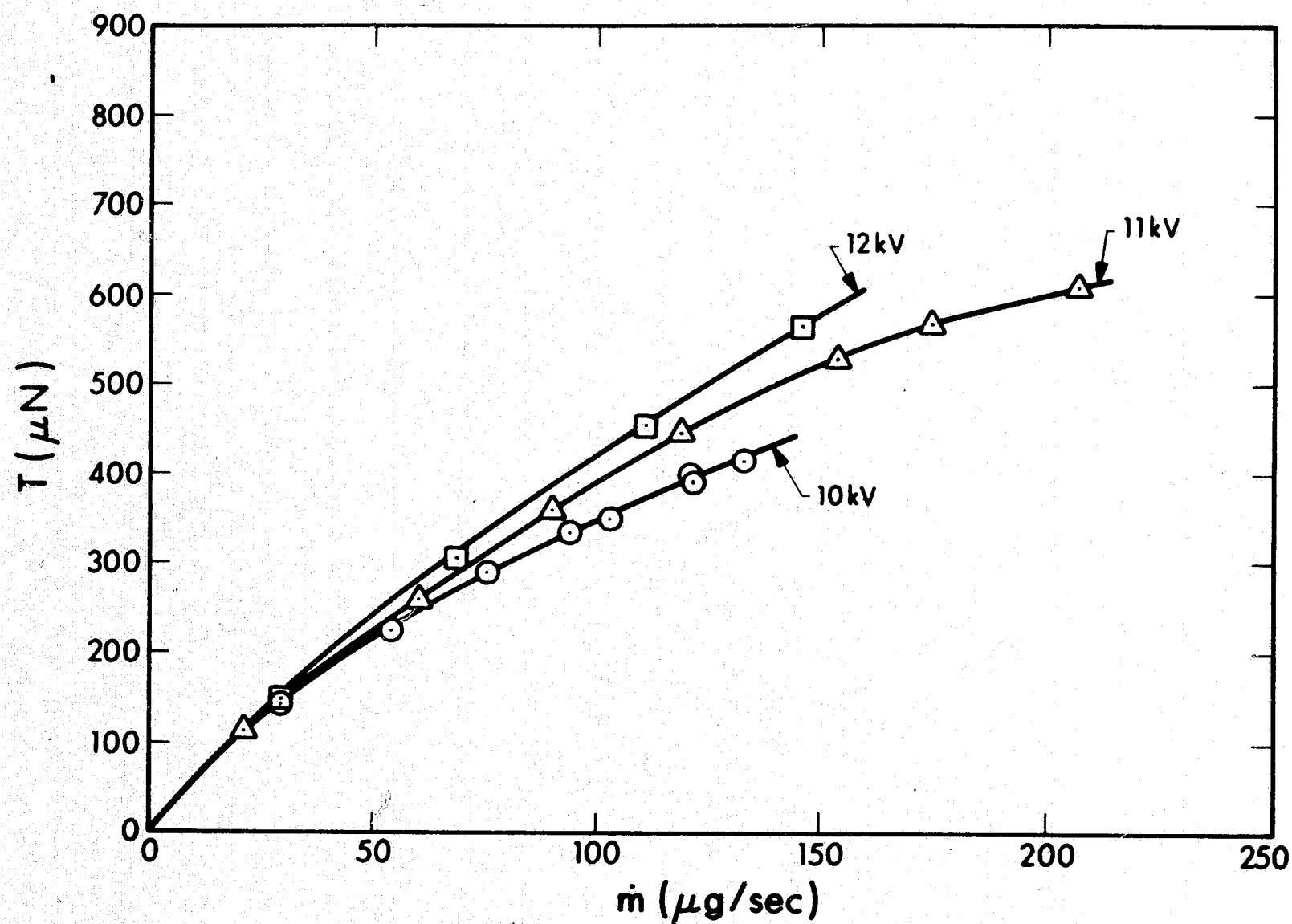


Figure 32. T versus \dot{m} for A02, Run 6910-01

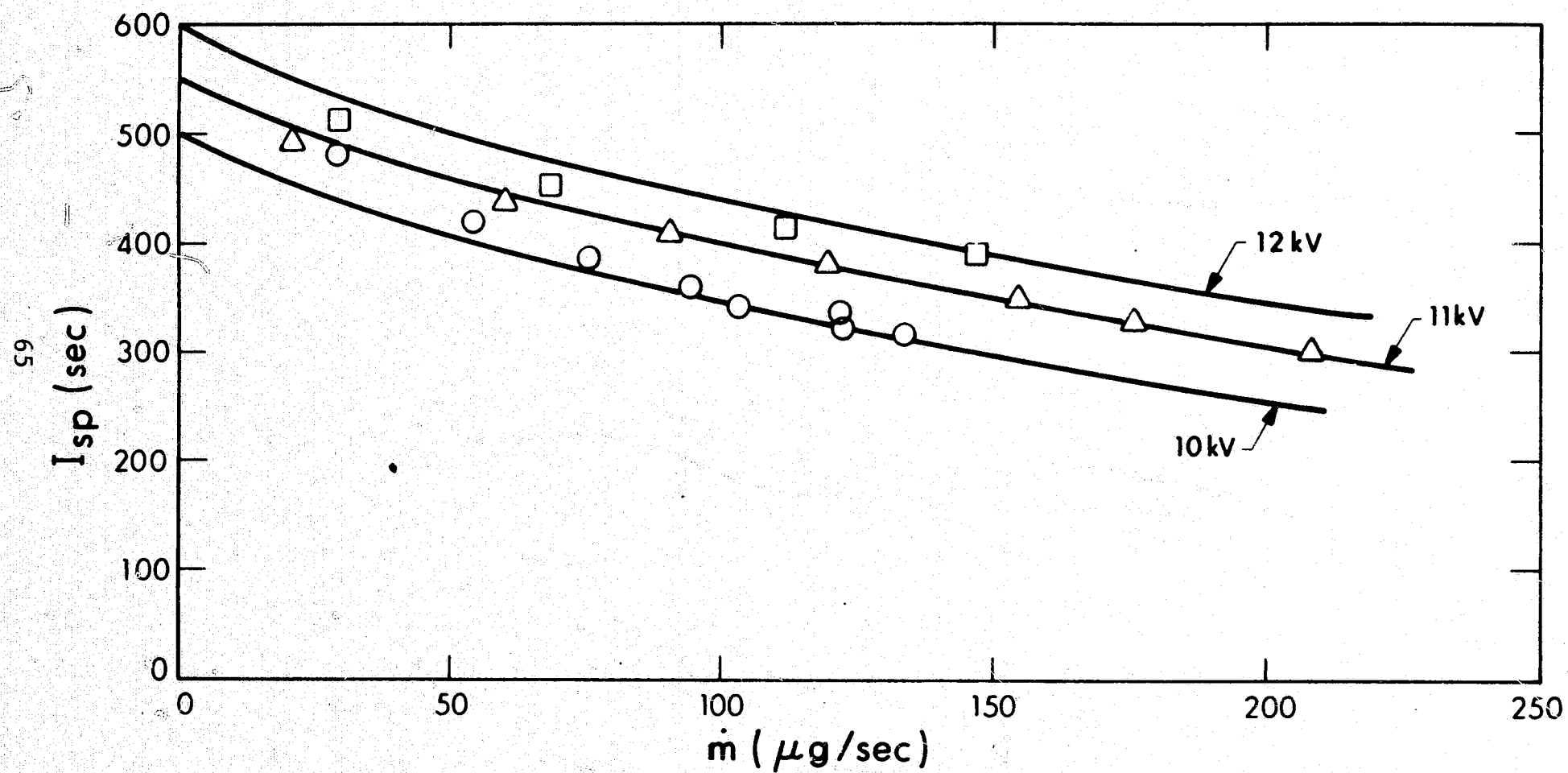


Figure 33. I_{sp} versus \dot{m} for A02, Run 6910-01

Figure 34 compares analytical curves with data for I , T and I_{sp} versus \dot{m} for annulus A06 at two voltages. This also illustrates the effect of V and \dot{m} upon the operational parameters and shows the relation between the different parametric curves. Note that the thrust curves are more linear than the current curves, but that the current curves are a more sensitive measure of the region of operation and therefore more useful as a diagnostic tool. The more linear variation of the thrust is advantageous in thruster operation which extends over more than one region.

4.4 PERFORMANCE INDICES

To illustrate the effects of different performance indices, Figure 35 shows I versus \dot{m} in arbitrary units for a thruster operated with parameters (k_o, P, V) . The maximum occurs at $I = 1, \dot{m} = 2$, with the linear region slope equal to $k_o^2 V$. If just k_o is doubled, the linear slope increases by a factor of four and the maximum shifts to $I = 2, \dot{m} = 1$. If the value of P is doubled, giving parameters $(k_o, 2P, V)$, the linear slope remains the same as the initial curve, but the maximum shifts to $I = 2, \dot{m} = 4$. For parameters $(2k_o, 2P, V)$ the curve shape does not change with \dot{m} , but increases by a factor of four. Finally, increasing V by a factor of two increases the $(k_o, 2P, V)$ curve by a factor of two. Thus, the slope in the linear region can be greatly affected by the value of k_o . Any attempt to increase this slope and therefore the I_{sp} could be made by increasing V and those properties of the thruster which cause k_o to increase. The \dot{m} range of the linear region is determined by V and P , but V is limited by experimental constraints to less than a factor of two variations (12 to 20 kV) to obtain sufficient thrust.

The tests and analysis provided information on the meaning and properties of the performance indices. The specific perveance (P) appears to be a purely geometric term which in conjunction with the voltage determines the accelerating electric field. It depends upon the

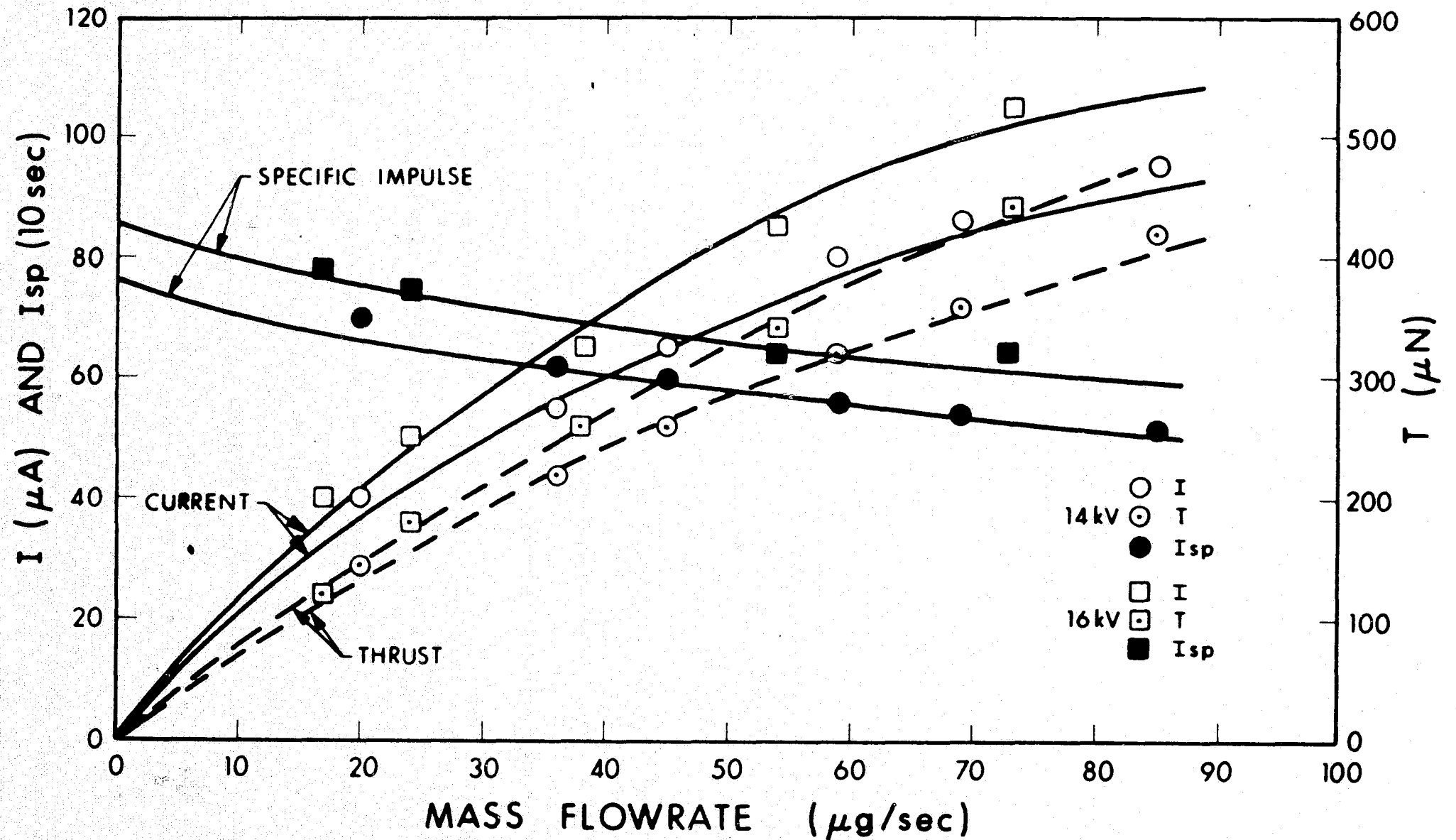


Figure 34. Current, Specific Impulse, and Thrust versus \dot{m} for A06, Run 7005-02

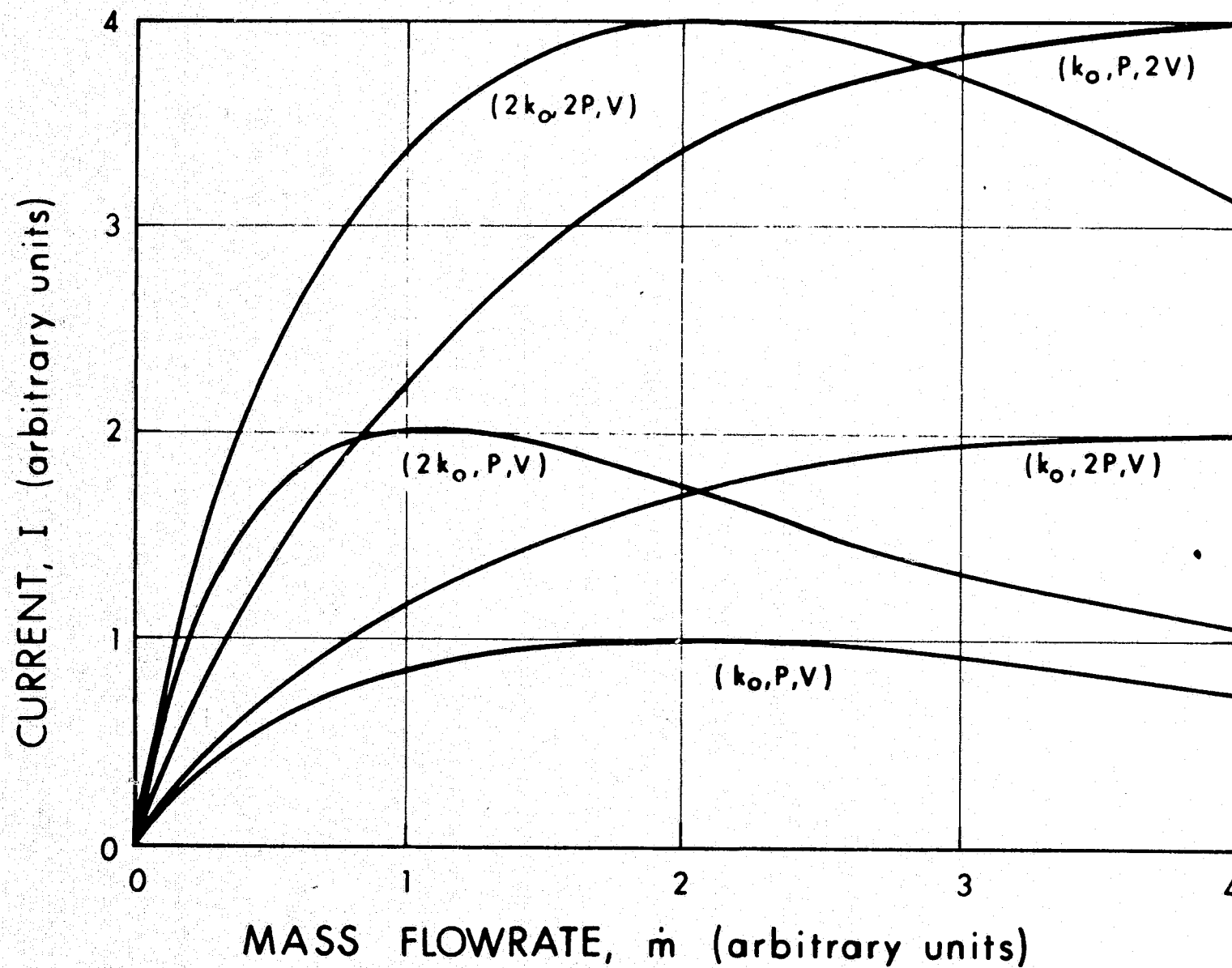


Figure 35. Current versus Mass Flowrate for Various Parameters

propellant meniscus shape and the emission area. For example, if an annulus were not emitting from the entire perimeter the value of P would be decreased. This would not affect the value of k_0 which depends upon the electric field for the generation of the charged particles in addition to such propellant properties as viscosity, conductivity, surface tension, and perhaps dielectric constant and charge concentration. It was noted that tests involving the dependence of the operational parameters upon the emitter temperature, but independent of the mass flowrate, show k_0 to be temperature dependent. Recent tests on temperature effects have been made and are discussed in Section 5. The indications are that the specific charge decreases as the temperature at the emitter increases for constant \dot{m} and V . This change of approximately 10 percent for every 5°C change is significant, but has not as yet been incorporated into the analytical equations. It is probable that the dependence is related to the electrohydrodynamics of the liquid interface determined by the propellant properties. Thus k_0 is associated with charged particle generation and P with beam acceleration properties.

The importance of k_0 and P as performance indices is to characterize the operational parameter range of a thruster. Thus to compare various emitter-propellant combinations, tests can be restricted to those required to determine performance indices. Additional data may be required to determine such operational features as emitter temperature effects, general stability, lifetime, etc. The results of the analysis to determine the performance indices from thruster tests are discussed in Section 5.

4.5 THEORETICAL THRUSTER DESIGN

A thruster can be theoretically designed using this analysis to satisfy performance goals. An example is shown to display the use of the analytical curves and the performance indices. The resulting

performance curves are particularly useful in understanding the trade-offs that can be made to obtain a different performance level from the same thruster such as the increase in thrust that can be achieved by sacrificing I_{sp} .

For operation of a single emitter at 15 kV with a specific charge efficiency of $\eta = 72$ percent, a set of performance indices are chosen to be:

$$k_o = 0.95 \text{ (A sec/kgV)}^{1/2} \quad (42)$$

$$P = 47.5 \times 10^{-13} \text{ (Akg/sec V}^3)^{1/2} \quad (43)$$

This combination is near the state of the art for annulus thrusters and will be used for illustrative purposes. With the indices specified, the operational parameters as a function of mass flowrate at constant voltage are shown in Figure 36. Note that at the 53 μlb level where $X = 0.2$ (Eq. 14), the current is 165 μA and the mass flowrate is 15 $\mu\text{g/sec}$. The tradeoffs between alternate operational modes are also included in Figure 36 and are discussed to illustrate the versatility of operation possible with a given thruster. For example, to obtain four times the thrust (200 μlb) at the same voltage, the mass flow must increase to 93 $\mu\text{g/sec}$ and the current to approximately 410 μA , with a resulting specific impulse of ~ 1000 seconds. This operating point is not in the near linear region, but in the constant current region (where I is independent of \dot{m} or where $X > 1$). An increase in voltage would shift all the curves upward and extend the near linear region out to higher mass flowrates. Thus, 250 μlb could be achieved at a higher voltage with a mass flowrate below 100 $\mu\text{g/sec}$. A thrust of 250 μlb can be achieved at 900 sec by using two or three annuli having performance indices of $k_o \sim 0.7$ and $P \sim 50 \times 10^{-13}$, and operated at approximately 15 kV and 50 $\mu\text{g/sec}$.

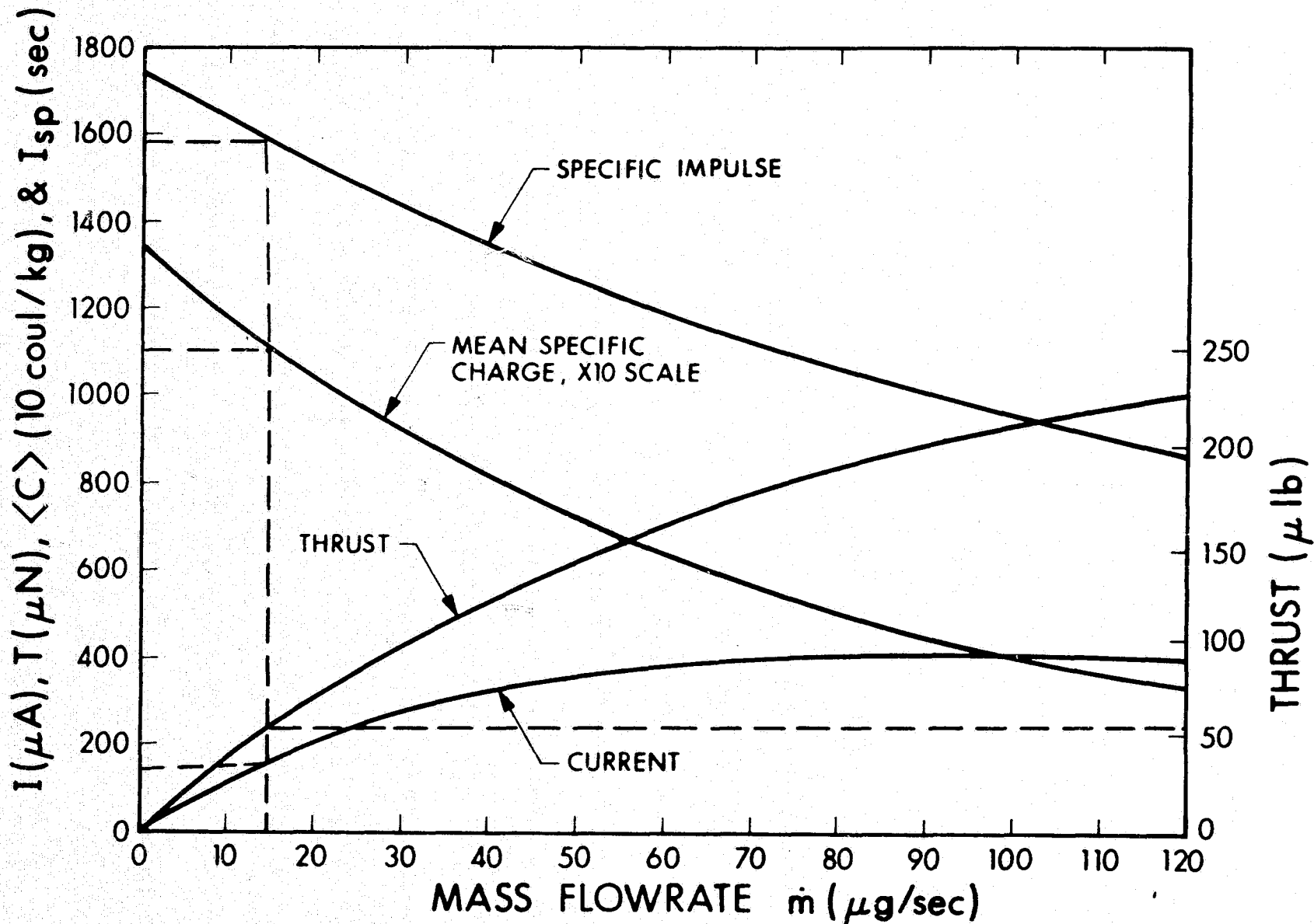


Figure 36. Operational Parameters for a Theoretical Thruster Operated at 15 kV ($k_o = 0.95$, $P = 47.5 \times 10^{-13}$)

SECTION 5

ANNULAR THRUSTER TESTS

5.1 TEST RUNS

A large amount of data were taken during the duration of the program using annular emitters. Each of the test runs (with comments) is listed in Table 3. The emitter configurations were described in Table 1 (Section 2) and the propellant properties were given in Table 2 (Section 3).

5.2 THRUSTER PERFORMANCE

The present state-of-the-art annular thruster performance is characterized by stable, repeatable operation with excellent thermal control and good beam focusing properties. Thruster control variables such as V , \dot{m} , and temperature, have been extended over a wide range without encountering glow discharge or unwanted extractor currents. Recent tests have shown that inner extractor currents can be maintained at less than 1 percent of the total annulus current using proper shielding techniques.

This subsection emphasizes those parameters such as thrust density and specific impulse essential to an evaluation of thruster performance. The parametric data presented will be primarily concerned with data from the most recent tests involving annuli A06 and A09. Results of tests with annulus A01 will also be displayed parametrically and discussed. Selection of A06 and A09 data for presentation is based on the improved thruster performance exhibited by these annuli and the improved conditions under which the data were obtained. By "improved conditions" is meant that the data were taken with a minimum of temperature scatter

TABLE 3
COLLOID THRUSTER TEST RUNS

Run No.	Emitter	Propellant	Comments
6908-01	A01	F01	Large inner extractor currents observed (40 to 70% of total annulus current). Teflon core supporting inner extractor coated with fluid.
6908-02	A01	F01	Teflon core replaced with vacuum core. Concentric cylindrical outer extractor investigated.
6908-03	A01	F01	Large increases in current observed when feed pressures increased. Data showed first hint of linear response of current with mass flowrate.
6908-04	A01	F01	Outer extractor/annulus spacing increased from nominal 0.035 in. to 0.125 in. Evaluation of extractor not complete due to early termination of test caused by inner extractor/annulus short.
6908-05	A01	F01	Determined that inner and outer extractor circuitry required limiting resistors to prevent meters from arcing out.
6908-06	A01	F01	Data taken at 12.5 and 13.5 kV showed good linearity of annulus current with increasing mass flowrate.
6909-01	A01	F02	Performance mapping, 133 hr, run 105 hr at $I_{sp} > 1000$ sec.

TABLE 3

COLLOID THRUSTER TEST RUNS (contd)

Run No.	Emitter	Propellant	Comments
6909-02	A01	F02	Performance mapping, part of 122-hr test.
6910-01	A02	F02	Performance mapping.
6901-02	A02	F02	A02 operated for 100 hours. Emitter erosion was less than that of Type 304 emitter.
6910-03	GSFC	F02	Goddard thruster showed operation in linear and saturated regions.
6911-01	A03	F03	Flow controller constructed on IR&D program tested. Response of annulus current to heat input at the restrictor very slow. Annulus temperatures observed to increase with inner extractor currents.
6912-01	A03	F03	Flow controller test with feed lines heated by infrared lamp. Suspect cold feed lines in previous test provided higher impedance than restrictor.
6912-02	A05	F03	Inner and outer extractor spacing increased from ~ 0.035 in. to $1/16$ in. A05 constructed from same specifications as A01. After assembly A05 had lower impedance by factor of 6. Runaway modes observed with increasing annulus temperature.
6912-03	A05	F03	Flow restrictor used with A05. Stable operation at higher voltage possible but runaway modes still present with increasing annulus temperature caused by inner extractor currents.

TABLE 3

COLLOID THRUSTER TEST RUNS (contd)

Run No.	Emitter	Propellant	Comments
6912-04	A01	F04	Data acquisition system and thyratron successfully operated with an annulus.
7001-01	A03	F04	Mass flow meter and flow controller operated successfully with annulus. I versus m data agreed with theory.
7002-01	A06	F04	A06 operated with I_{sp} between 525 to 770 seconds. Design shows promise for obtaining higher specific impulses.
7002-02	A06	F04	Continuation of 7002-01 with more temperature control and data taken as function of pressure, voltage and temperature.
7002-03	A03	F03	Photomultiplier used to monitor annulus glow. Sodium spectra identified.
7003-01	A08	F04	20Cb3 S.S. shows more erosion than Pt/Ir material.
7004-01	A06	F05	Test using 30 gms NaI/100 ml glycerol propellant fluid. Specific impulses lower than expected.
7004-02	A06	F05	Inner extractor guard not effective in preventing inner extractor currents.
7004-03	A06	F05	Test with hemispherical extractor. Glow related to backstreaming electrons.
7004-04	A06	F05	Electron shield electrode stops glow. Shown to be effective in reducing inner and outer extractor currents.

TABLE 3

COLLOID THRUSTER TEST RUNS (contd)

Run No.	Emitter	Propellant	Comments
7005-01	A06	F05	The 0.200 dia. spherical extractor replaced with 0.250 dia. extractor. No glow observed at 17 kV operation. Inner extractor currents less than 1% of total annulus current.
7005-02	A06	F05	The 0.313 dia. spherical extractor replaced 0.250 dia. extractor. Inner extractors again less than 1% of annulus current. Outer extractor currents observed, but reduced significantly by applying positive voltage. Electron guard shield prevented backstreaming electrons from triggering glow even when outer extractor biased positively.
7006-01	A09	F05	New emitter design test A09 gave higher specific impulses than A06 under similar operating conditions. Annulus current observed to be linear with mass flowrate past 120 $\mu\text{g}/\text{sec}$ (215 μA).
7006-02	A06	F05	Test designed to determine dependence of q/m on temperature at constant voltage and mass flowrate. q/m found to decrease with temperature.

and little or no glow discharge and, therefore, small scatter in the data. Parametric plots depicting the performance of the GSFC thruster tested at EOS is also described in this section along with a discussion of beam focusing effects and mass flowrate variations with feed pressure, temperature, and voltage. Due to the importance of temperature and its relation to thruster performance in terms of mass flow and charged particle generation, parametric data showing the variation of q/m with temperature will be given later in this section. All of the emitters tested on this program are classified according to their performance using the performance index system developed in the analytical study.

5.2.1 PARAMETRICS

Annulus A06 was designed to provide a high impedance at the emitter edge. As a result, operation was limited to the region where the current varies linearly with mass flowrate as defined in Section 4. Note that the linear region was defined by limiting the analytical current deviation from the initial straight line by 20 percent. In this case the current remains within 10 percent of an average straight line which approximates the experimental error. In this linear region the thrust is within 5 percent of the average straight line shown in Figure 37 for annulus A06. The thrust is plotted versus mass flowrate at three different voltages and at a constant temperature of -6°C . The reduced data for this run (7004-04) showed that the specific impulse did not vary significantly at constant voltage over the measured range. For this reason the average specific impulse, noted for each voltage, increased approximately 27 sec/kV. This variation is consistent with the analytical expression for I_{sp} , discussed in Section 4.

A plot of thrust versus \dot{m} (run No. 7005-02) at higher temperature is shown in Figure 38. Although the same annulus (A06) was used for this test, the mass flow region was extended somewhat beyond the linear

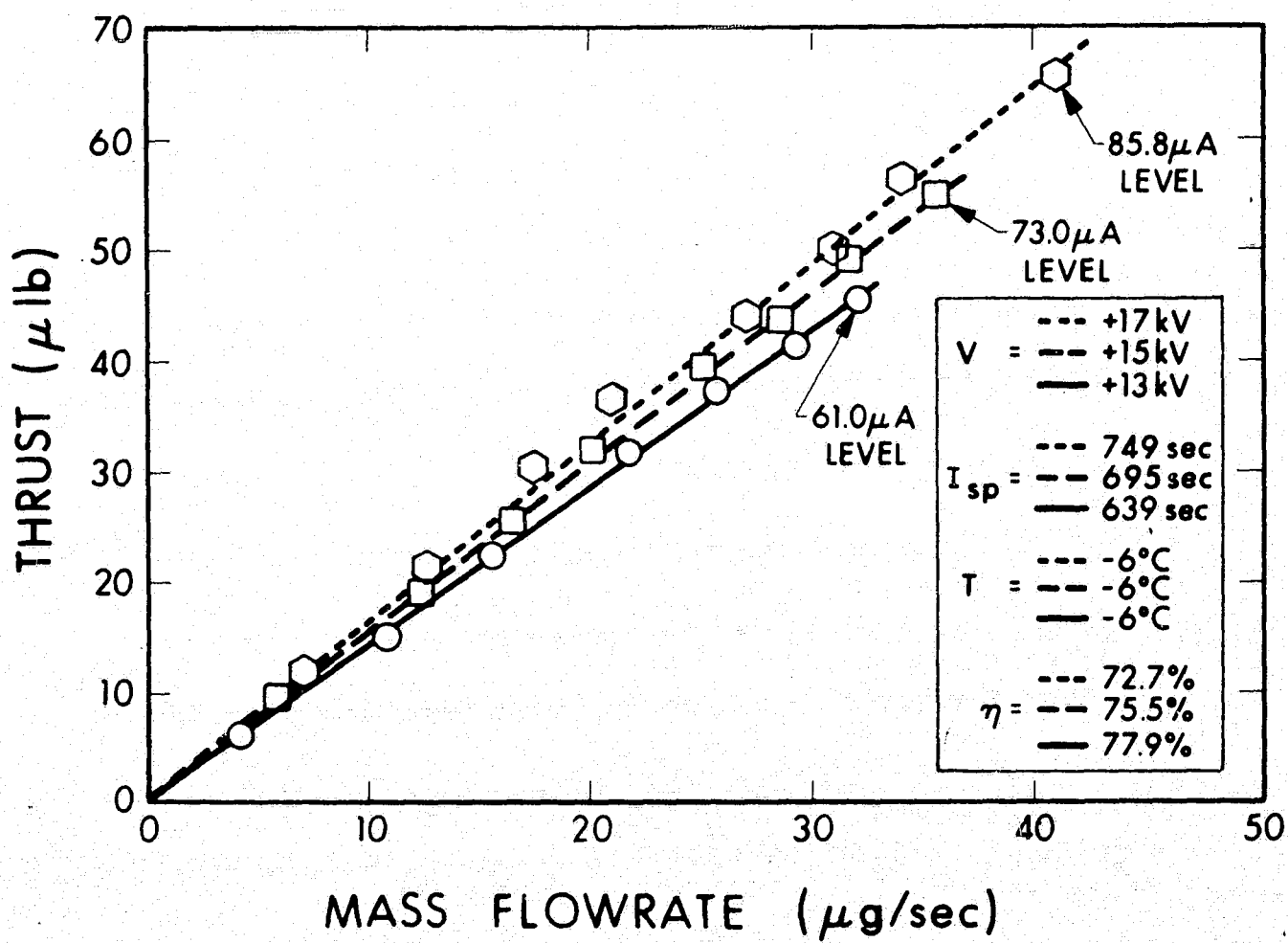


Figure 37. Mass Flowrate versus Thrust at a Constant Temperature for Annulus A06, Run 7004-04

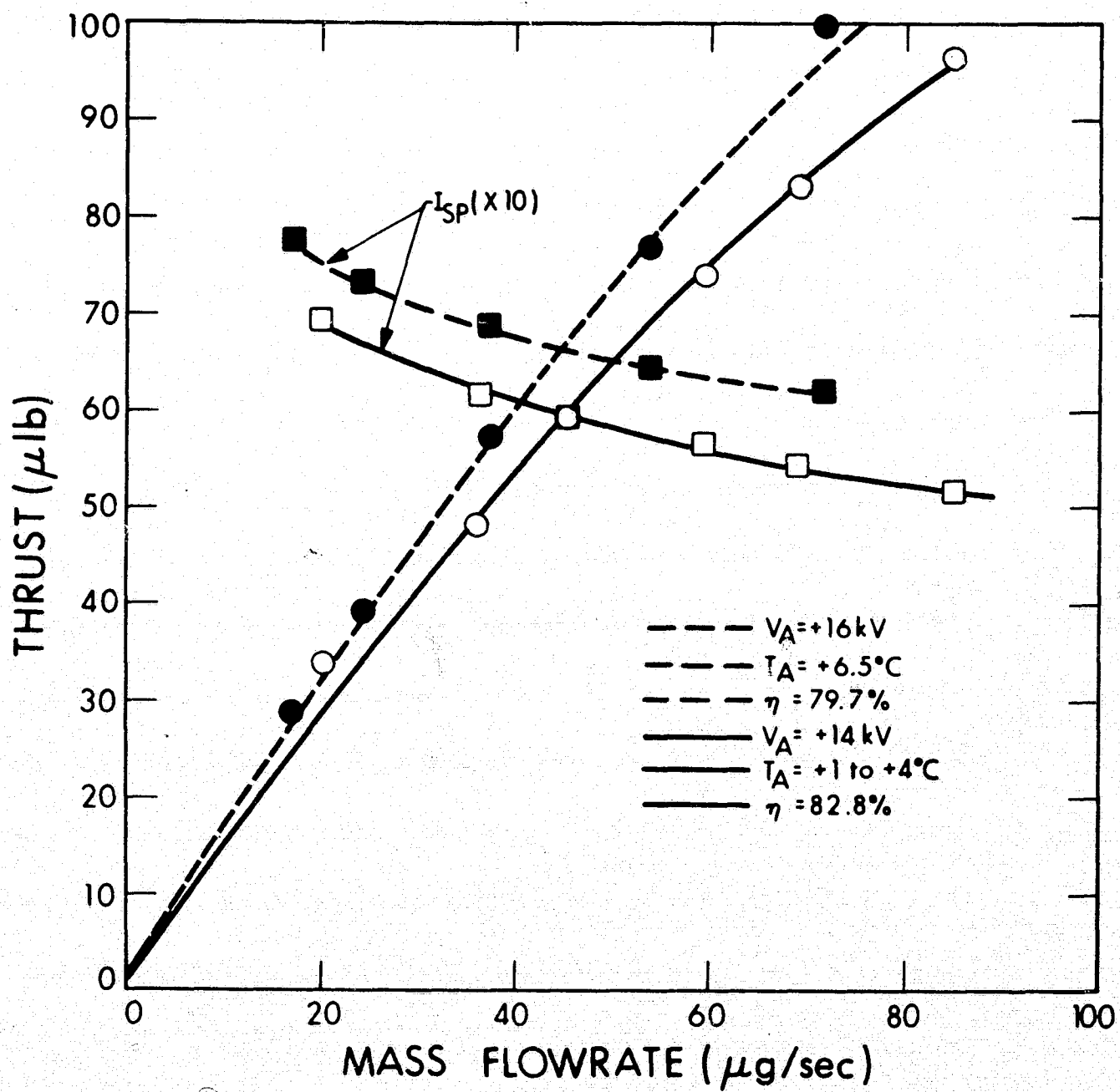


Figure 38. Mass Flowrate versus Thrust at Various Temperatures
For Annulus A06, Run 7005-02

region due to increases in temperature. The decreasing specific impulse with increasing \dot{m} , also shown in Figure 38, conforms with the analytical study. The specific impulse lies between 600 to 800 seconds at 16 kV and 500 to 700 seconds at 14 kV for higher and lower temperatures, respectively. It should be mentioned that in both Figures 37 and 38 the specific charge efficiency is greater than 70 percent and remains nearly constant at a constant voltage. In general, it is seen that the specific charge efficiency increases with decreasing voltage.

Operational parameters for annulus A09 are plotted in Figure 39. The source current, thrust, and specific impulse are plotted versus mass flowrate for two different temperatures. At a constant temperature and voltage, the range of feed pressures available and the annulus impedance determines the operational mass flow range. As annulus A09 had a smaller geometrical impedance than A06, the operational mass flow range was extended. The source current and thrust density shows linearity at mass flowrates up to 140 $\mu\text{g}/\text{sec}$ which is the widest range where linearity has been demonstrated. Thruster performance (related to program goals) is superior in the linear portion because of higher specific impulse and better beam focusing. The most interesting data are the 174 μlb achieved at 550 seconds by one annulus operated at only 13 kV. The annulus was operated with an electron guard shield to prevent backstreaming electrons from triggering glow discharges and inner extractor currents. The extremely low emitter, extractor (I_{ix} and I_{ox}), and shield currents (I_s) listed in Table 4, substantiate the effectiveness of the shield when the emitter was operating at high levels.

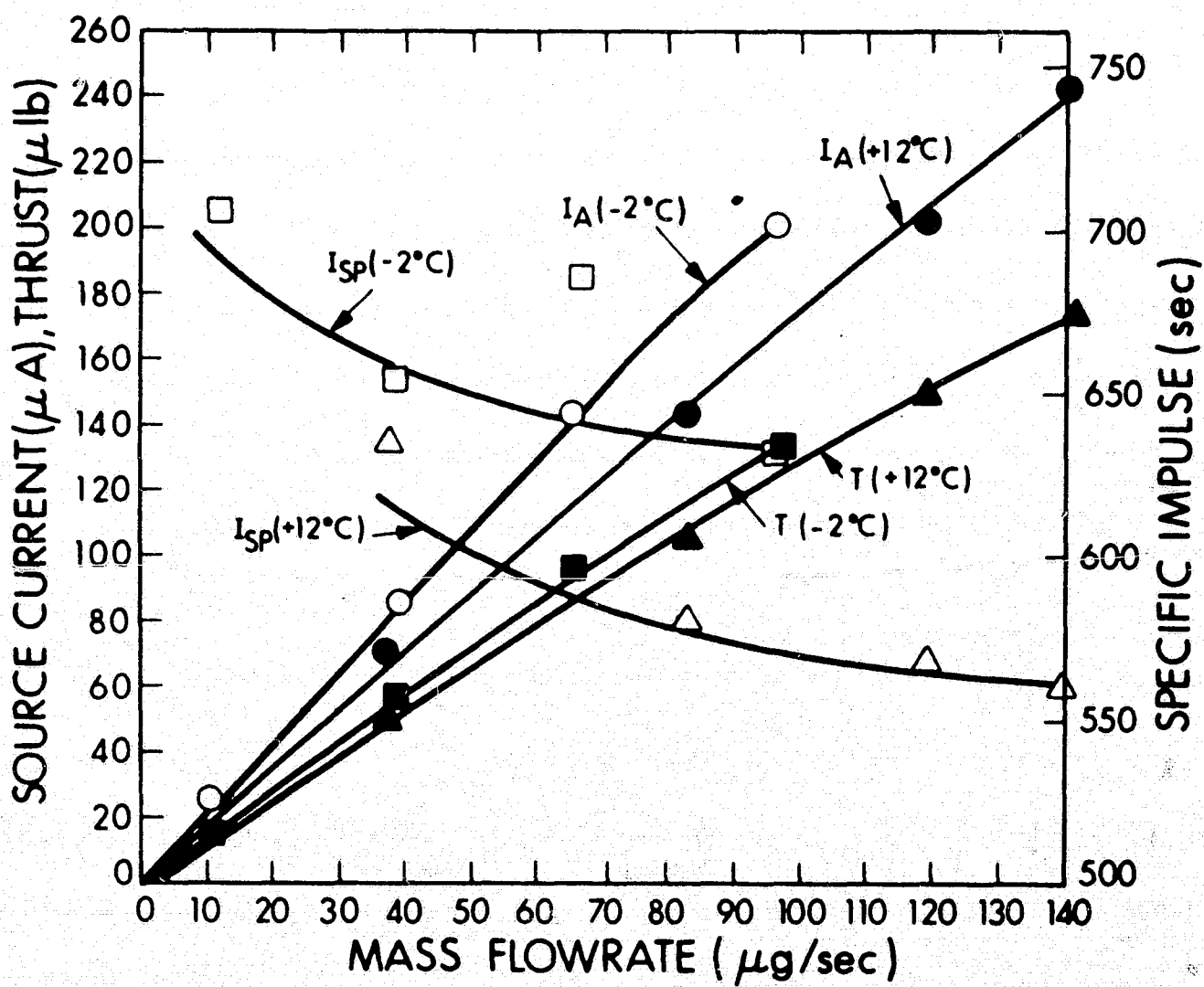


Figure 39. Operational Parameters versus Mass Flowrate
For Annulus A09, Run 7006-01

TABLE 4
RUN 7006-01 EXTRACTOR CURRENTS

<u>V (kV)</u>	<u>I (μA)</u>	<u>I_{ix} (μA)</u>	<u>I_{ox} (μA)</u>	<u>I_s (μA)</u>	<u>T ($^{\circ}$C)</u>
13	27	0	0	1.3	-2 $^{\circ}$
13	88	0.1	0.3	3	-2 $^{\circ}$
13	150	0.2	0.3	5.5	-2 $^{\circ}$
13	200	0.3	0.4	7	-2 $^{\circ}$
13	75	0.1	0.3	3.5	+12
13	150	0.4	0.3	6	+12
13	210	0.6	0.5	5.6	+12
13	250	1.0	0.6	6.2	+12

To increase the specific impulse, annulus emitter A09 was constructed with 0.001 inch edges compared to 0.002 edges for annulus A06. To illustrate the effect of smaller rim size on specific impulse, thruster performance data are plotted in Figure 40 for A06 and A09 operated under similar conditions. In the region between 6 and 40 μ g/sec, the specific impulse for A09 lies between 750 and 900 seconds while the specific impulse for A06 is in the 690- to 700-second region. Because the data for A06 under these conditions did not extend beyond 40 μ g/sec, a more complete comparison could not be made.

Annulus A01 was designed to operate in the low mass flowrate region and had a high-impedance shelf to restrict the mass flow. Data taken over a range of feed rates and voltages are shown in Figure 41. The figure is a log/log plot of specific impulse versus thrust, showing lines of constant \dot{m} and beam power (ηIV). The data, taken over a voltage range from 10 to 18 kV, show a nearly constant specific impulse over a range of thrust levels, then decrease more rapidly at the higher thrust. These variations correspond to the linear region at low \dot{m} and to the constant current region at high \dot{m} , respectively. With increasing voltage this type performance is maintained and shifted

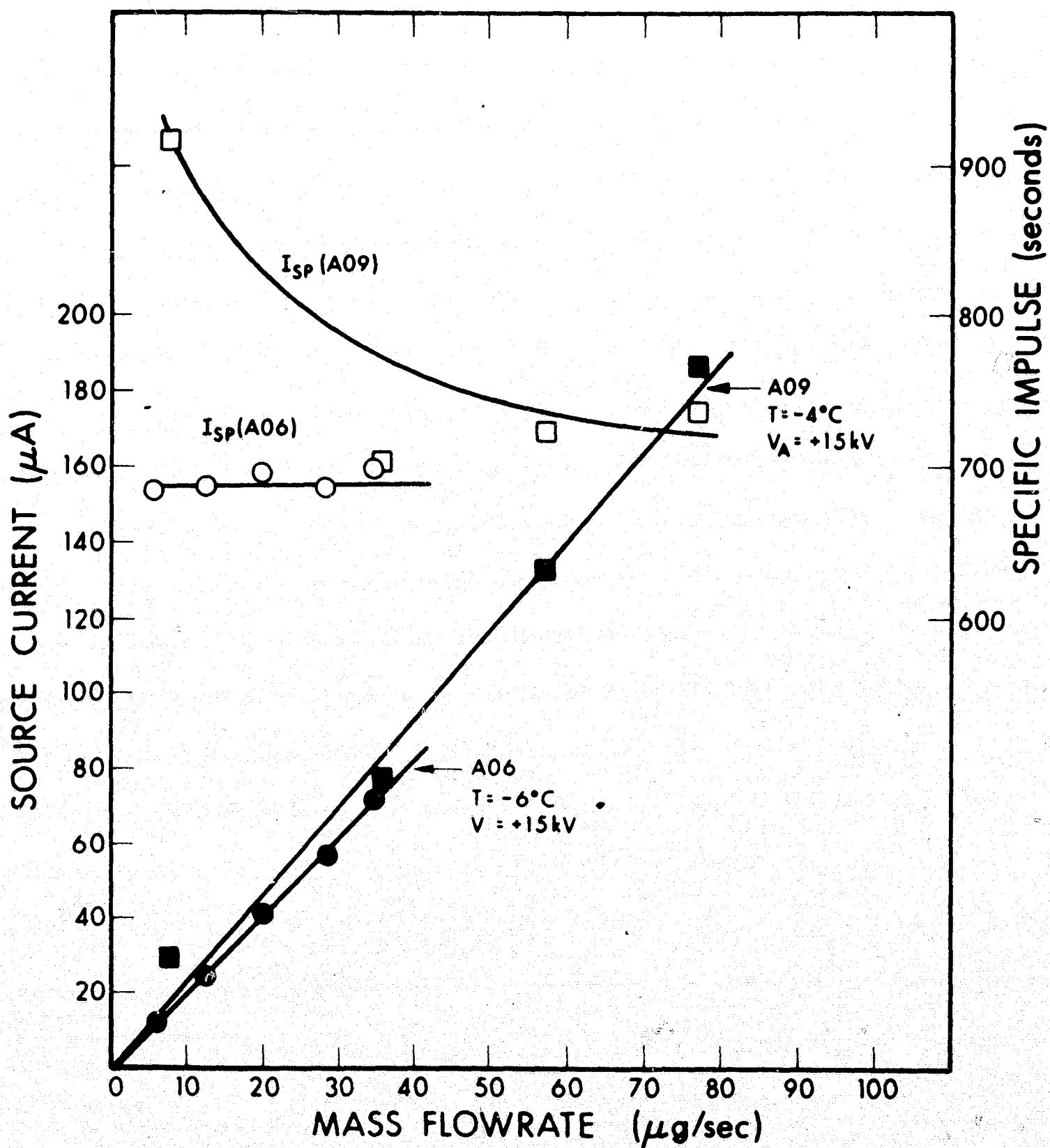


Figure 40. Effect of Smaller Rim on Thruster Performance
For Run 7004-04 (A06) and 7006-01 (A09)

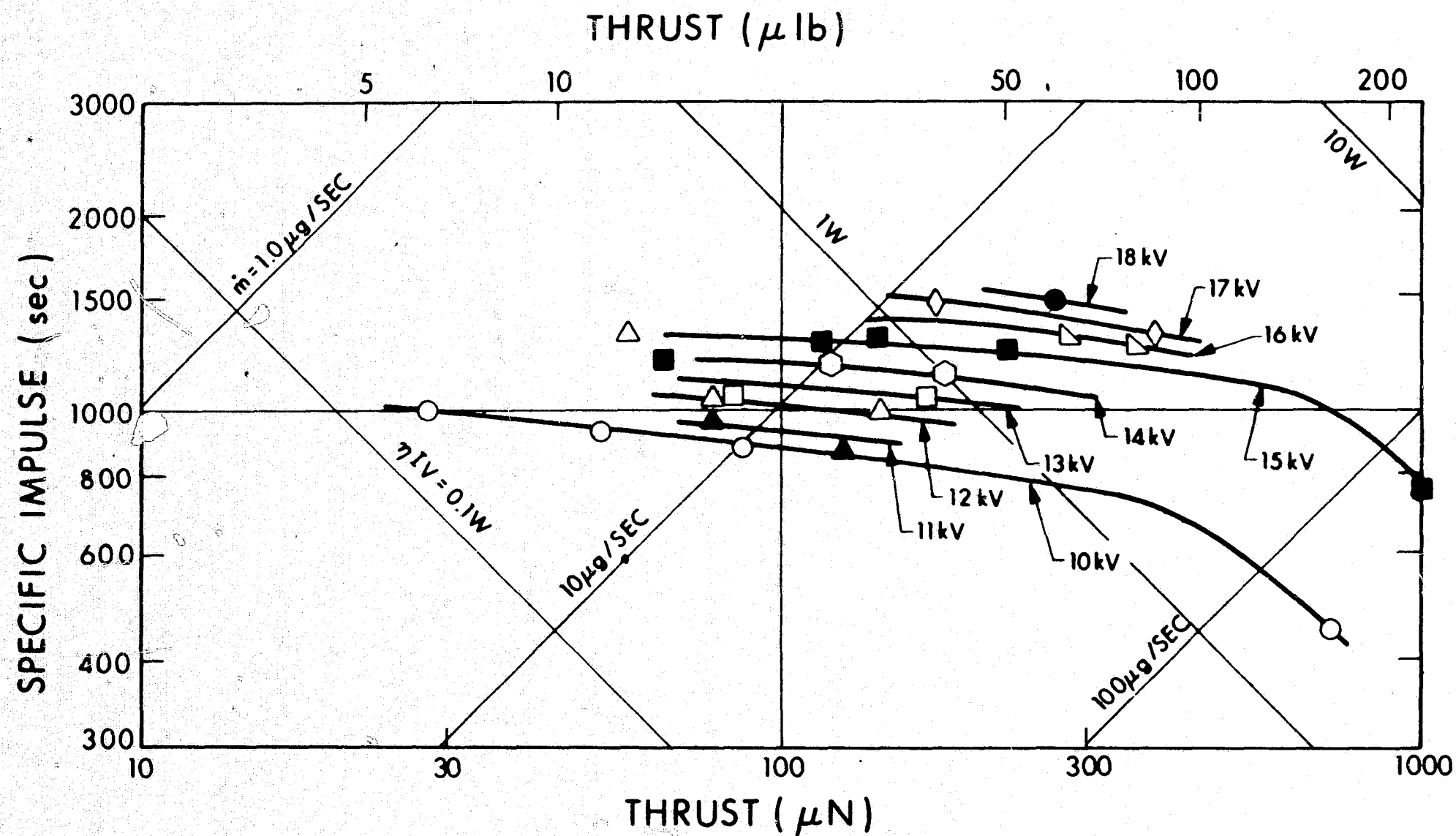


Figure 41. Variation of Specific Impulse with Thrust for Annulus Parametric Study (Annulus A01)

toward higher specific impulse and thrust. The variation with voltage is clear, although the higher \dot{m} regions were not examined thoroughly. The 15 kV data indicates a thrust of nearly 200 μ lb and I_{sp} of about 900 seconds. This plot can be used for extrapolating beyond the measured data to obtain a thruster capability at other ranges of operation.

5.2.1.1 GSFC Thruster Test

In collaboration with A. Sherman and W. Burton of GSFC, a Goddard thruster was tested at EOS using the 2-by-3-foot vacuum chamber colloid test facility and was designated run 6910-03. The thruster was operated continuously for approximately 22 hours and was run overnight unattended. The low annulus current observed in this test at EOS may be explained partially by the smaller emission lengths of the GSFC annulus compared to EOS thrusters and perhaps lower temperatures due to LN_2 cooling in the EOS chamber. In addition, it is felt that the absence of an inner extractor, and the larger gap spacing between the outer extractor and annulus result in lower fields at the emitter tip at similar voltages. The comparison given in Table 5 of the EOS and GSFC thruster and test environments may help explain the major differences in operation:

TABLE 5

COMPARISON OF GSFC-EOS ANNULUS THRUSTERS AND TEST FACILITIES

Parameter	GSFC	EOS
Emission Length	0.24 in.	1.5 in.
Gap Spacing	0.002 in.	0.001 in.
Inner Extractor	No	Yes
Chamber Pressure	10^{-5} torr	10^{-6} torr
LN_2 Cooled Liner	No	Yes

Data obtained with the thruster indicated operation in the linear region at 18 kV, and in the saturated region at 12 and 16 kV (see Figure 42). These data also lend support to the analytical equation of the current versus mass flow for a different design emitter.

Figure 43 shows a plot of specific impulse versus mass flow. Note that the specific impulse for the 18 kV data remains roughly constant as predicted for operation in the linear region. Figure 44 shows a plot of thrust versus mass flow.

5.2.2 BEAM FOCUSING EFFECTS

Colloid emitters sometimes produce highly divergent charged particle beam accompanied by poor performance such as low I_{sp} , etc. Focusing techniques were investigated for capillary needles by shaping or introducing new electrodes (Ref. 14). Recent measurements of the beam convergence for an annulus show a direct correlation between the region of operation and beam shape. A collection efficiency defined as the ratio of the TOF collector current to the emitter current was measured for each data run. This efficiency is a measure of the percentage of the beam confined to a half angle of 28.5° (see Figure 2).

Figure 45 shows a plot of the collection efficiency versus \dot{m} for the GSFC emitter that clearly illustrates the results of most emitter tests. At a constant voltage the efficiency increases with \dot{m} in the linear region. For increasing \dot{m} , it reaches a maximum then decreases. The curve shifts to higher values and the maximum to higher \dot{m} as the voltage is increased. Note the poor characteristics at 12 kV where the maximum is below the measured \dot{m} range and the beam is highly divergent at the highest flowrate. Increasing convergence with increases in V and with decreasing \dot{m} have been observed in the past, but the existence of a maxima and the decrease in convergence for values of \dot{m} below the maxima were not observed (or even predicted) in the past.

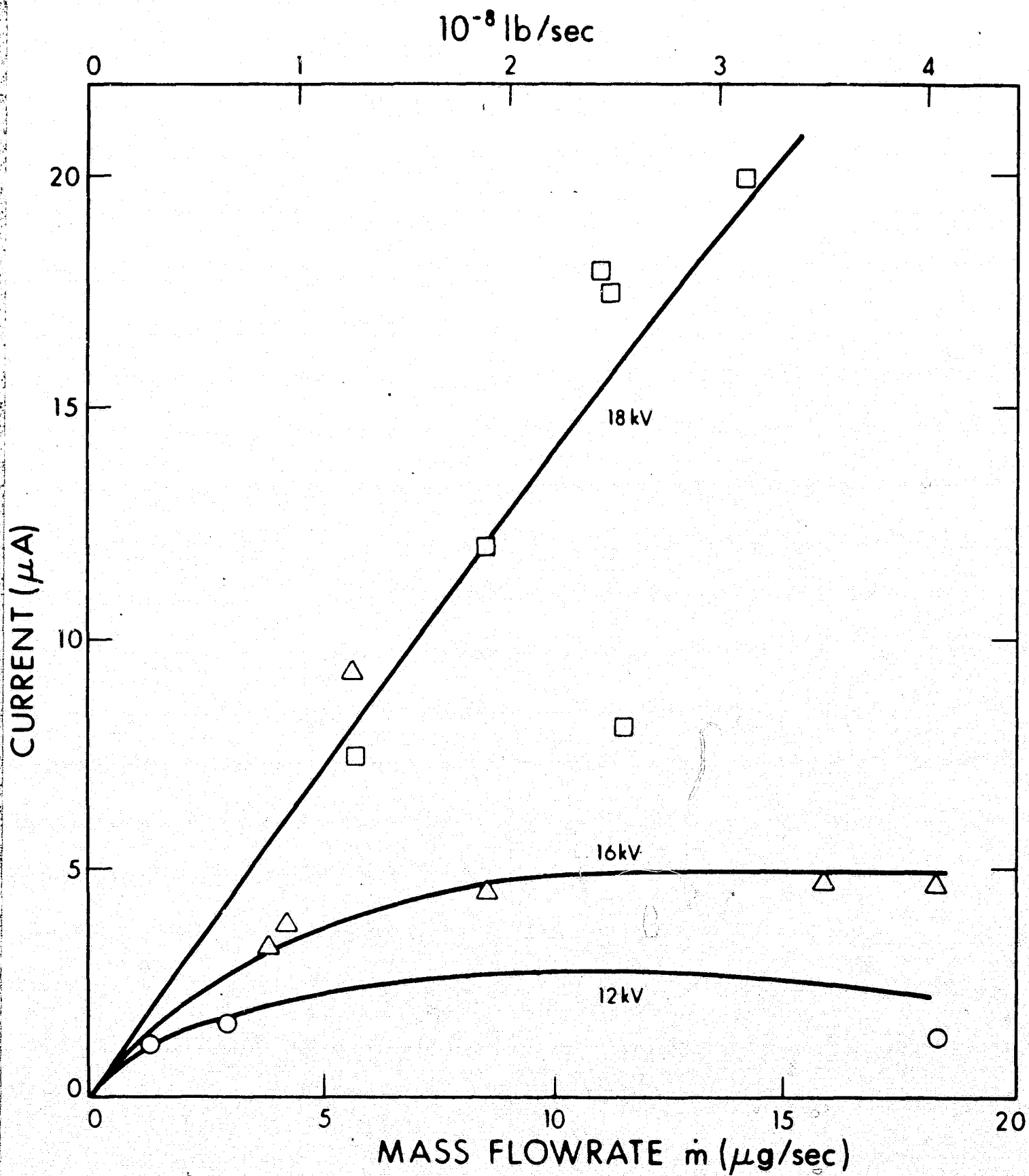


Figure 42. I versus \dot{m} for GSFC Thruster, Propellant F02, Run 6910-03

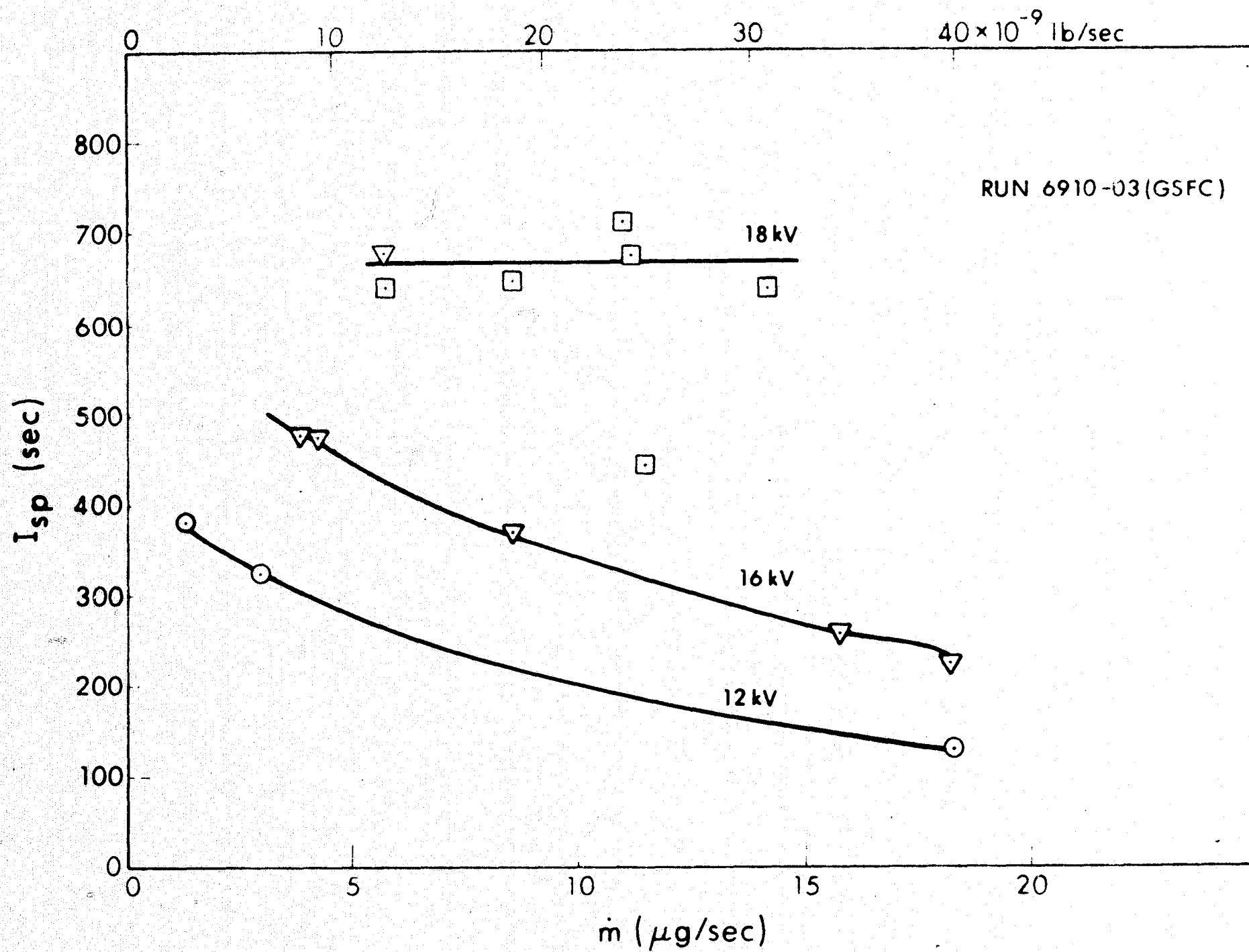


Figure 43. Specific Impulse versus Mass Flow (Run No. 6910-03-GSFC)

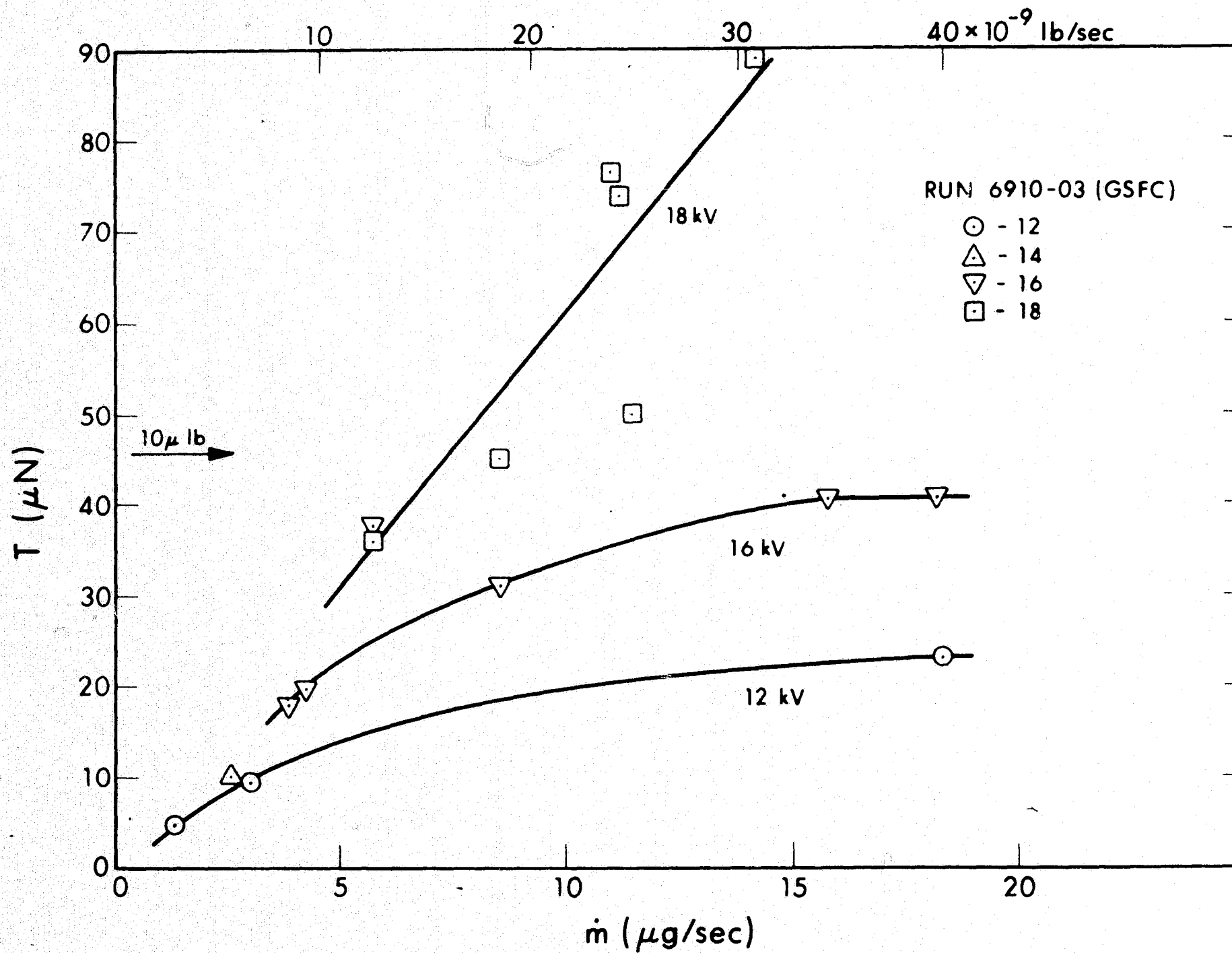
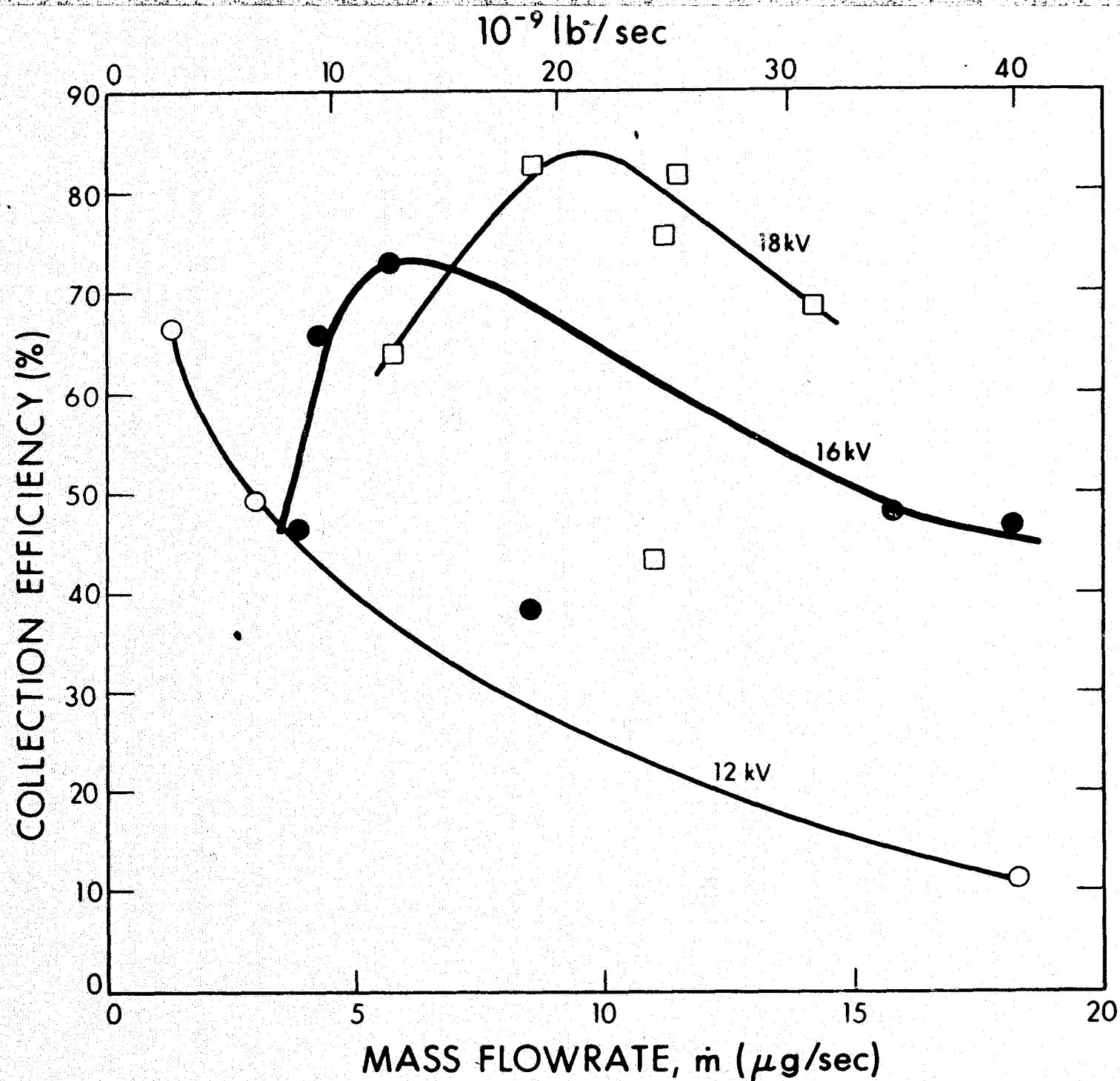


Figure 44. Thrust versus Mass Flow (Run No. 6190-03-GSFC)

Figure 45. Collection Efficiency versus \dot{m} , Run 6910-03

The effect of an inner extractor on collection efficiency was examined at the conclusion of test run No. 6912-01, using annulus A02 with the inner extractor tied to annulus potential to correlate EOS thruster operation with the GSFC thruster. The most striking effect of this modification was the decrease in collection efficiency resulting from higher beam spread which indicates that an inner extractor has the effect of converging the beam which is important for maintaining thrust efficiency and is a desirable feature for vectoring purposes. This decrease in collection efficiency is depicted in Figure 46. The data shown for 9, 10, 11 and 12 kV were taken with the inner and outer extractors biased negatively. The data taken at 14, 16 and 18 kV were obtained with the inner extractor tied to the annulus potential. Notice that the efficiency collection is considerably less for the latter data even though the operation was at higher voltages.

The effect of temperature upon beam spread is shown in Figure 47. The maximum in the collection efficiency curves decreases with increasing temperature and shifts toward higher mass flowrates. At constant mass flowrates, the collection efficiency is higher for the lower temperature data. This is not surprising since $\langle q/m \rangle$ increases with decreasing temperature (see Subsection 5.2.4) and the higher $\langle q/m \rangle$ particles are better focused than the lower $\langle q/m \rangle$ particles which tend to be distributed nearer beam extremities.

5.2.3 MASS FLOW PARAMETRICS

The effects of various parameters upon mass flowrate was measured in recent tests using emitter A06 which has the highest impedance to mass flow at the annulus. The results show the mass flowrate to be dependent on voltage, feed pressure and annulus temperature over the measured ranges. An analytical expression in a general form is presented which enables the mass flowrate to be computed as a function of V, emitter temperature and feed pressure.

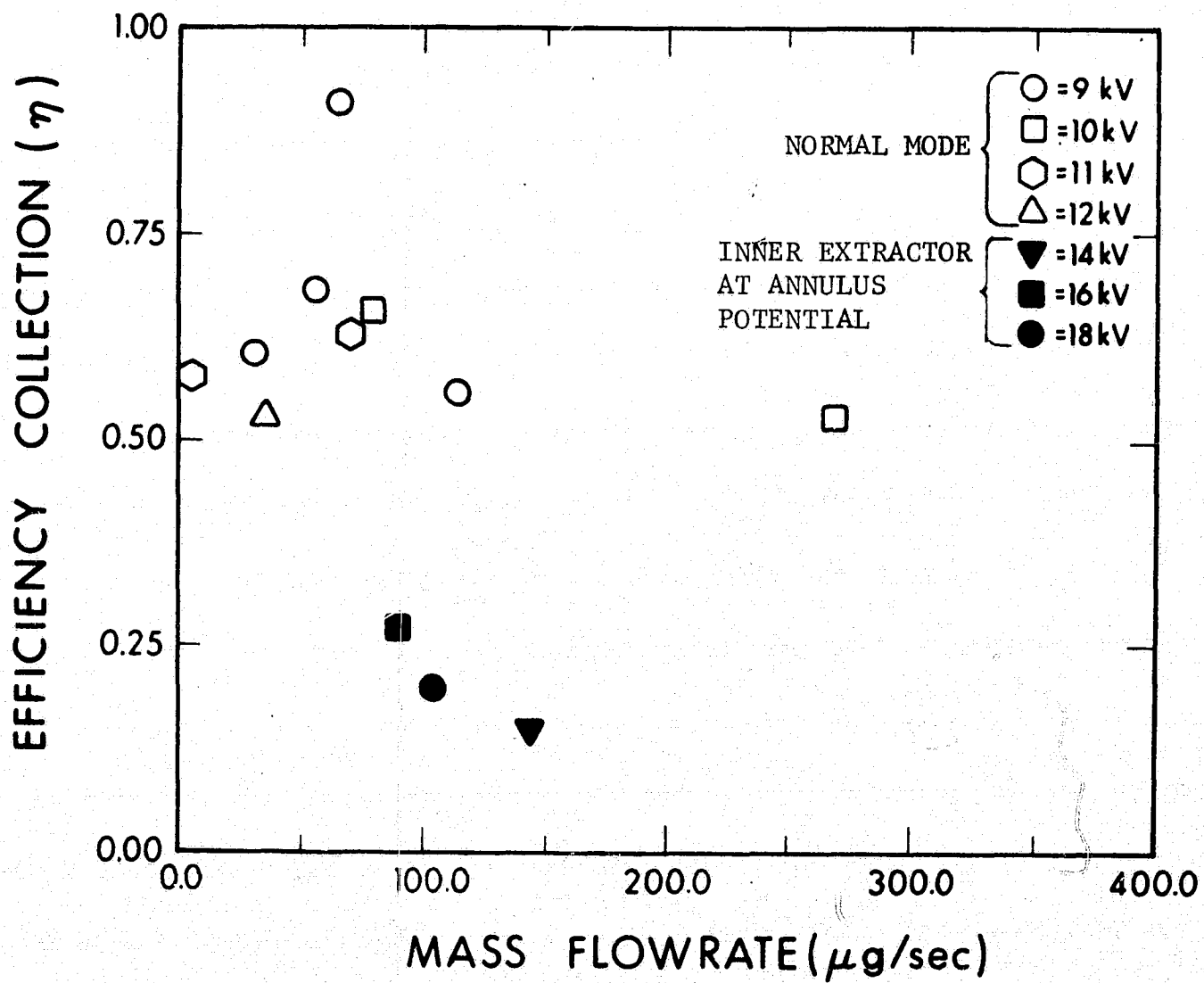


Figure 46. Efficiency Collection versus Mass Flow Emitter A02 - Run 6912-01

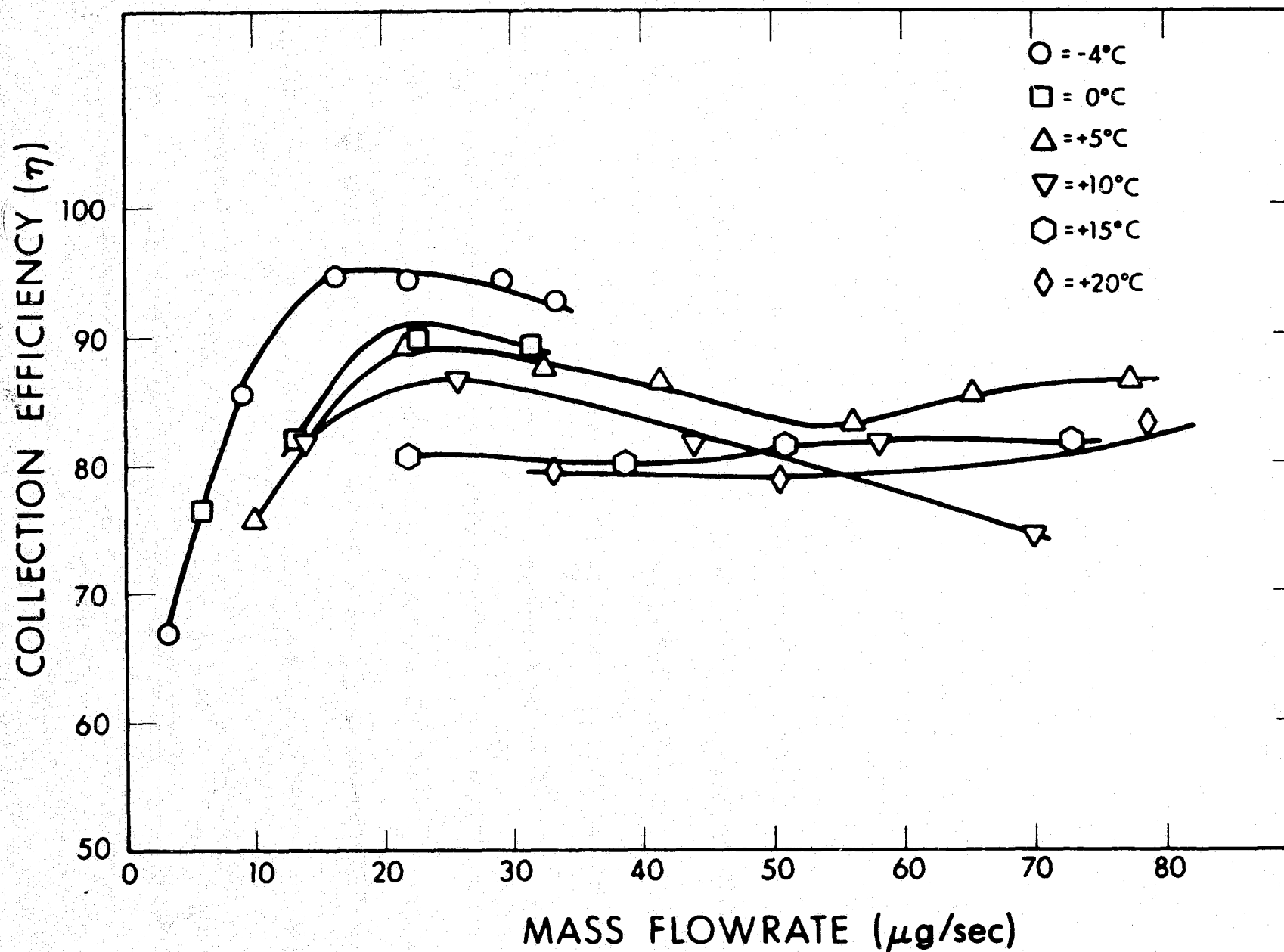


Figure 47. Collection Efficiency versus Mass Flowrate as a Function of Temperature at 15 kV for Annulus A06 (Run 7006-02)

The variation of \dot{m} with the annulus temperature at constant annulus voltage and four values of feed pressure is shown in Figure 48. The exponential character of the variation is directly attributed to the variation of fluid viscosity with temperature. From the data, therefore, mass flowrate dependence on temperature has the form $\dot{m} \propto \exp(bT)$ corresponding with the inverse of the viscosity variation with temperature.

The variation of mass flowrate as a function of feed pressure for four different temperatures and a constant voltage is seen to vary linearly as expected (Figure 49). Extrapolations of the straight lines intersect at approximately -50 torr for $\dot{m} = 0$ with the slopes determined by the temperature. Hence the mass flowrate variation with the pressure can be expressed as $\dot{m} \propto (P_f + P_o)$ where P_o is a constant.

In run 7002-02, sufficient voltage variation was achieved to obtain mass flowrate as a function of voltage. Figure 50 shows a plot of mass flowrate as a function of voltage at constant feed pressure. There was some scatter in the data due primarily to temperature variation on the order of a few degrees. For the measured voltage range the \dot{m} variation was approximately linear with voltage or $\dot{m} \propto (V - V_o)$ where V_o is a constant. As a result of this variation, the specific impulse remained nearly constant when the source voltage was increased from 10 to 17 kV. This effect is a consequence of \dot{m} increasing more rapidly than V . From the analytical expression for the specific impulse (Eq. 32) $I_{sp} \propto f(X)V$, the value of $f(X)$ decreases with $X (\propto \dot{m}/V)$ by approximately the same factor as V increases. From a thruster performance standpoint, in this mode of operation the specific impulse cannot be significantly increased with increasing voltage unless the mass flowrate is maintained constant. This is an important consideration in the design of a thruster system and provides a further need for a mass flowmeter and controller. Not all of the tests indicated this strong variation of \dot{m} with V . The

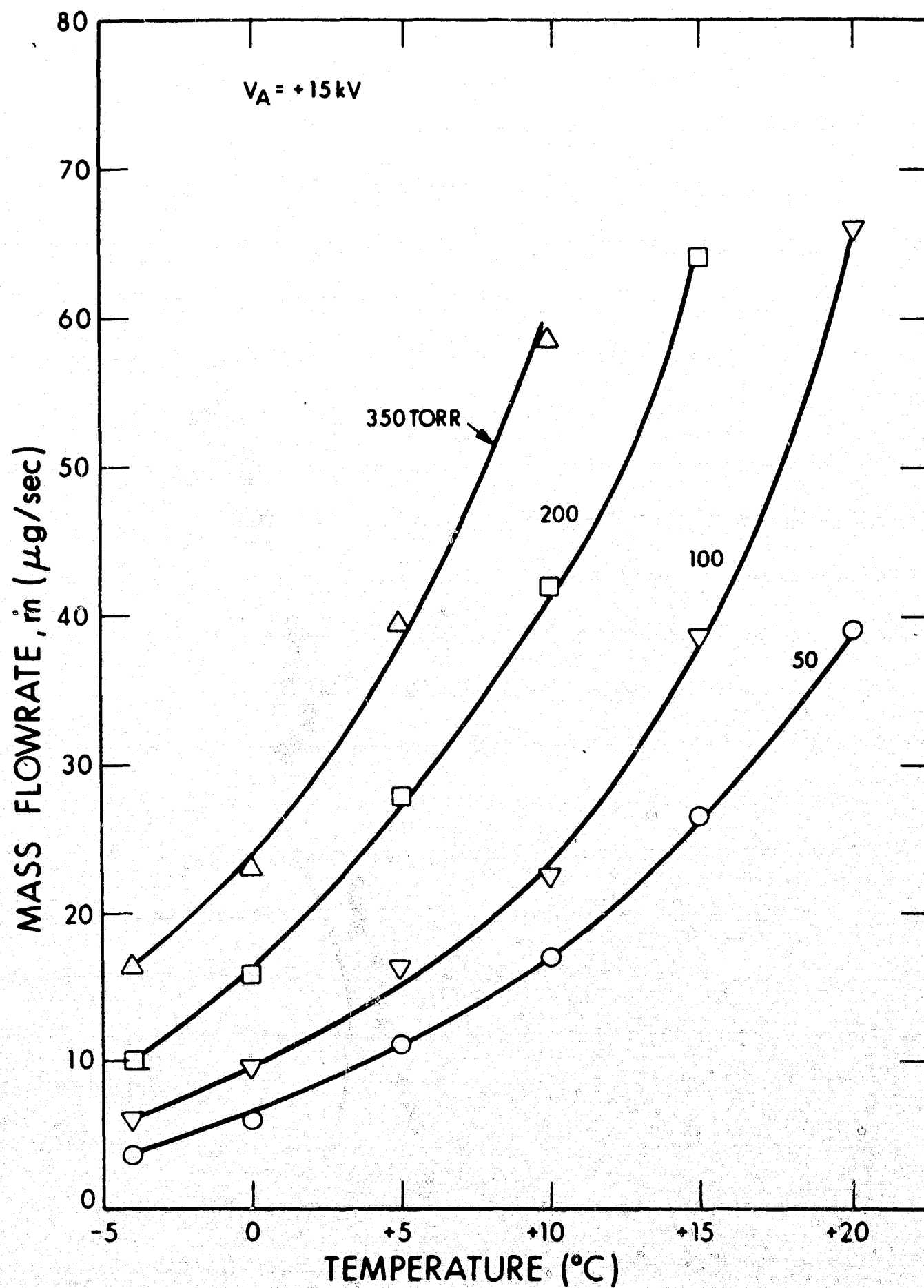


Figure 48. Effects of Feed Pressure on Mass Flowrate
For Annulus A06, Run 7002-02

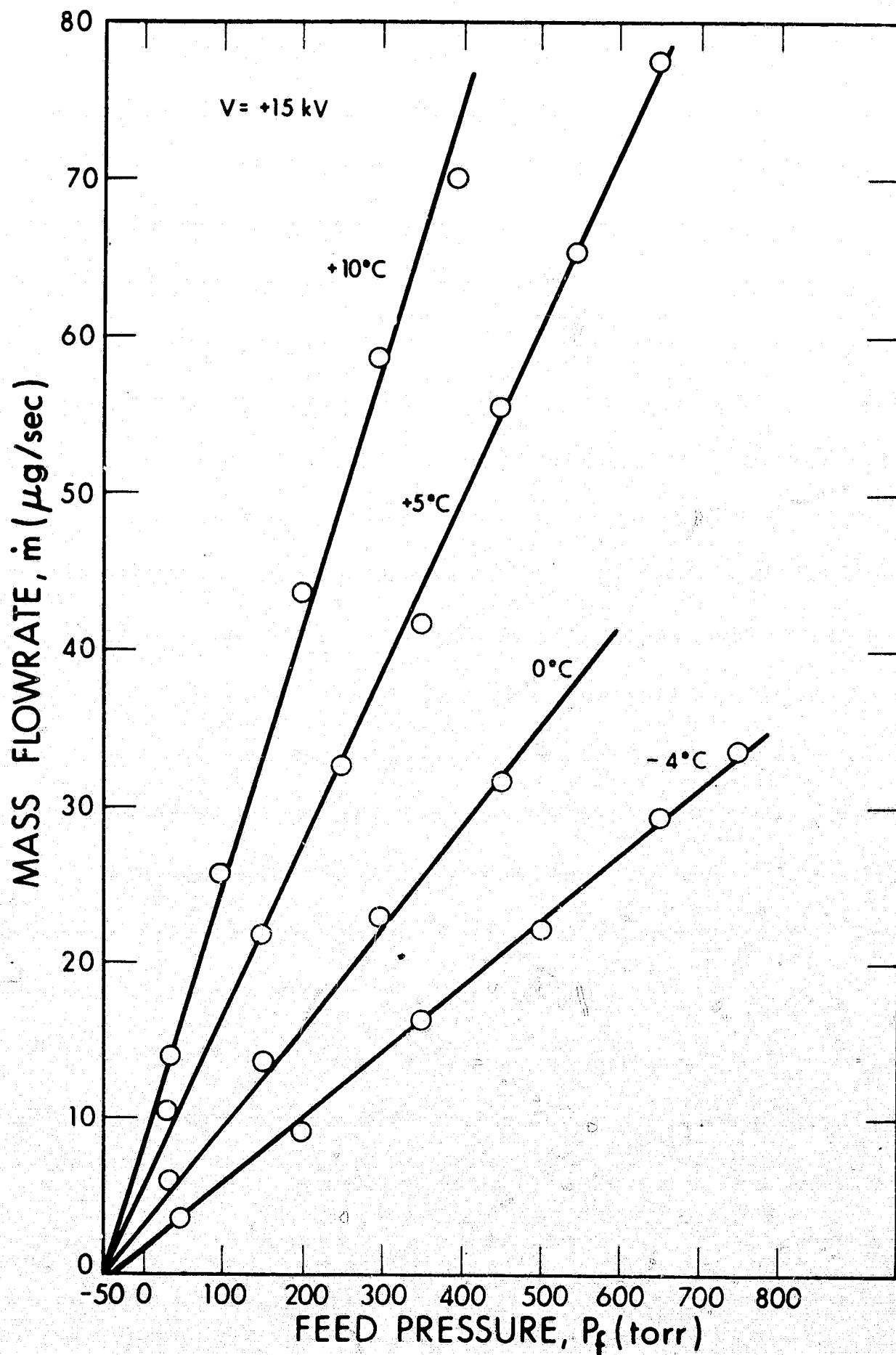


Figure 49. Effects of Temperature on Mass Flowrate
For Annulus A06, Run 7006-02

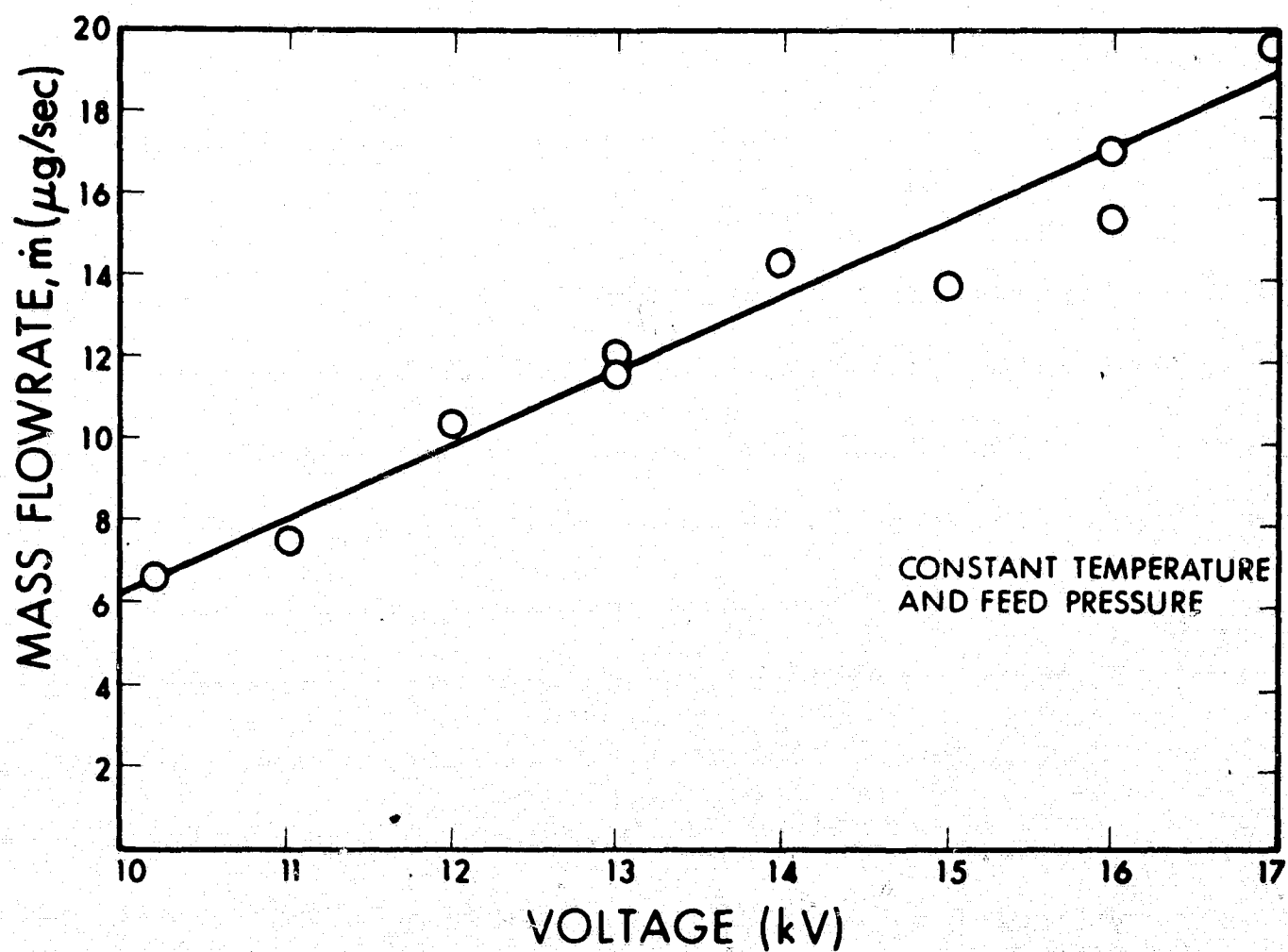


Figure 50. Mass Flowrate as a Function of Voltage
For Annulus A06, Run 7002-02

effect does depend upon the value of \dot{m} and appears to be negligible at high \dot{m} . More data are required to determine a more quantitative dependence for different values of temperature and feed pressure.

As a result of these tests, the variation of \dot{m} with the parameters discussed above can be expressed as

$$\dot{m} = a(V - V_0) (P_f + P_0) \exp(bT_1) \quad (42)$$

where a , b , V_0 and P_0 are constants determined by the geometry of the emitter and the properties of the propellant and V , P_f , and T_1 are independent variables.

5.2.4 TEMPERATURE EFFECTS

Temperature effects upon the charged particle generation process have been difficult to discern for several reasons. Primarily, they have been masked by the large variation of \dot{m} with temperature due to the propellant viscosity and the subsequent variation of specific charge with \dot{m} . Also complicating the situation has been the difficulty of accurate temperature measurements. This effect has been lessened using annuli since the temperature, measured at a point on an emitter body, can be very close to the value at the emitter edge for an annulus or slit while the temperature at the tip of a capillary needle is estimated to differ by 10 or 20°C from the measured value due to a large temperature gradient. Temperature control is also difficult in the presence of backstreaming electrons accompanied by large extractor currents and glow discharges.

Using an electron shield to minimize electron backstreaming, extractor current and glow discharge, tests were performed at 15 kV with annulus A06. The temperature was controlled using an infrared heat lamp, which uniformly heated the entire thruster assembly located in a

cryogenic shroud inside the vacuum chamber. Measurements consisted of maintaining a constant temperature and recording data for a wide range of \dot{m} . The temperature was increased in approximately five-degree increments and data again recorded at various flowrates.

Figure 51 shows a plot of q/m versus \dot{m} for six different temperatures. As expected, the q/m is seen to decrease with increasing \dot{m} at each temperature level. The data are given in Figure 52 which shows a cross plot of the specific charge versus temperature at constant \dot{m} . These data also conform to the typical decrease of $\langle q/m \rangle$ with \dot{m} (shown in Figure 51), but with some scatter in the data. What is most interesting is the decrease in $\langle q/m \rangle$ with increasing temperature at a rate of over 1 percent/ $^{\circ}\text{C}$.

The effect of the decreasing $\langle q/m \rangle$ with increasing temperature at constant \dot{m} is seen in the plot of I versus \dot{m} in Figure 53 and I_{sp} versus \dot{m} in Figure 54. The other curves are uniformly spaced between the -4°C and 20°C curves. Note that at constant \dot{m} , I and I_{sp} decrease with increasing temperature consistent with the decrease in $\langle q/m \rangle$ with temperature. These observations provide the impetus for a renewed consideration of fluid conductivity in the high field spraying environment.

Another factor involved in the electrostatic portion of the electrohydrodynamical process is dielectric constant. The dielectric constant for pure glycerol changes by about 10 percent over the range of temperatures investigated. The dielectric constant of glycerol containing conductive salts as a function of temperature is not known at present, but may be an important factor here.

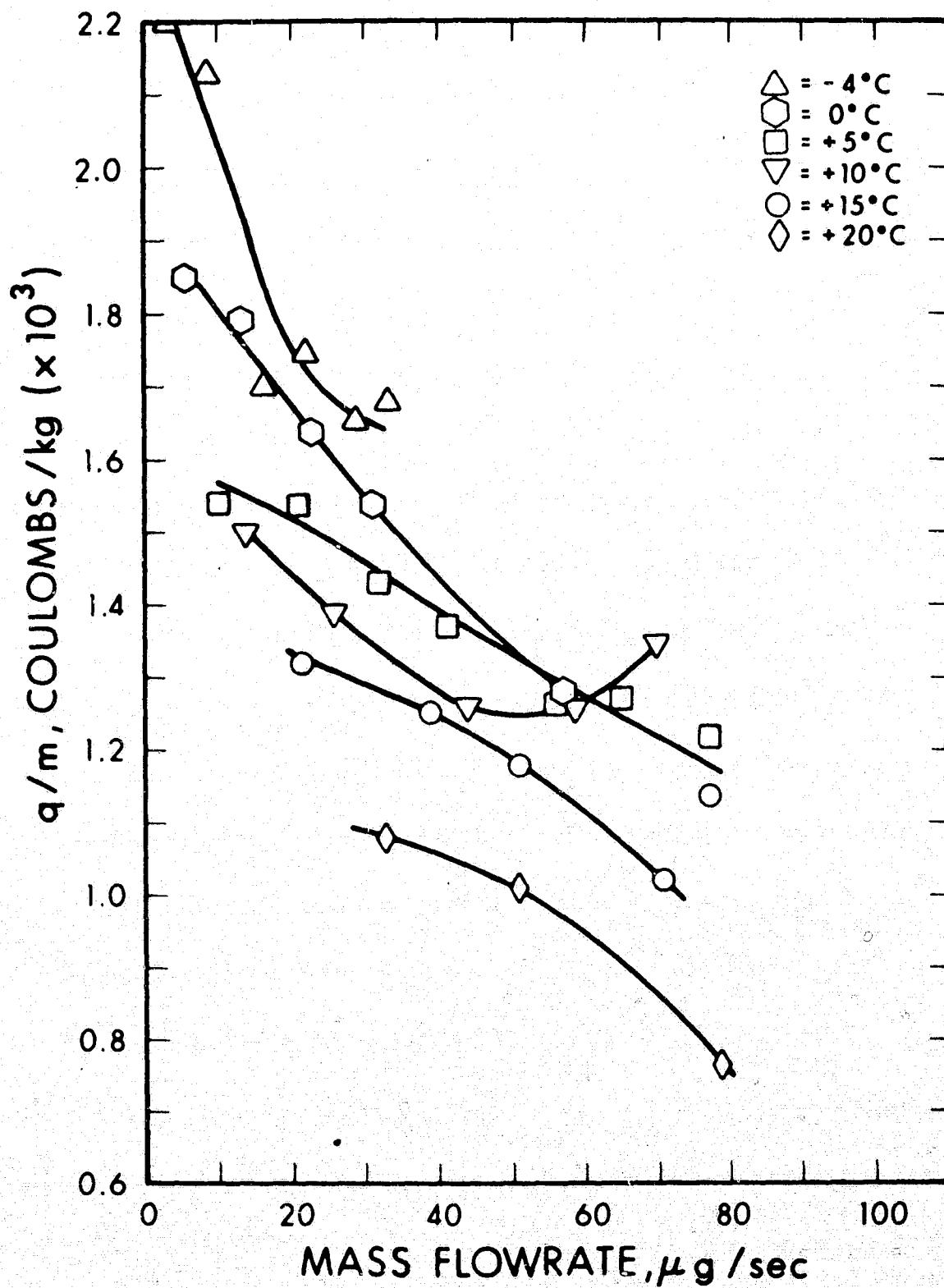


Figure 51. Mass Flowrate as a Function of Specific Charge for Various Temperatures for Annulus A06, Run 7006-02

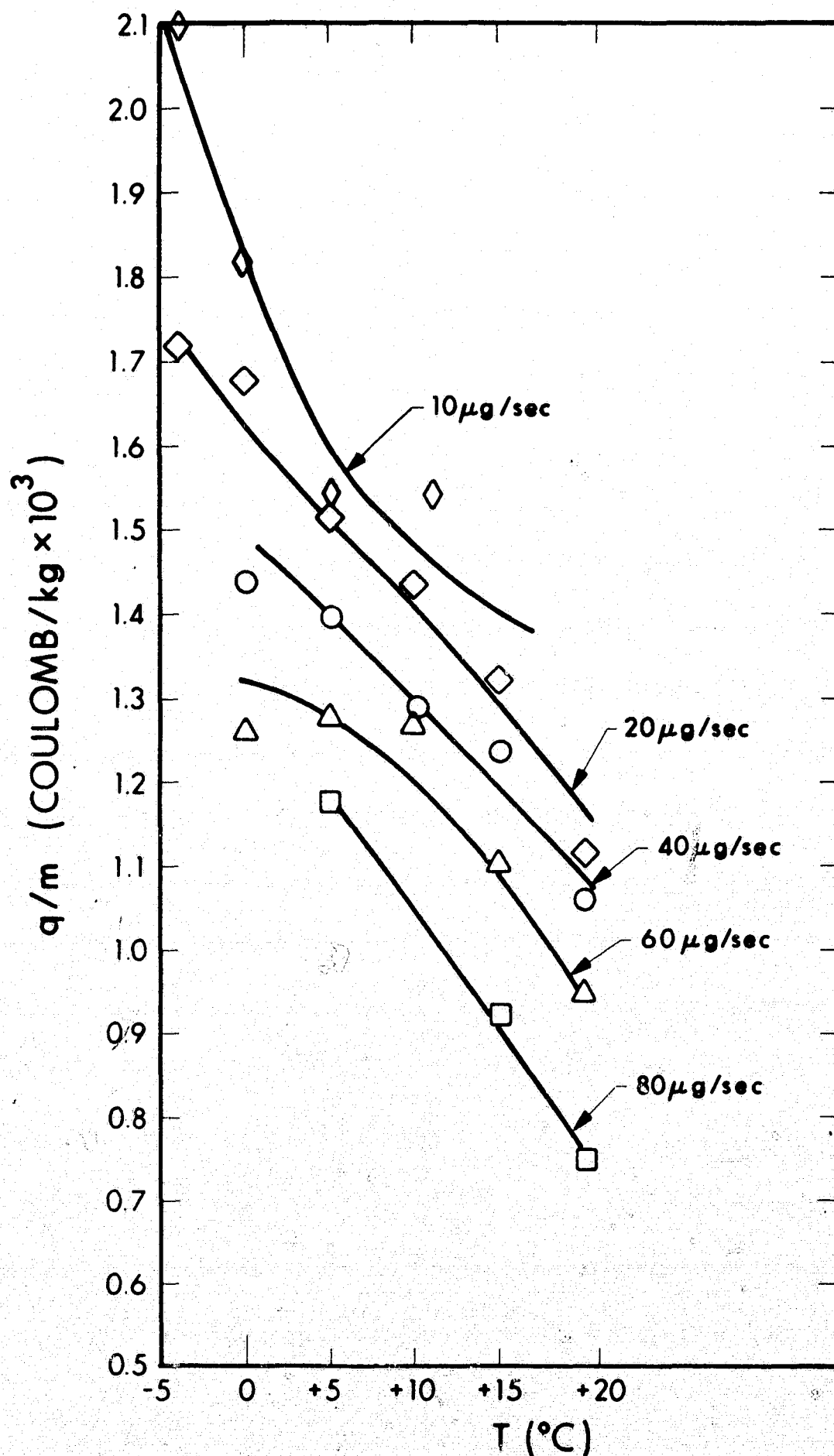


Figure 52. Variation of Specific Charge with Temperature for Constant Mass Flowrates for Annulus A06, Run 7006-02

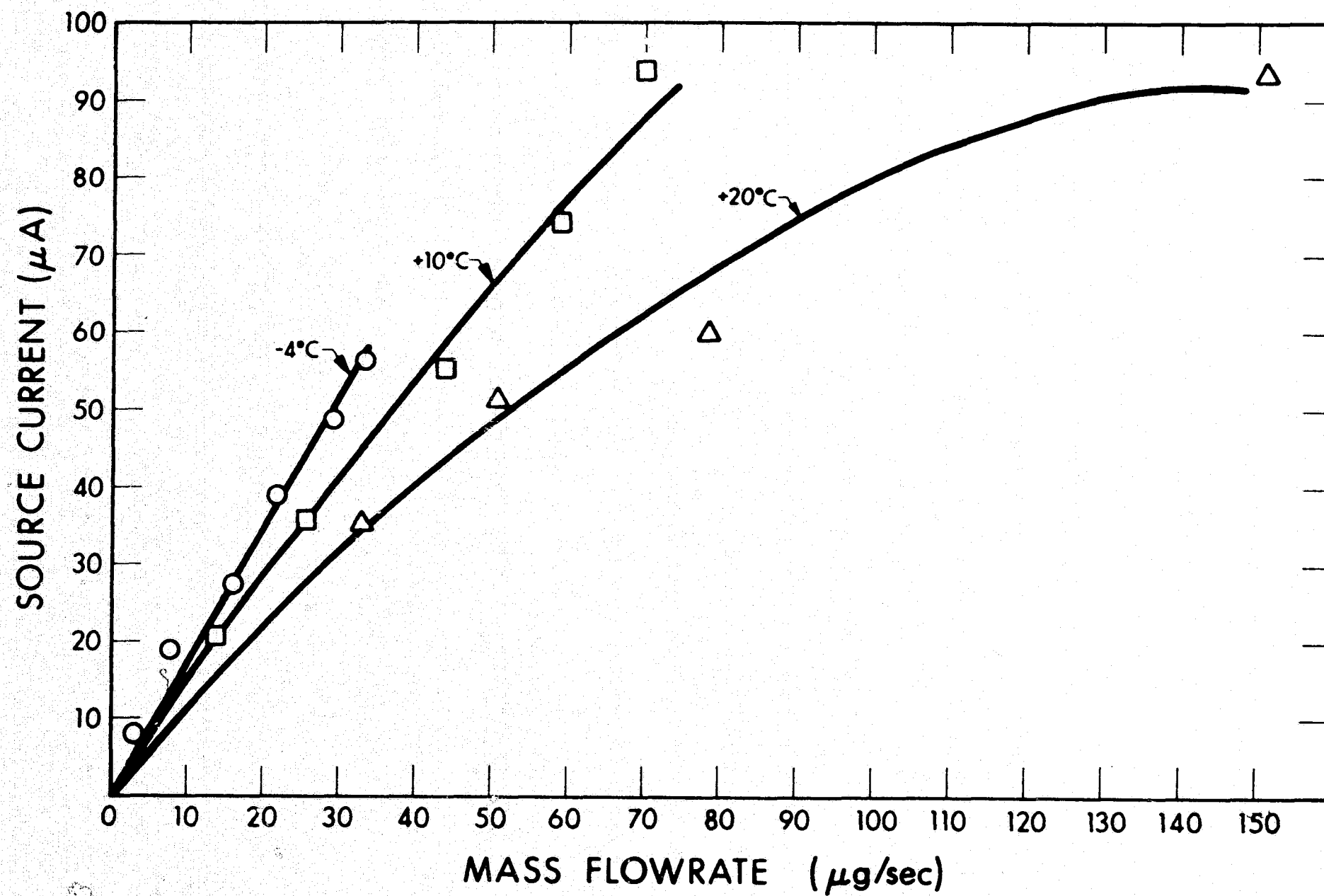


Figure 53. Source Current as a Function of Mass Flowrate
For Annulus A06, Run 7006-02

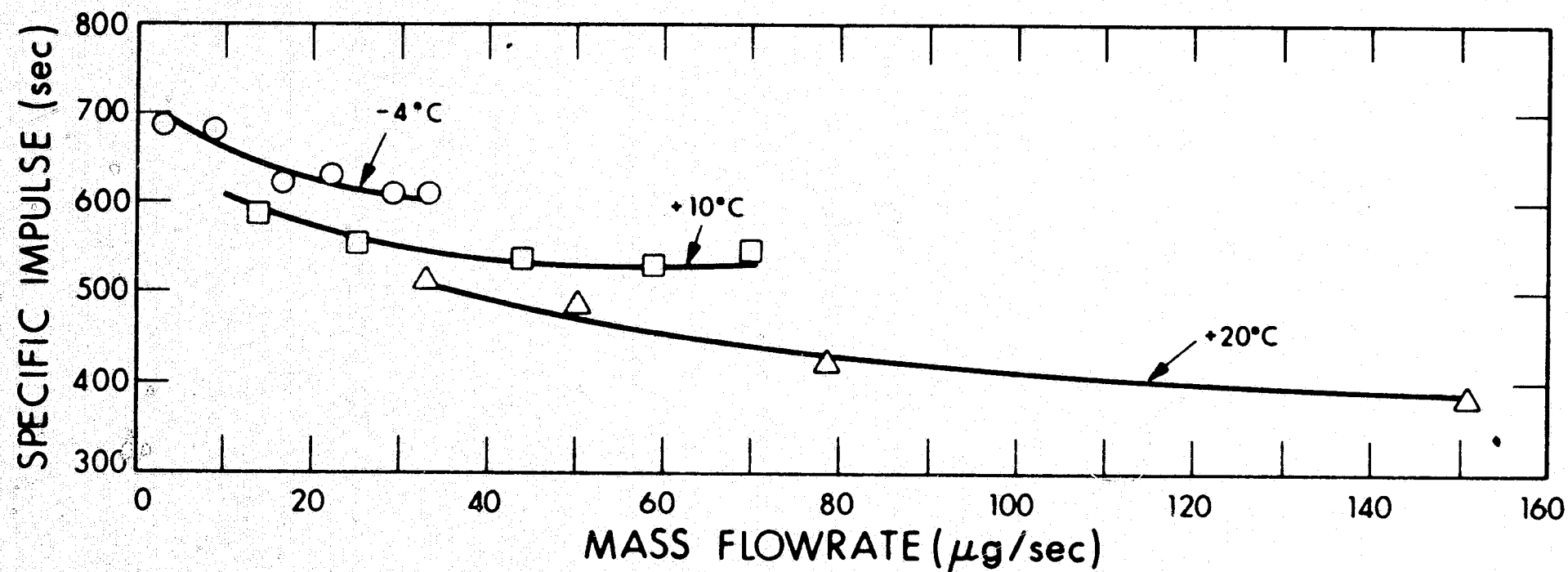


Figure 54. Specific Impulse as a Function of Mass Flowrate for Annulus A06, Run 7006-02

Another propellant property, the viscosity, undergoes a large change in its physical behavior as a function of temperature as seen in Section 3. The viscosity of glycerol decreases by a factor of 10 over the temperature range -4°C to 20°C , the range of operation in this test. In this range, an investigation of the hydrodynamics (viscosity effects) involved in the spraying process may shed some light on the mechanism of particle formation.

5.2.5 SUMMARY OF THRUSTER PERFORMANCE

During the course of this program, several annular emitters were tested and the data analyzed using the equations from the analytical study (Section 4). The experimental data from the different emitters were reduced to plots of the performance parameters versus the mass flowrate and the results of the test characterized by two performance indices, k_o and P . These indices are dependent upon propellant properties and emitter geometry with k_o associated with charge particle generation and P with particle acceleration. Table 6 lists various emitter tests, the propellant mixture batch, and calculated performance indices. In general, higher values of the performance index result in better performance in terms of achieving high thrust and specific impulse. In addition, a given emitter must be efficient and show stable and controlled operation. For example, A01 in Run 6909-02 listed in the table, resulted in very good performance indices, but was unstable and could not be adequately controlled. This was due to lack of temperature control resulting in poor mass flow control.

The GSFC emitter had a very low value of k_o as a consequence of the lack of an inner extractor. A similar low value of k_o was obtained by shorting the inner extractor of A03 to the emitter voltage as discussed in Subsection 5.2.2. This emitter duplicated some of the other performance features of the GSFC emitter including the annulus glow patterns described in Subsection 5.3. Thus, the value of k_o was in part

TABLE 6

PERFORMANCE INDICES OF THRUSTER EMITTERS

Emitter	Test	Propellant	$\left(\frac{k_o}{\frac{\text{A sec}}{\text{kgV}}}\right)^{\frac{1}{2}}$	$10^{-13} \frac{P}{\left(\frac{\text{A kg}}{\text{sec V}^3}\right)^{\frac{1}{2}}}$	Comments
A01	6908-06	F01	0.48	25	12.5, 13.5 kV
	6909-02	F02	0.79	54	Initial observation of linear operation
A02	6910-01	F02	0.384	51	
GSFC	6910-03	F02	0.266	1.8	12, 14, 16 kV
			0.266	~ 40	18 kV data only
A03	6912-01	F03	0.43	~ 57	10, 11, 13 kV
			0.43	~ 16	9 kV only
			0.252	~ 50	Inner extractor shorted to emitter
A06	7002-01	F04	0.45	18	Mass flow and temperature effects
	7002-02	F05	0.47	12	T = 4°C } Temperature effects
			0.33	11	
	7004-03	F05	0.54	12	
	7005-01	F05	0.51	20	Spherical inner extractor (0.25 inch)
	7005-02	F05	0.39	27	Spherical inner extractor (0.31 inch)
A08	7003-01	F04	0.40	6.6	Pt-Ir and SS annulus
A09	7006-01	F05	0.43	200	Extended linear range

dependent upon the potential within the annular circle. A06 showed extremely stable operation with good focusing properties which were attributed to the flattened emitter edge.

The low values of P may have been due to the narrow gap geometry causing irregular emission around the annular parameter. The effect of emitter temperature on k_0 seen in 7002-02 is consistent with the high specific charge at lower temperature considerations discussed in Subsection 5.2.4. Emitter A09 was an improved design with the smaller flat at the emitter edge in an effort to increase the value of k_0 . Tests indicated some improvement with no appreciable loss of focusing properties and stability. The linear region was found to be extended well beyond that of other emitters as reflected in the large value of P .

Using Table 6 an entire run, as characterized by two performance indices, can be compared with the other runs in a quantitative way. This is also a way of comparing propellants from tests with a single emitter. The complete performance characteristics of a thruster can also be obtained using the analytical equation with performance indices obtained from a limited region of operation. Any of the values or a range of control variables determines the operational parameters, with the major uncertainty being the variation of k_0 with emitter temperature.

5.3 GLOW DISCHARGE EFFECTS

Prior to our investigations of glow discharge and extractor currents, it was observed that inner extractor currents were correlated with increasing temperature of an annulus (monitored near the tip region). This had the effect of increasing the mass flowrate, due to propellant properties, occasionally initiating a runaway mode of operation. A possible explanation is that the increase in \dot{m} at high temperature is responsible for an increase in local pressure near the emitter edges, which increased the discharge causing an even greater increase in temperature. This runaway condition is a self-feeding mechanism where electrons in the discharge heat the annulus. Conditions are then established for perpetuating the discharge. At all times the presence of a glow is accompanied by poor performance, uncertainty in the data, and a condition that undoubtedly causes deterioration of the emitter.

A series of tests were performed to study glow discharge phenomenon and the behavior and origin of annulus inner extractor currents. The vacuum chamber pressure for the tests described in this section (and in general) remained in the 10^{-6} torr range or below. Although the pressure does affect the glow discharge, the local pressure (due to outgassing, evaporation, etc.) appears to be more dominant. The glow discharge was also investigated by examining its radiation characteristics using a photomultiplier tube and combination of filters. The investigation of the behavior of inner extractor currents revealed the significance of glow discharge and its relation to thruster performance. These latter tests showed how inner extractor currents and glow discharge are a related and interdependent phenomenon.

Glow discharge had been observed in our laboratory tests and also at GSFC. To simulate the geometrical conditions of the GSFC emitter, an

annulus was operated with the inner extractor connected to the emitter potential. The change in the pattern of glow discharge was immediately apparent. Instead of being concentrated in the region between the inner extractor and annulus, it now covered the entire inner extractor and resembled the GSFC emitter glow. This indicates that the presence of a negative inner extractor reduces the scope and intensity of the discharge, but is not sufficient to eliminate the discharge entirely.

5.3.1 RADIATION CHARACTERISTICS OF GLOW DISCHARGE

The light output in the glow discharge region of annulus A03 (Run 7002-03) was examined using a photomultiplier tube (S-11 response) and a combination of sharp cutoff glass filters to cover the region from 400 to 650 mμ. The relative intensity of the radiation in several wavelength regions isolated by a combination of filters was measured. Briefly, the relative intensity was obtained using the expression $\Delta i_p / \bar{\eta} \Delta \lambda$ where Δi_p is the photomultiplier current due to light emission in the cutoff band, $\bar{\eta}$ is a normalized spectral response of the photomultiplier tube, and $\Delta \lambda$ is the wavelength band determined by the difference between midpoint values of adjacent transmission curves.

A histogram plot of the results in Figure 55 shows the relative intensity versus wavelength. As expected, a peak was observed which corresponds to resonance radiation from atomic sodium (5890Å). Atomic sodium even in minute quantities can be a major constituent that supports the discharge.

5.3.2 GLOW DISCHARGE AND INNER EXTRACTOR CURRENTS

As a result of the test to study inner extractor currents, it was determined that these currents were directly related to the glow discharge.

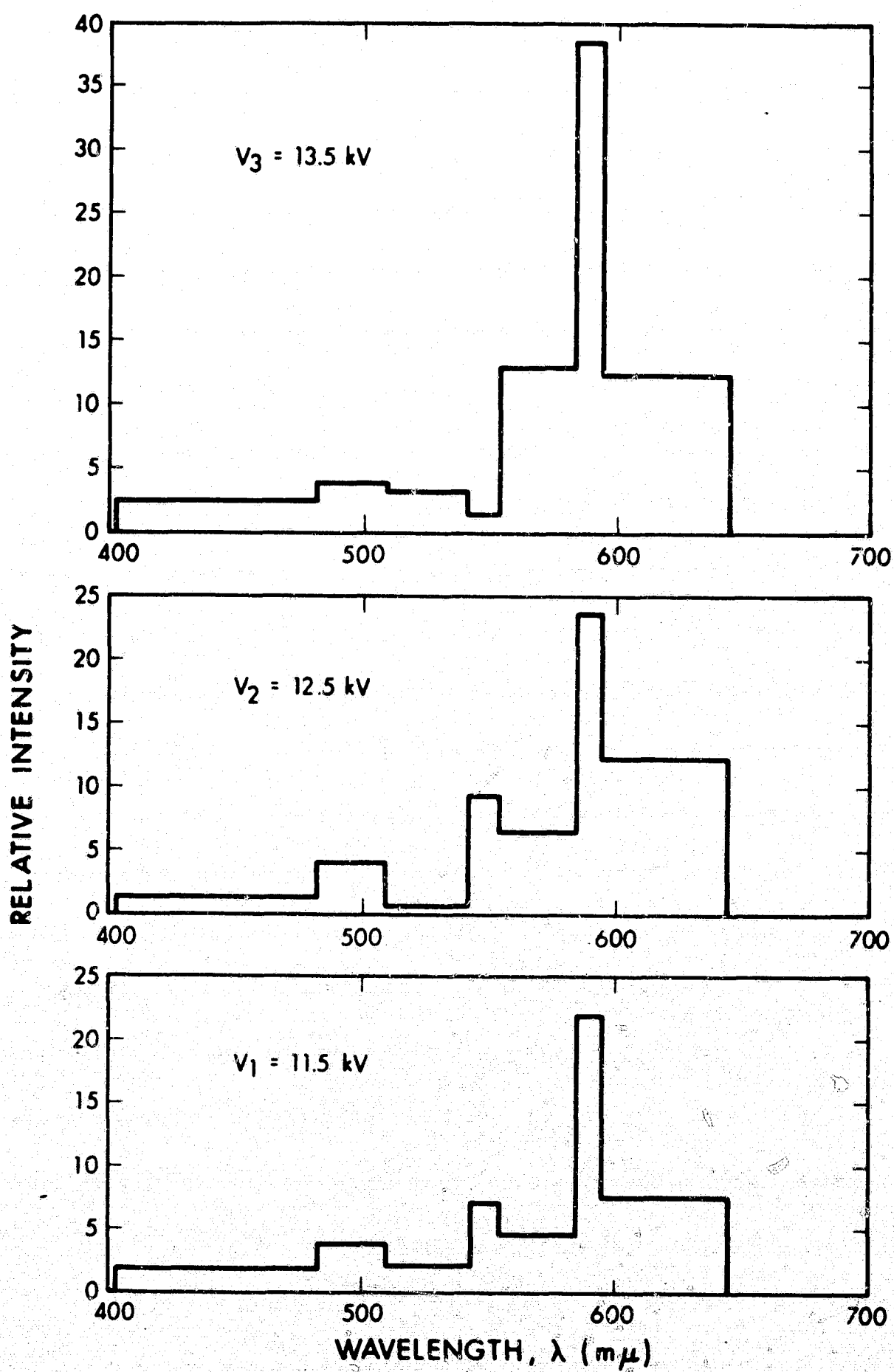


Figure 55. Wide Band Spectra of Annulus Glow
(Annulus A03, Run 7002-03)

Also, the glow discharge was observed to be related to the presence of backstreaming electrons which originate at collector and/or grid surfaces.

The tests involved maintaining the inner extractor voltage constant while the outer extractor voltage was varied. The data from these tests are plotted in Figure 56, with a glow discharge limiting line included to indicate the point at which the inner extractor current begins to rise, and was observed to coincide with the onset of glow discharge. Information contained in the plots worth emphasizing are the increase in the initial slope of the inner extractor current with decreasing negative potential, and the saturation value of the inner extractor current that decreases with increasing negative voltage.

The value of the slope of the inner extractor current is directly related to the illuminative intensity in the glow discharge. Further, the intensity of the discharge is believed to be strongly dependent on the presence of electrons in the discharge region, becoming more intense as the electron current density increases. It should be pointed out that the inner extractor current slope is greater when the voltage is smallest.

It was observed that the glow discharge could be controlled, i.e., made to appear or disappear, as the outer extractor voltage was made more or less negative. At 13 kV annulus potential, the discharge appeared at -300V on the outer extractor and was extinguished at -400V. With -400V on the outer extractor, the annulus potential was then increased in steps of 1 kilovolt until the discharge reappeared. The data are given in Table 7.

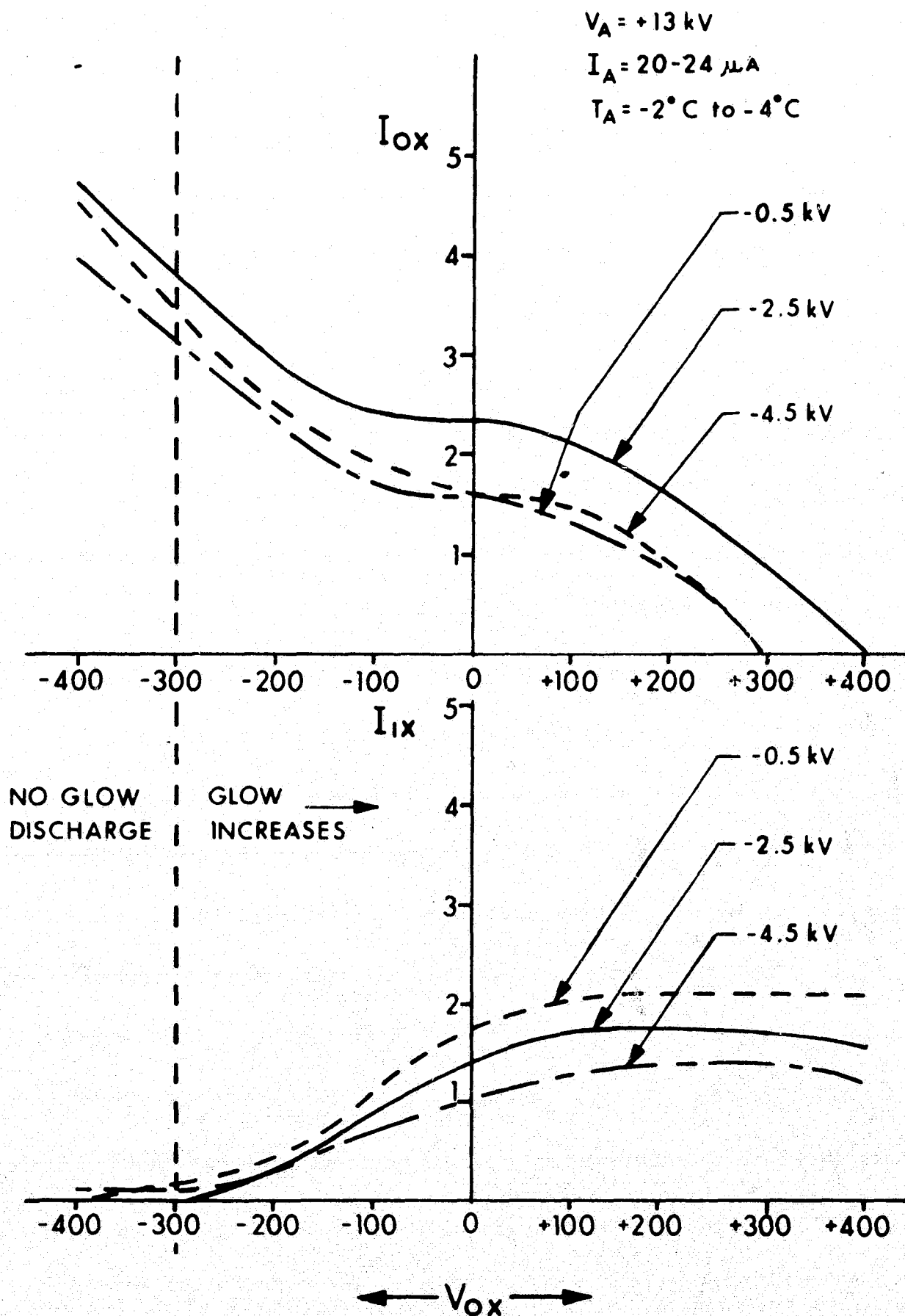


Figure 56. Variation of Inner and Outer Extractor Currents with Outer Extractor Voltage at Inner Extractor Voltages of -0.5, -2.5, and -4.5 kV. (Annulus A06, Run 7004-03)

TABLE 7

OBSERVATION OF GLOW DISCHARGE WITH INCREASING ANNULUS POTENTIAL

V (kV)	I (μ A)	I _{ix} (μ A)	I _{ox} (μ A)	T _A (C ^o)	Glow Condition
14	43	0	12	+2	No glow
15	54	0.2	17	+3.5	No glow
16	110	6.0	35	+12	Glow appeared
V _{ix} = -4.5 Kv, V _{ox} = -400V					

At 16 kV, the glow appeared and the temperature of the annulus increased rapidly. The annulus potential was maintained at 16 kV and the outer extractor voltage was increased to -500V. The glow was observed to disappear at this setting and the annulus current dropped from 110 μ A to 90 μ A while the outer extractor current was dropping from 35 μ A to 14 μ A. This is a decrease of about 20 μ A on both the annulus and outer extractor when there is no glow. This could indicate that in the previous condition (at the same annulus potential), with glow present, 20 μ A of electron current was leaving the outer extractor arriving at the annulus. However, it is suspected that electrons alone would not account for 20 μ A at the outer extractor. Rather, the initial secondary electrons ejected are multiplied through collisions with the gas occupying the space between the outer extractor and annulus. Thus, positive ions formed in collisions could contribute to the outer extractor current in addition to secondary electrons. When the annulus potential was increased to 17 kV with -500V on the outer extractor the glow reappeared.

A summary of the important features which have evolved from the tests just described are:

- a. The glow discharge was determined to be related to back-streaming secondary electrons from the vacuum chamber environment.

- b. The temperature of the annulus, discharge glow, and inner extractor currents are interrelated and interdependent.
- c. There is compelling evidence that inner extractor currents are not due, at least initially, to spraying from the annulus.
- d. Glow discharge can be minimized by operating with more negative outer extractor voltages.

5.3.3 TRAPPING ELECTRODE TESTS

Tests results of the inner extractor currents discussed above furnished convincing evidence that the glow discharge was related to backstreaming electrons. It was seen that the outer extractor bias was an important feature of the glow discharge. However, control was limited under this experimental condition. As the annulus voltage was increased, the outer extractor required additional negative bias to extinguish the glow. It was then felt that the addition of a negative electrode placed forward of the outer extractor would sufficiently trap electrons repressing the initiation mechanism of the glow discharge. In addition, this would remove the constraint of glow condition so the outer extractor could be made controllable over a wide range of voltages without encountering a glow discharge condition.

Based on these predictions, an electron trapping electrode was constructed and installed in the annulus assembly used in run 7004-03. The thruster configuration shown in Figure 57 was left completely undisturbed, except for cleaning operations, so data with the electron shield could be correlated with the data from the inner extractor current tests.

Remarkably improved operation with the electron shield was apparent when no discharge glow was observed under conditions where glow was previously obtained. No inner extractor currents were observed and the stability of operation illustrated by the data in Table 8. Note that over the range

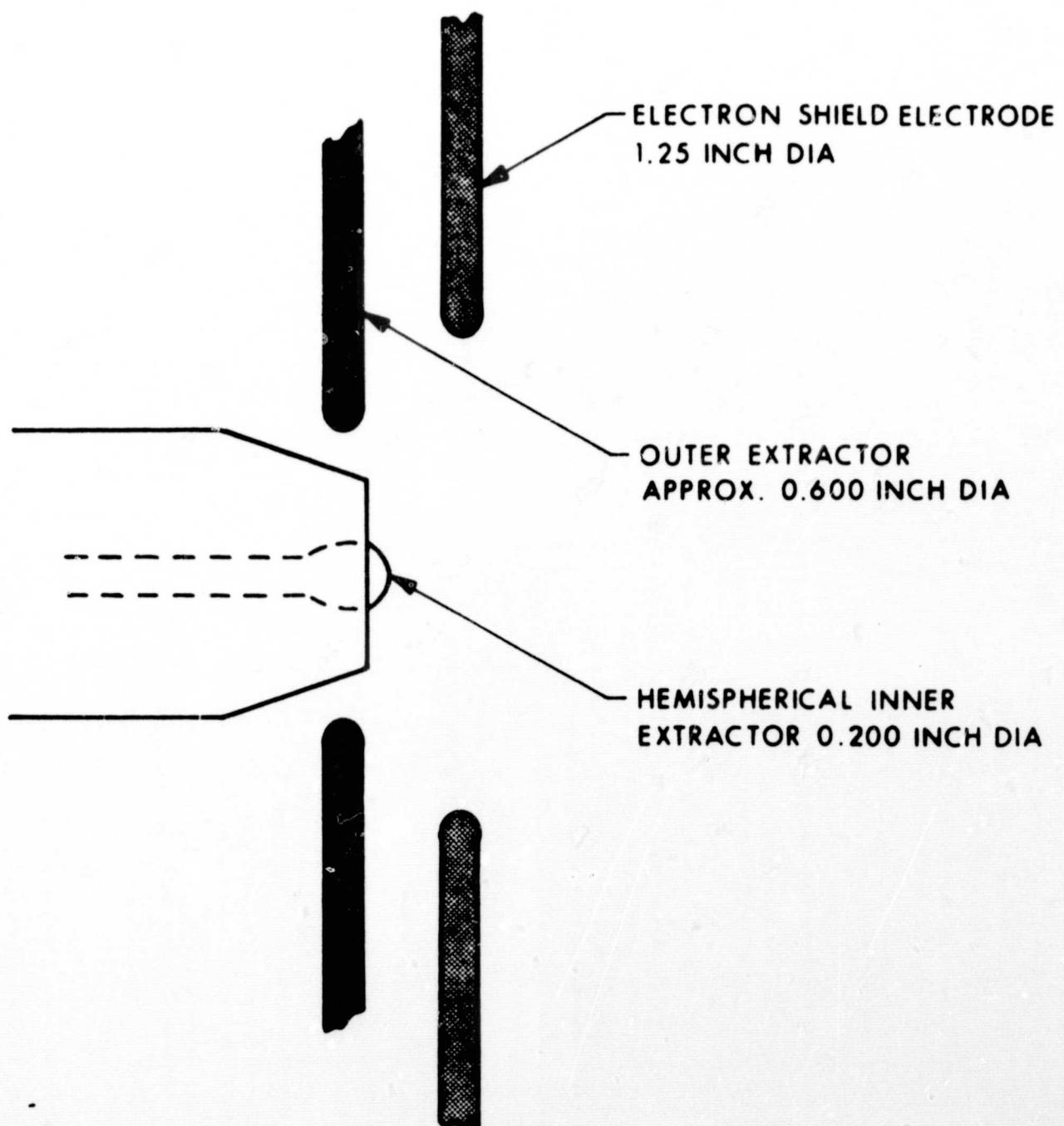


Figure 57. Cross Sectional View of Annulus (A06) Assembly
Showing Electron Shield Electrode

TABLE 8

ANNULUS DATA WITH ELECTRON TRAP ELECTRODE MOUNTED (NO DISCHARGE GLOW)

V_A (kV)	I_A (μ A)	I_{IX} (μ A)	I_{OX} (μ A)	I_S (μ A)	T_A ($^{\circ}$ C)	P_F (in. Hg)
17	15	0	0	1.7	-6	14
17	29	0	0	2.6	-6	12
17	40	0	0	3.1	-6	10
17	49	0	Neg.	3.4	-6	8
17	68	0	Neg.	3.8	-6	6
17	66	0	Neg.	4.1	-6	4
17	74	0	Neg.	4.6	-6	2
17	86	0.2	Neg.	6.0	-5	0
15	12	0	0	1.2	-6	14
15	25	0	0	1.8	-6	12
15	34	0	0	2.2	-6	10
15	42	0	0	2.6	-6	8
15	50	0	0	2.5	-6	6
15	58	0	0	2.9	-6	4
15	65	0	Neg.	3.6	-5.5	2
15	73	0	Neg.	3.6	-5	0
13	8	0	0	0.8	-5	14
13	21	0	0	1.4	-5	12
13	30	0	0	1.5	-5	10
13	37	0	0.4	1.5	-5.5	8
13	44	0	0	1.5	-5	6
13	49	0	0	1.5	-5	4
13	56	0	0	1.5	-5	2
13	61	0	0	1.5	-5.5	0
$V_{IX} = -4.5$ kV, $V_{OX} = 400$ V, $V_s = -500$ V						

from 13 to 17 kV, no inner extractor currents were discernible. In addition, the temperature remained constant as the annulus current varied between 8 and 86 μ A. It is of interest to mention that at one point the 17 kV on the annulus, the outer extractor voltage was decreased to zero and no glow was observed. In the previous run (No. 7004-03) at 17 kV glow was observed even with -500V on the outer extractor. This observation is further proof of the effectiveness of the electron trapping electrode.

5.4 ADVANCED STATE-OF-THE-ART THRUSTER

Based on the experimental and analytical investigations described in this report, it is possible to theoretically design a thruster system to predetermined specifications. There are still several features of such a thruster system that are not within the state of the art, but these are just beyond it and are considered reasonable extrapolations. Techniques for increasing the performance index, k_o , are under examination and the quantitative effects of temperature have not been determined. Further work on the former will be continued, and the latter should be understood by means of some well defined experiments.

A comparison of annular emitter state of the art performance with the continuation program (Phase II) goals is summarized in Table 9. The requirements of thrust density and source efficiency in the region of 15 kilovolts can be met and surpassed using existing emitter/fluid technology. The need to achieve higher specific impulses is apparent from an examination of the data in the table.

The thrust density requirement of 25 to 35 μ lb/source defines a thruster module consisting of 8 to 10 annular emitters, ultimately capable of producing a total thrust of 250 μ lbs. The number of emitters required to produce a 1/4 mlb thruster can be reduced by operating at a higher thrust

TABLE 9

COMPARISON OF STATE-OF-THE-ART PERFORMANCE WITH PROGRAM GOALS

	Thrust Density (μ lb/Source)	Specific Impulse (sec)	Source Voltage (kV)	Source Efficiency (%)	No. Emitters per 1/4 mlb Thrusters
Phase II Goals	25-35	> 1500	< 15	> 70	8-10
Run 7002-02	25-35	860-825	14	> 80	8-10
	60	700	14	> 80	5
	86	600	14	> 80	3
Run 7004-04	25-35	749	17	72.7	8-10
	66	749	17	72.7	4
	25-35	695	15	75.5	8-10
	54	695	15	75.5	5
	25-35	639	13	77.9	8-10
	45	639	13	77.9	6
Run 7005-02	25-35	800-750	16	79.7	8-10
	100	620	16	79.7	3
	25-35	710-670	14	82.8	8-10
	95	540	14	82.8	3

density ($\mu\text{lb}/\text{source}$). This is achievable, however, at the expense of operating at lower specific impulse levels for these emitters as shown in Table 9. A tradeoff exists, therefore, between number of emitters (reliability factor) and specific impulse (performance).

An advanced state-of-the-art thruster is described which would meet the Phase II program design goals given in Table 9. The characteristics of a single emitter are discussed along with the tradeoffs that occur over a wide range of operation. A thruster array design is described, using this basic type emitter, which could attain a 1 mlb thrust level with only 19 emitters.

To achieve a low beam divergence, the range of operation should be limited to the linear region where $x \leq 0.2$. Thus the value of x (Eq. 14) is chosen to be 0.1 to achieve the maximum thrust well in the linear region. From the experience gained on this program, this type of performance requires a low thrust per emitter with the emitters having the general dimensions described in Section 2. It is also desirable to minimize the number of emitters because system reliability tends to decrease as the number of critical parts increases. As a compromise, a 19 annuli hexagonal array is chosen for the number of emitters and the array geometry with each emitter required to produce 53 μlb . The specific impulse is chosen at 1500 sec and $\eta = 80$ percent. The operating voltage is chosen at 15 kV which may be too low to generate the required mean specific charge.

Performance indices found to satisfy these conditions are

$$k_o = 0.815 \text{ (A sec/kgV)}^{1/2}$$

$$P = 87.2 \times 10^{-13} \text{ (Akg/sec V}^3)^{1/2}$$

This value of k_o is only slightly above the highest value achieved on the program (see Table 6), while P is well within the present state of the art. With these specifications, the operational parameters are calculated and shown in Figure 58 as a function of the mass flowrate. Note the similarity between this figure and Figure 36 which is for an emitter having a higher k_o , but lower P . Both sets of performance indices will satisfy the goals given in Eq. 47, but a more extended linear region is shown in Figure 58. Table 10 shows the tradeoff in I_{sp} for increasing thrust for such a single emitter. The beam input power (IV) is also listed for one emitter and the thrust is given for 6 and 19 emitters. The linear region extends up to about 100 μlb but performance can theoretically be extended to 300 μlb and higher.

TABLE 10

ADVANCED ANNULUS THRUSTER

1 Emitter			6 Emitters	19 Emitters
T (μlb)	I_{sp} (sec)	Power (watts)	T (μlb)	T (μlb)
10	1560	0.45	60	190
53	1500	2.0	318	1000
100	1415	3.9	600	1900
170	1305	6.0	1020	
$k_o = 0.815, P = 87.2 \times 10^{-13}$ $V = 15 \text{ kV}$				

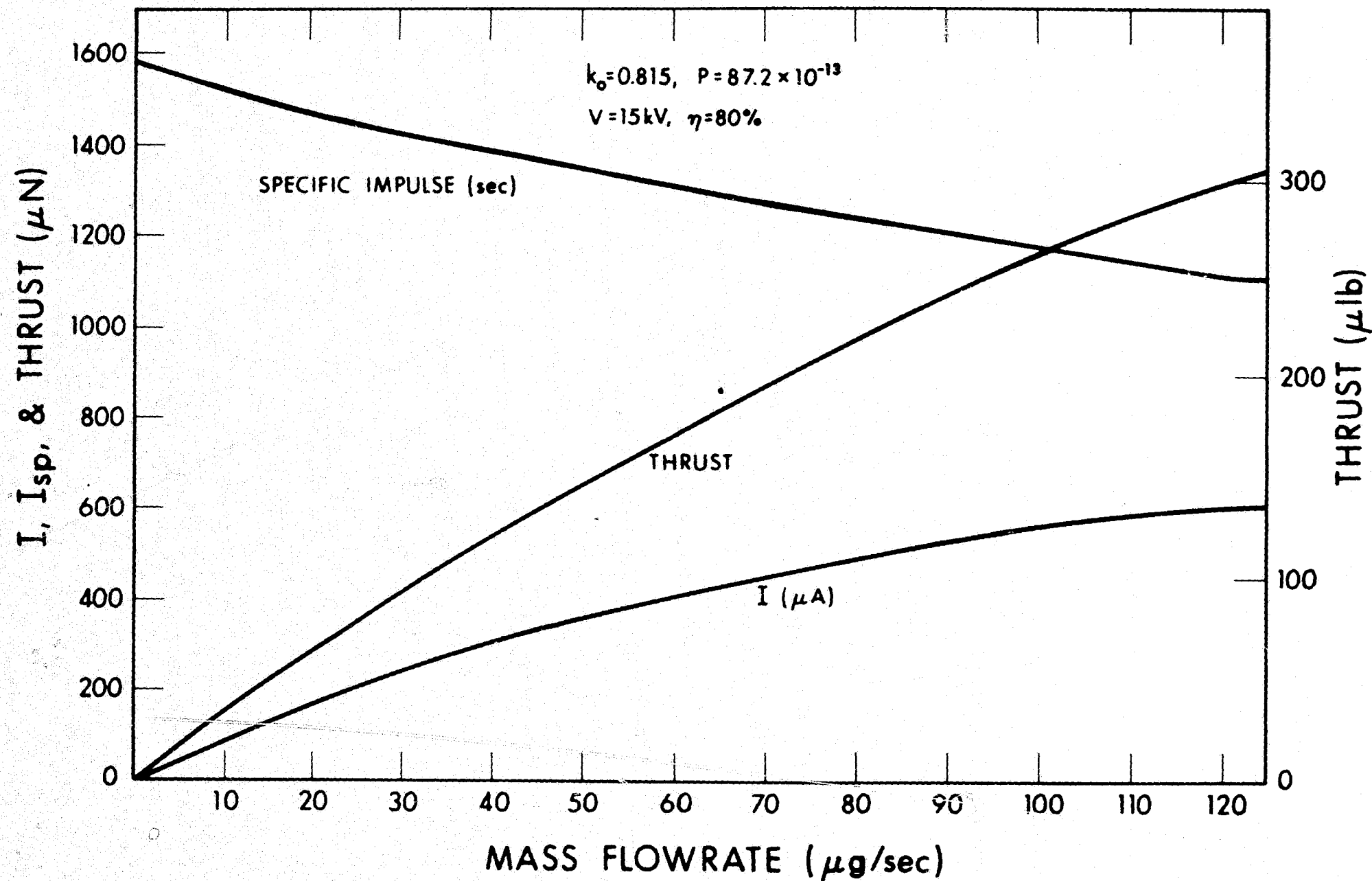


Figure 58. Operational Parameters versus \dot{m} for an Advanced Thruster Design for $k_o = 0.815$, $P = 87.2 \times 10^{-13}$, $\eta = 80\%$ Operated at 15 kV

SECTION 6

SUMMARY

A general review summarizing significant highlights and contributions made to colloid technology during this program is given in this section. Achievements relating to experimental performance will be examined first, followed by a discussion of complementary experimental/analytical investigations. Those areas where problems were encountered will be discussed in relationship to the continuation program.

6.1 ACHIEVEMENTS

Prior to the initiation of this program, the concept of recording and analyzing TOF data was considered, which would be capable of handling large amount of experimental data. Automatic data gathering techniques were desirable for eliminating systematic human error and for providing thruster performance feedback during, and not after, a test run. These considerations led to the development and successful operation of the data acquisition system discussed in Section 2.

Interest in colloid propulsion at Electro-Optical Systems led to the development of a thermo-differential mass flowmeter and flow controller system (with breadboard electronics) on an internally funded development program. The system was successfully integrated and operated with an annulus thruster. An advantage of this device in a thruster system is apparent from the potential feedback and variable flowrate capabilities.

Investigations into the origin of inner extractor currents led to uncovering of the mechanism responsible for sustaining glow discharge. Subsequent investigation produced data relating the dependence of inner extractor currents on glow discharge. An electron trap shield proved to be effective in eliminating both and together with the Pt/Ir annulus should greatly reduce erosion during long term tests.

The effectiveness of the inner extractor in the annulus assembly was demonstrated quite drastically in experiments comparing operation with and without the extractor electrode. Operation with the inner extractor has the advantage of producing better beam focusing, increasing k_0 , and reducing glow discharge.

Considerable emphasis was placed on isolating the effect of temperature on emitter performance during this program. As a result of these studies, a better understanding of the importance of emitter temperature control has emerged. Under the condition of constant mass flowrate, it was found that the specific charge decreased with increasing temperature. Related to this observance is the fact that the performance index, k_0 , decreases with increasing temperature. Unless a constant temperature is maintained at a suitable operating level, instability may result manifested by varying flowrates and unwanted beam divergence. In addition, the importance of comparing data at constant temperatures is necessary to minimize errors due to scatter in the data.

The near-linear region of operation was demonstrated experimentally and described analytically. Operating in this region will greatly simplify a thruster control system since the emitter current can be used in a feedback loop for mass flowrate and/or emitter voltage control.

The analytical work discussed in Section 4 that predicts thruster operation was beneficial for several reasons. First, it provided a confident method for extrapolating data. Secondly, theoretical expressions developed yielded a set of performance indices by which the performance of emitters can be classified using two indices, k_o and P . These parameters, as we have seen, provide a reasonable basis for design of future annulus emitters. Thirdly, the analytical study was fruitful in establishing guidelines for future experimental studies. A useful feature of the analytical work is that one can predict the thrust and specific impulse from V and \dot{m} over a wide range of operation.

Two features not included in the past analytical study are the temperature effect upon k_o , discussed above, and the operational level effect upon beam configuration. Beam focusing was examined in Subsection 5.2.2 and was shown to depend upon the control variable in a reproducible manner. It is expected that both beam configuration and the temperature effects will be integrated into the analytical expressions.

6.2 PROBLEMS

Further development of a colloid thruster system capable of producing a 1/4 mlb thrust level will require a number of identical annuli emitters to ensure good efficiency. Therefore, emitter fabrication techniques have to be controlled to ensure reproducibility of tip configurations and also propellant flow impedances. The problem arises in achieving the above-mentioned specifications in view of the large annular dimensions and the small gap dimensions involved.

The performance goals for the Phase II program are all within the state of the art except for the specific impulse of greater than 1500 seconds. Although experimental channels directed toward increased specific impulse are known, it is anticipated that a concentrated effort will be necessary to achieve 1500 seconds.

GLOSSARY

<u>Symbols</u>	<u>Definition</u>
V	Emitter Voltage
V_o	Onset Voltage for Spraying
V_{ix}	Inner Extractor Voltage
V_{ox}	Outer Extractor Voltage
V_s	Electron Trap Electrode Voltage
I	Emitter Current
I_{ix}	Inner Extractor Current
I_{ox}	Outer Extractor Current
I_s	Electron Trap Electrode Current
i_o	TOF Collector Current at $t = 0$
i	TOF Collector Current
t_f	TOF Time at $i = 0$
L	Distance Between Emitter and TOF Collector
A	Area Under TOF Trace
t_c	Time Coordinate of TOF centroid
T_A	Emitter Temperature
\dot{m}	Mass Flowrate
I_{sp}	Specific Impulse
T	Thrust
q/m	Specific Charge
$\langle q/m \rangle$	I/\dot{m} , Mean Specific Charge
$\langle q/m^{1/2} \rangle^2$	Square Mean Root Specific Charge
η	$\langle (q/m)^{1/2} \rangle^2 / \langle q/m \rangle$, Specific Charge Efficiency
ϵ	i_o/I ; Collection Efficiency
g	Acceleration due to Gravity

GLOSSARY (contd)

<u>Symbols</u>	<u>Definition</u>
P_F	Feed System Pressure
P_O	Pressure due to Capillary Forces
TOF	Time-of-Flight
DAS	Data Aquisition System
IX	Inner Extractor
OX	Outer Extractor
LN_2	Liquid Nitrogen

Conversion Factors

Thrust	$1 \mu\text{lb} = 4.5 \mu\text{N (newtons)}$
Mass Flowrate	$1 \times 10^{-9} \text{ lb/sec} = 0.454 \mu\text{g/sec}$

REFERENCES

1. J. Perel, R. D. Moore, A. Y. Yahiku, and J. Mahoney, "Electrodeless Particle Thruster," Tech. Report AFAPL-TR-67-106, Res. and Tech. Div., AFSC Wright-Patterson AFB, Ohio (Oct 1967)
2. M. N. Huberman, Ernest Cohen, "Research on Charged Particle Electrostatic Thrusters," AFAPL-TR-67-115, Air Force Aero Propulsion Laboratory, Wright-Patterson AFB, Ohio (Sep 1967)
3. M. N. Huberman, P. W. Kidd, "Charged Particle Electrostatic Thrusters," AFAPL-TR-69-14, Air Force Aero Propulsion Laboratory, Wright-Patterson AFB, Ohio (Mar 1969)
4. K. W. Stark, "Design and Development of an Annular Slit Colloid Thruster," Paper No. 69-287, AIAA 7th Electric Propulsion Conf., Williamsburg, Virginia (Mar 1969)
5. J. Perel, J. F. Mahoney, R. D. Moore, and A. Y. Yahiku, "Research and Development of a Charged Particle Bipolar Thruster," AIAA J., 7, p. 507 (1969)
6. R. E. Hunter, "Theoretical Consideration of Nonuniformly Charged Expellent Beams," ARL Technical Note 60-138 (Oct 1960)
7. F. B. Hildebrand, Introduction to Numerical Analysis, McGraw-Hill, New York (1956), p. 71-76
8. American Institute of Physics Handbook (McGraw-Hill Book Company, Inc., New York, 1963)
9. C. D. Hendricks, "Research on High Intensity Charged Particle Sources," AFAPL-TR-67-92, Air Force Aero Propulsion Laboratory, Wright-Patterson AFB, Ohio (Aug 1967)
10. R. J. Pfeifer and C. D. Hendricks, "Charge to Mass Relationships for Electrohydrodynamically Sprayed Liquid Droplets," Phys. Fluids, 10, p. 2140 (1967)
11. A. Sherman, "Parametric Analysis of Electrostatic Dispersion of a Liquid," NASA X-734-67-321, Goddard Space Flight Center, Greenbelt, Maryland (Jul 1967)
12. P. W. Kidd, "Parametric Studies with a Single-Needle Colloid Thruster," J. Spacecraft, 5, p. 1034 (1968); Paper No. 67-530, AIAA Electric Propulsion and Plasmadynamic Conf., Colorado Springs, Colorado (Sep 1967)
13. J. Perel, J. F. Mahoney, R. D. Moore, and A. Y. Yahiku, "Research and Development of a Charged Particle Bipolar Thruster," AIAA J., 7, p. 507 (1969)
14. J. Perel, A. Y. Yahiku, and J. F. Mahoney, "Focusing and Deflection of Heavy Charged Particle Beams," Paper No. 69-283, AIAA 7th Electric Propulsion Conf., Williamsburg, Virginia (Mar 1969)